Application of carboranes and metallacarboranes for synthesis of innovative nanostructures and for the development of highly stable ion-pair potentiometric sensors

Abhishek Saini

Universitat Autònoma de Barcelona

Application of carboranes and metallacarboranes for synthesis of innovative nanostructures and for the development of highly stable ion-pair potentiometric sensors.

Abhishek Saini

Doctoral Thesis
(Programa de Doctorat en Quimica)

Supervisor: Prof. Francesc Teixidor i Bombardo
Tutor: Prof. Josep Ros Badosa

Departament de Quimica
Facultat de Ciences

2019

ICMAB INSTITUT DE CIÈNCIA DE MATERIALS DE BARCELONA
EXCELENCIA SEVERO OCHOA
CSIC CONSEJO SUPERIOR DE INVESTIGACIONES CIENTÍFICAS

Memòria presentada per aspirar al Grau de Doctor per

Abhishek Saini

Vist i plau

Prof. Francesc Teixidor i Bombardo (Supervisor)

Prof. Josep Ros Badosa (Tutor)

Bellaterra, 19th July, 2019

MINISTERIO
DE CIENCIA, INNOVACIÓN
Y UNIVERSIDADES

ICMAB
INSTITUT DE CIÈNCIA DE MATERIALS DE BARCELONA

CSIC

Le Professor Francesc Teixidor i Bombardo, Profesores d'Investigació del *Consejo Superior de Investigaciones Científicas* a l'*Institut* de *Ciència de Materials de Barcelona*

CERTIFICA

Que n' ABHISHEK SAINI, llicenciada en Química, ha realizat sota la seva dirección el treball que porta per titol "*Application of carboranes and metallacarboranes for synthesis of innovative nanostructures and for the development of highly stable ion-pair potentiometric sensors.*"
que queda recollit en aquesta memoria per optar al titol de Doctor per la
Universitat Autònoma de Barcelona.

I, perquè aixi consti i tingui els efectes corresponents, signa aquest certificat a Bellaterra, a 19 de Julio del 2019.

Prof. Francesc Teixidor
ICMAB-CSIC

http://icmab.es

Campus de la Universitat Autònoma de Barcelona
08193 Bellaterra, Catalunya, Espanya
Telf.: +34 935 801 853
Fax.: +34 935 805 729

http://icmab.es

Campus de la Universitat Autònoma de Barcelona
08193 Bellaterra, Catalunya, Espanya
Telf.: +34 935 801 853
Fax.: +34 935 805 729

Aquest treball de recerca ha estat finançat per la Comisión Interministerial de Ciencia y Tecnología, CICYT, mitjançant els projectes CTQ2013-44670-R i CTQ2016-75150-R; per la Generalitat de Catalunya amb el projecte 2014/SGR/149 i els projectes concedit per Unió Europea H2020-NMBP-13-2017 y KARDIATOOL (Grant No-768686).

Aquest treball d'investigació, amb data de defensa del 20 de Setembre de 2019, té com a membres del tribunal a:

- President: Dra. Cecilia Jimenez-Jorquera, Investigadora Científica CSIC Institut de Microelectrònica de Barcelona, CSIC.

- Secretari: Dr. Jordi Poater Teixidor, ICREA Research Professor, Departament de Química Inorgànica i Orgànica, Universitat de Barcelona.

- Vocal: Dra Maria Isabel Romero Garcia , Professora titular del Department de Química, Universitat de Girona.

Com a membres suplents:

- Suplent 1: Dr. Gonzalo Guirado, Professor Titular, Department de Química, Universitat de Autónoma de Barcelona.

- Suplent 2: Prof. Miquel Sola Puig, Catedràtic d'Universitat, Institut de Química Computacional i Catàlisi, Universitat de Girona.

Acknowledgements

The successful completion of any doctoral thesis requires a great deal of hard work, perseverance and sacrifice, none of which can be achieved without the continuous support of people around you. Consequently, though only a single person gets the title of "Doctor" at the end of a thesis, in reality, it is the fruitful completion of the endeavours of a whole host of people. Hence, there are a lot of people I need to thank for having helped me reach this point.

The first thanks go to my supervisor, Prof. Francesc Teixidor, for trusting in me enough to offer me the position of a pre-doctoral researcher in his group. This thesis would not have been possible without continuous encouragement and expert knowledge. I'm grateful not only for his scientific guidance and expertise, but also for the numerous other discussions we have about a whole host of topics, where even though we may not always agree, have helped me understand the world around me much better. I'm honoured to have known him not only as a great scientist, but also as a wonderful person.

Next, I would like to thank Prof. Clara Vinas, who played a vital part in shaping my thesis. Her scientific knowledge and guidance helped prevent many a pitfall over the course of these last 4 years. Her warm disposition and cheerful demeanour, even in the face of adversity, have been a continuous source of inspiration for me. It is not only her unparalleled scientific knowledge that set her apart, but also her ability to always work with a smile on her face.

I would also like to extend my gratitude to Dr. Rosario Nunez and Dr. Jose Giner for their wise presence. A big thanks to Rosario for her wonderful efforts in not only maintaining the lab, but also for organizing activities outside the lab such as group excursions and lunches which always helped keep the morale of the group high.

I'm indebted to Prof. Xavier Obradors, Director of ICMAB for accepting me as a part of this institution. A big thanks to Sonia and Pietat and all the administrative department for helping with my contract and other administrative work. A special mention to Anna May for her tireless efforts in organizing various seminars, workshops, lectures and so on at ICMAB to make sure there is never any dearth of new learning opportunities. I would also like

to thank the coordinators of the UAB Chemistry department for accepting me in their doctoral program and Prof. Josep Ros Badosa for agreeing to be my tutor. A big thank you to Elena Jimenez, for putting up with my numerous queries and patiently resolving all of them. Without her support, it would have been extremely difficult to navigate the various administrative issues over the course of my thesis.

I spent 6 months of my thesis in Lyon at Institut des Sciences Analytiques (ISA) in the wonderful group of Prof. Abdelhamid Errachid. I would like to extend my gratitude towards him for accepting me in his group and for his guidance during my time there. I would also like to thank my colleagues there, the now doctors Juan Gallardo-Gonzalez and Selim Boudjaoui for their cheerful presence and support in the lab and office and for our numerous discussions and debates on a range of topics. Thank you Juan for being such a patient teacher and teaching me all about potentiometry and Cyclic Voltammetry, without your guidance, my stay in Lyon would not have been as fruitful as it was. A big thanks also to Dr. Abdellatif Baraket for being a great help when I was new to Lyon, in helping me with everything that eased the settling down process in a new place. Thank you to Dr. Nadia Zine for her scientific guidance and support.

I required the help and expertise of a number of technicians with characterization techniques during my thesis, so a big thank you to all of them, but a special mention to Judit Oro and Belen Ballesteros (of ICN2), for their enthusiasm and drive to go beyond the bare minimum and having the patience and perseverance to keep analysing the samples until we found what we were looking for.

My thesis could not have been completed without the support and encouragement of my group members. Thanks to Jordi Cortes for maintaining the labs and making sure we knew where to look when finding something. I would like to specially thank the now doctors Victor, Adnana, Justo and Elena for their guidance when I was new to the lab and office. You were all fantastic teachers when I was new here and without your efforts, I wouldn't have mastered the ins and outs of working in the lab.

A big thanks to Isa and Bego, we all started here at nearly the same time and grew up in the lab together. There are a thousand little things to thank you for, from help with Spanish and Catalan, to help

with work in the lab. It has been a pleasure to share the bulk of my time here with you guys.

I would also like to thank the other members of the group, both past and present, who made my time here highly interesting. Flavia, Lei, Ines, Mahdi, Isabel Guerrero, Joan, Sara, Raquel, Miquel, Pol, thank you to all of you. I would like to wish good luck to the newest members of the group, Sohini and Zhen Li. A special mention to Albert and Zsolt, the experienced heads in the lab, for sharing their wisdom and experiences with me, not only about work but about other things as well. I'm really happy I was able to meet and work with you guys.

I would not have been able to reach this point of my life without my family. The word "thanks" is not enough to acknowledge the contribution of my parents, who raised me and made me capable enough to be able to succeed with my thesis, but nevertheless, I would like to thank them for everything. Thank you to my brother for always being there and making sure I didn't have to worry about home whilst I was here, knowing he was there.

Finally, I would like to thank the person without whom I would not have survived here, be it at work or at home. There are no words I have that can express my gratitude, so I am not even going to attempt it, I hope you already know everything I would want to say- Thank you Arpita.

I'm sure I've missed some people who deserve my gratitude and acknowledgment in having made my time here a success, so I apologise if I'm not mentioned you by name. A big Thank You to everyone for everything you have taught me.

Organització del Manuscrit

D'acord amb la normativa vigent i prèvia acceptació de la Comissió de Doctorat de la Universitat Autònoma de Barcelona, aquesta memòria es presenta com a compendi de publicacions, presentats i acceptats per la Comissió de Doctorat en Química de la UAB, el 3rd de Juny de 2019. Els treballs inclosos en aquesta memòria són els següents:

- A novel potentiometric microsensor for real-time detection of Irgarol using the ion-pair complex $[Irgarol\text{-}H]^+[Co(C_2B_9H_{11})_2]^-$, A. Saini, J. Gallardo-Gonzalez, A. Baraket, I. Fuentes, C. Vinas, N. Zine, J. Bausells, F. Teixidor, A. Errachid., *Sensors and Actuators B*, **268** (2018) 164–169.
  DOI: doi.org/10.1016/j.snb.2018.04.070

- A simple membrane with the electroactive $[Sulfapyridine\text{-}H]^+[Co(C_2B_9H_{11})_2]^-$ for the easy potentiometric detection of sulphonamides, A. Saini, I. Fuentes, C. Vinas, N. Zine, J. Bausells, A. Errachid, F. Teixidor., *Journal of Organometallic Chemistry,* **893** (2019) 32-38.
  DOI: doi.org/10.1016/j.jorganchem.2019.04.030

- A highly selective potentiometric amphetamine microsensor based on all-solid-state membrane using a new ion-pair complex,$[3,3'\text{-}Co(1,2\text{-}closo\text{-}C_2B_9H_{11})_2]^-[C_9H_{13}NH]^+$, J. Gallardo-Gonzalez, A. Saini, A. Baraket, S. Boudjaoui, A. Alcacer, A.

Streklas, F. Teixidor, N. Zine, J. Bausells, A. Errachid., *Sensors and Actuators B,* **266** (2018) 823–829.
DOI: doi.org/10.1016/j.snb.2018.04.001

Abbreviations

ECSA	Electron Confined Space Analogy
ISE	Ion Selective Electrode
PVC	Polyvinyl Chloride
AgCl	Silver Chloride
KCl	Potassium Chloride
SSM	Seperate Solution Method
FIM	Fixed Interference Method
K_{ij}^{pot}	Nicolsky Coefficient
POT	Polytrioctylthiophene
PEDOT	Polyethylenedioxythiophene
PANI	Polyaniline
Ppy	Polypyrrole
o-NPOE	o-nitrophenyloctyl ether
DOS	Bis (2-ethyl hexyl) Sebacate
DBP	Dibutyl Phthalate
DOP	Dioctyl Phthalate
ATRA	Atom Transfer Radical Addition
$ClP(NMe_2)_2$	Bis(dimethylamino)chlorophosphine
BuLi	n-Butyllithium
QDs	Quantum Dots
QNCs	Quantum Nanocrystals
QR_{ods}	Quantum Rods
QRs	Quantum Rings
CdSe	Cadmium Selenide
r_B	Bohr's Exciton Radius
UV	Ultraviolet
QY	Quantum Yield
TOPO	Tri-octylphosphine oxide
GC-NPD	Gas Chromatography-Nitrogen Phosphorous Detector
GC-MS SIM	Gas Chromatography- Mass Spectroscopy in Selected Ion Monitoring Mode
ESI-MS/MS	Electrospray Ionization Mass Spectroscopy with Tandem Mass Spectroscopy
ELISA	Enzyme Linked Immunosorbent Assay
NMR	Nuclear Magnetic Resonance
FTIR	Fourier Transform Infrared Spectroscopy

EA	Elemental Analysis
MALDI-TOF-MS	Matrix Assisted Laser Desorption/Ionization-Time of Flight Mass Spectroscopy
PECVD	Plasma Enhaced Chemical Vapor Deposition
PCB	Printed Circuit Board
CV	Cyclic Voltammetry
SCE	Saturated Calomel Electrode
WE	Working Electrode
GSAM	General Standard Addition Method
EMF	Electromotive Force
ATS	Amphetamine Type Stimulants
NFA	N-formyl Amphetamine
BMK	Phenylacetone
HPLC-MS/MS	High Performance Liquid Chromatography- Mass Spectroscopy
S-K	Stranski- Krastanov
DE	Droplet Epitaxy
PTFE	Polytetrafluoroethylene
TEM	Transmission Electron Microscope
STEM	Scanning Transmission Electron Microscope
HRTEM	High Resolution Transmission Electron Microscope
EELS	Electron Energy Loss Spectroscopy
EDX	Energy Disperse X-Ray
PL	Photoluminescence
CMC	Critical Micelle Concentration
ICP-MS	Inductive coupled plasma- mass spectroscopy
QTPs	Quantum Tetrapods
EGM-2	Endothelial cell growth medium 2
RPMI	Roswell Park Memorial Institute culture media
EFTEM	Energy filtered TEM
ICP-MS	Inductive coupled plasma-mass spectroscopy
Au NPs	Gold nanoparticles
POC	Point of Care
MNP@Au	Gold coated Magnetic Nanoparticles
H[COSAN]	Cobaltabis(dicarbollide)

$Ø_{carbSH}$	Diameter of *ortho*-carboranethiol sphere
$Ø_{TEM}$	Diameter measured from TEM
N_A	Avogadro's Number
XPS	X-Ray Photoelectron Spectroscopy
FWHM	Full width Half Maxima
NPs	Nanoparticles
UV-vis	Ultraviolet- visible
SEM	Scanning Electron Microscope
HAADF	High-angle annular dark field
MNPs	Magnetic Nanoparticles
SAED	Selected Area Electron Diffraction
SQUID	Superconductive Quantum Interference Device
HOMO	Highest occupied molecular orbital
LUMO	Lowest unoccupied molecular orbital
SPR	Surface Plasmon Resonance
TOAB	Trioctylammonium bromide

Summary of the Thesis

The research presented in this thesis has been summarized as a compendium of articles published and to be published in the future. There are five chapters dealing with the results and discussions. The results and discussions are preceded by a general introduction and objectives. The summary of each chaper of the results is given below.

- In the first chapter, a micro Ion Selective Electrode (ISE) based on an ion pair complex $[C_{11}H_{20}N_5S][Co(C_2B_9H_{11})_2]$ has been described for the potentiometric detection of the algaecide Irgarol in water. The use of the metallacarborane anion $[Co(C_2B_9H_{11})_2]^-$ in conjunction with the target ion (in this case Irgarol) to form an ion pair complex to be incorporated in a polymeric (PVC) membrane leads to enhanced selectivity and sensitivity of the ISEs. The ISE described in this chapter showed extremely promising results and the lowest detection limit achieved was 2×10^{-6} mol/dm^3 and it showed a stable response between pH 6 and 12, making it ideal for use in water. It also showed great selectivity in presence of interfering ions belonging to the same class of compounds as Irgarol.
- In the second chapter, the strategy of using the $[Co(C_2B_9H_{11})_2]^-$ anion as the electroactive component in the polymeric membrane of a micro ISE was further utilized for the detection of the Sulphonamides class of compounds in water, taking Sulfapyridine as an example. The ISE described in this chapter showed a lowest limit of detection of 1×10^{-6} mol/dm^3 and a stable response between pH 6 and 9, allowing for its use in water. It was at least 2 orders of magnitude more selective towards the target ion (Sulfapyridine) than any other compound belonging to the Sulphonamides class of compounds.
- The third chapter deals with the detection of the illicit drug Amphetamine in wastewater. Methods used for production of Amphetamine by illicit small scale factories often lead to a huge amount of liquid waste, containing

traces of Amphetamine, which is dumped in wastewater. Detection of Amphetamine in wastewater can make it easy to pinpoint the location of these illicit factories. A micro ISE based on ion pair complex contianing the $[Co(C_2B_9H_{11})_2]^-$ anion was used for potentiometric detection of Amphetamine in wastewater, leading to a lowest detection limit of 1 x 10^{-5} mol/dm^3, the best amongst existing potentiometric sensors for Amphetamine detection, and a working pH range of 1.5-8.5.

- In the fourth chapter, carboranyl derivatives were used as capping agents for the production of CdSe Quantum Nanocrystals (QNCs). CdSe Quantum Dots, Quantum Rods, Quantum Rings and Quantum Tetrapods were produced using a simple colloidal synthesis method. The method for the production of all these QNCs was identical, except for the use of different carboranyl ligands as capping agents. A slight modification in the carboranyl derivative used as capping agent led to the formation of a different morpholigy in the quantum regime. All the QNCs produced showed intense photoluminescence, high Quantum Yield and a long, stable lifetime. All the QNCs were thoroughly characterized to check for their composition, Quantum Yield and Photoluminescent Emission intensity.
- In the fifth and final chapter, *ortho*-carboranethiol capped gold nanoparticles (Au NPs) were synthesied which showed the unique property of being able to transfer between aqeuous and organic phases. It was demonstrated that the phase transfer occurred upon using, divalent, trivalent and tetravalent cations. Fe^{3+}, Ni^{2+}, Mn^{2+}, Ce^{4+} were amongst the cations that tested successfully in this phase transfer system. This further demonstrated the use of carboranyl spheres acting as vehicles for transfer of ions from aqueous to organic phase, making them ideal for ion transport in biomedical applications. It was observed that the carboranyl spheres are present on the surface of the ions to be transported, creating a kind of charged ionic pool which upon the application of a little kinetic energy, releases energy allowing the ions to transfer from one phase to another. Further, as part of the European Union

Horizon 2020 KardiaTool project, Gold coated Fe_3O_4 magnetic nanoparticles (MNP@Au) decorated with amine and $H[Co(C_2B_9H_{11})_2]$ (labelled as H[COSAN]) were synthesized and characterized. The incorporation of H[COSAN] in this complex allows for its use a sensing layer in a Point of Care device for early diagnosis of heart failure. The use of H[COSAN] is due to its nature as a redox specie which has a tuneable HOMO-LUMO which enhances the possibility of using it in sensing applications.

Table of Contents

1. Introduction

Abhishek Saini
ICMAB-CSIC (UAB)

CONTENTS

1.1 Carboranes

Carboranes are polyhedral clusters of Boron with Carbon atoms incorporated into their structure. Due to the Nobel prize winning research of W.N. Lipscomb, it was found that polyhedral boron clusters could be described as species having occupied orbitals and multicentric bonds in different resonant forms. Due to the work of H.C. Brown it was also discovered that BH units show great reducing effect over unsaturated organic and hence could have an effect on organic synthesis. [1-6]

Boranes may be defined as neutral or anionic boron clusters which are formed by triangular faced polyhedra containing a BH unit for each vertex. It has also been demonstrated that Boranes can act as aromatic compounds. [7] Recently, it has been established that hydrocarbon and borohydride chemistries are quite similar to each other since they have a common root regulated by number of valence electrons in a confined space. Application of the Electronic Confined Space Analogy (ECSA) method further reinforces the similarities between fundamental aromatic hydrocarbons and analogous closo B-H clusters. [8-9] When one of the vertices of the Boranes is substituted by a heteroatom, such as carbon, it gives rise to a family of heteroboranes amongst which Carboranes are the most studied ones. These carboranes have at least one boron atom replaced by a carbon atom.

The empirical formula of these compounds is $[C_nB_mH_{n+m+p}]^{x-}$ where n is the number of C atoms within

the vertices of the cluster, m is the number of B atoms within the cluster and p is the number of bridging H.

These clusters are consistent with some electronic requirements that lead to a tridimensional structure. If the number of electron pairs maintaining the cluster together is n+1(where n is the number of occupied vertices in the cluster) then the structure of the compound is known as closo, if it is n+2, it is known as nido, if it is n+3 it is known as archano. [10]

1.1.1 Metallacarboranes

Metallacarboranes can be synthesized by reacting $[C_2B_9H_{12}]^-$ or its conjugate base $[C_2B_9H11]^{2-}$ with metal containing reagents in which the metal atom fills the vacancy and completes a 12 vertex closo icosahedral cage. Anionic icosahedral metallocarboranes, $[3,3'\text{-}M(1,2\text{-}C_2B_9H_{11})_2]^{n-}$ can be generated where M=Co(III), Fe(III), Fe(II) and n=1 or 2.

The first metallacarborane $[3,3'\text{-}\ Fe(1,2\text{-}C_2B_9H_{12})_2]^{n-}$ where n=1,2 was reported in 1965. [11]. This was closely followed by the synthesis of the cobaltabis(dicarbollide) $[3,3'\text{-}Co(1,2\text{-}C_2B_9H_{12})_2]^-$ as represented in **Fig. 1**. [11] This anion features low nucleophilic character, high molecular volume, high chemical stability and low charge density due to the distribution of the negative charge between 45 atoms. [12]

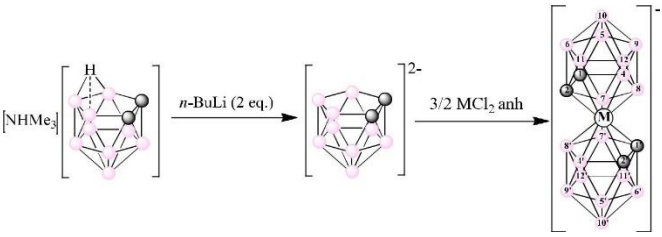

Figure 1. Schematic for synthesis of cobaltabis(dicarbollide) and ferrabis(dicarbollide). M=Co, Fe.

Recently, a new green synthetic method for the synthesis of metallacarboranes was reported by Vinas and Co. which facilitates a quick and solvent free synthesis. [13]

Work done in this thesis is more focused on the cobaltabis(dicarbollide) anion, depicted in **Fig. 2.** Along with it's low nucleophilic character, the cobaltabis(dicarbollide) anion is part of the weakly coordinating class of anions. [14-15] It has a relatively large size and its terminal hydrogens show a hydride character. This is thought to be one of the main causes of high degree of dissociation of strong free conjugate acids along with delocalized charge spread over the surface of the anion. This leads to a unique hydrophobic character of all cobaltabis(dicarbollide) derivatives. The salts and free conjugate acids of the bis-icosahedral cobaltabis(dicarbollide) show good solubility in medium polarity solvents like ethers, nitro-solvents, halogenated solvents, etc. [16] Perhaps the most important property of the cobaltasbis(dicarbollide) anion, in the context of the work done in this thesis, is its ability to form weak B–H···H–N dihydrogen bonds isolated with protonated amino compounds. [17] It also has the capability to self-

assemble through $C_{cluster}$–H···H–B dihydrogen bonds, and to be non-covalently bonded to plasticizers through $C_{cluster}$–H···O hydrogen bonds. Due to its many unique and fascinating properties, Cobaltabis(dicarbollide) anion has found use as doping agent on intelligent membranes for ion capture [12]. It has also found widespread use as doping agent for polypyrrole solid-contact layers to be used in solid-contact Ion Selective Electrodes. The presence of cobaltabis(dicarbollide) anion in these contact layers leads to an improved thermal stability and a marked improvement of the contact's overoxidation threshold, thus greatly improving its electric properties. [18–25].

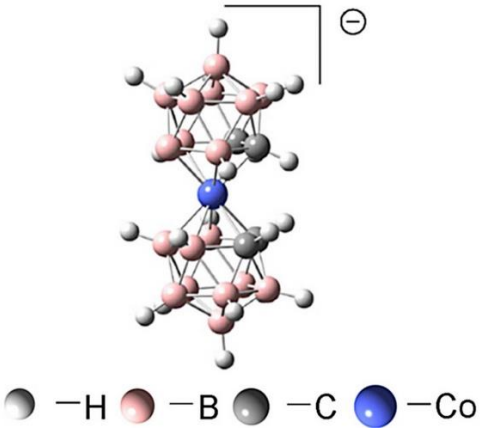

Figure 2. Chemical structure of Cobaltabis(dicarbollide) anion, [3,3'-Co(1,2-$C_2B_9H_{11}$)$_2$]$^-$ [26].

Since the first part of this thesis deals with using the cobaltabis(dicarbolide) anion in Ion Selective Electrodes for potentiometric detection, here follows a brief overview

of the various principles and components involved in potentiometric detection using Ion Selective Electrodes.

1.1.1.1 Ion Selective Electrode and Ionophores

An Ion Selective Electrode (ISE) is a sensor that converts the activity of a specific ion dissolved in a solution into an electric potential, where the voltage is theoretically dependent on the logarithm of the ionic activity. [27] They have found widespread use as basic tools of analytical detection over the past decades.

One of the most important components of these class of sensors are lipophilic complexing agents capable of reversibly binding ions, referred to as ionophores or ion carriers, so named due to their ability to transport ions across hydrophobic membranes. The sensing part of an ISE is its polymeric membrane, which comprises of a polymeric matrix, an appropriate plasticizer and a mixture of an ionophore and an ion exchanger. The viability of an ISE is determined by its most important parameters- Sensitivity and Selectivity. Sensitivity can be defined as the response of the sensor to the activity of the target ion. The larger the sensitivity range, more viable is the ISE. On the other hand, selectivity is the sensitivity of the ISE only to the target ion and not any other ions or compounds in the vicinity (referred to as interferences). It is dependent on the equilibrium constant of the exchange reaction of primary and interfering ions between the polymeric membrane and the media to be analysed. It strongly depends on the ratio of complex formation constants of these ions with the ionophore in the membrane phase.

Traditionally, ionophores were electrically charged species, but advancements were made in using neutral ionophores in ISE. Antibiotics were amongst the first neutral ionophores to be incorporated in ISEs and it was discovered that many neutral ionophores form complexes with certain target cations, thus increasing invitro selectivity of ISEs. [28-30]

Another important milestone in the field of ISEs was achieved in 1967, when the first solvent polymeric membranes were developed, using PVC as the polymer matrix. [31-32] Since then use of PVC as the polymeric matrix has become the standard for ionophore based ISEs.

The basic theory for potentiometric response of ISEs has been the same for many years. The response of an ISE membrane is measured under zero-current apparatus, in a classical galvanic cell, which comprises of: Ag │AgCl│ reference electrolyte (saturated KCl) **::** sample solution ‖ ion-selective membrane ‖ internal filling solution │AgCl │ Ag. A schematic of such a cell is depicted below in **Fig. 3**.

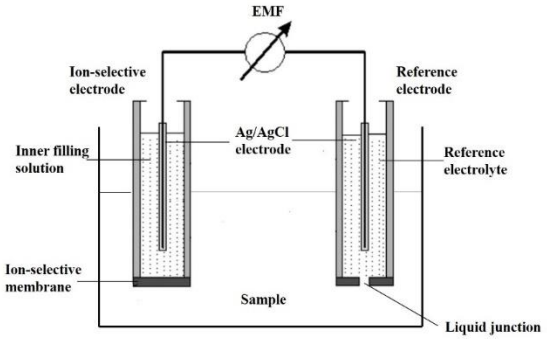

Figure 3. A classic liquid-membrane ISE cell assembly. [33]

The potentiometric response of any ISE is measured against the Nernst Equation:

$$E = E^0 + \frac{RT}{zF} \ln a_I(aq)$$

where E is the potential of the membrane, E^0 is the standard potential, a_I is the activity of the uncomplexed ion in an aqueous solution. R is universal gas constant, T is the absolute temperature, F is the Faraday constant and z is the number of valence electrons.

For monovalent species, such as those studied during the course of this thesis, the E should be 59mV/decade to be classified as a perfect Nernstian response. The thickness and composition of the polymer layer needs to be kept constant in order to achieve reproducible Nernstian response. Practically, it is very difficult to achieve a perfect Nernstian response due to certain abnormalities that occur when performing measurements such as ionophore lixiviation from the polymeric membrane, limited hydrophobicity of the plasticizer or permselectivity to counterions among others. [34-35] Since achieving a perfect Nernstian response is quite rare, the viability of an ISE is judged by how close its performance is to a perfect Nernstian response.

To measure the selectivity of an ISE, the Nicolsky-Eisenmann equation is the most widely used tool. [36] Although there have been several reports detailing new methods for calculating the selectivity, especially for mixed ion response of solvent polymeric membrane based on the phase boundary potential [36–38], the Nicolsky coefficient of selectivity is still the most widely used

despite being limited to the comparison of ions with the same charge. [35] According to the Nicolsky-Eisenmann equation, the activity term in the Nernst equation can be modified as:

$$E = E_I^0 + \frac{RT}{z_I F}\ln(a_I(IJ) + K_{IJ}^{Pot} a_j(IJ)^{z_I/z_j})$$

where a_I(IJ) is the activity of the target ion and a_J(IJ)is the activity of the interfering ion. z_i and z_j refer to the charge of the target ion and the interfering ion respectively. For extremely selective ISEs, the Nicolsky coefficient K_{IJ}^{pot}, is very small and the potential E, observed is mostly dependant of a_I(I) as in the case of ion-pair complex based ISEs, as elaborated later.

To obtain the potentiometric coefficient K_{IJ}^{pot} there are two different methods- separate solution method (SSM) and the fixed interference method (FIM). [37] In this thesis, the Fixed Interference Method (FIM) has been used. According to the FIM, the calibration curve is obtained by titration of the primary ion in the presence of a fixed background of interference. Therefore, the calculation of the K_{IJ}^{pot}, can be obtained as follows:

$$K_{IJ}^{Pot} = \exp\{\frac{(E_J^0 - E_I^0)z_I F}{RT}\}$$

where E_j is the potential of the interfering ion and E_i is the potential of the target ion.

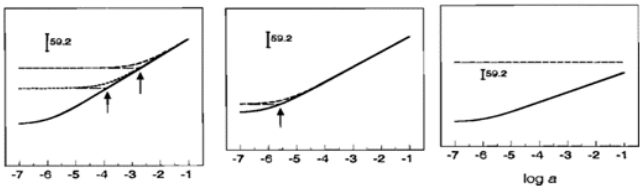

Figure 4. Representation of Fixed Interference Method. [37]

Fig. 4 represents the fixed interference method (FIM) under ideal (left) and nonideal conditions (centre and right). Solid lines, response to primary ion; dashed and dotted lines, monovalent and divalent interfering ions, respectively. In the case of the FIM, information about the electrode slope for the response of the interfering ion should be obtained in additional experiments. The experiment can be mainly biased by the lower (in centre image) or the upper detection limit (right image). For situation in the centre image, only a maximum selectivity coefficient can be reported; the highest possible activity of the interfering ion should be used. [37]

1.1.1.2 Ion Pair Complexes

Ion-pair complexes are thought of as ion exchangers which show increased selectivity towards a primary ion when compared to neutral ionophores which associate with ions in a more non-specific way. As a result, they can be referred to as charged ion-carriers or charged ionophores. [39]

Lipophilic anions such as the potassium salts of tetraphenylboric acid derivatives were amongst the first ion exchangers reported in literature. This was followed by lipophilic cations such as salts of tetraalkylammonium,

tetraalkylphosphonium and tetraalkylarsonium. [40] Commonly, ion exchangers are lipophilic salts with acid/base properties that dissociate in the polymeric membrane. For classic ion exchangers, this dissociation leads a lipophilic anion and a hydrophilic cation. The anion being lipophilic is necessary so as to prevent any leaking (lixiviation) of the salt from the membrane to the aqueous phase. The hydrophilicity of the cation can vary a lot since it can be of either inorganic or organic origin. But it must be capable of crossing the interface between the membrane and aqueous phase and distributing itself reversibly. Due to the macroscopic electroneutrality, the total number of hydrophilic ions in a membrane always equals the amount of ion-exchanger sites, regardless of the dissociation degree. The interaction between ions is governed by electrostatic forces and hence is not very strong, contributing to the low selectivity in ion exchanger based ISEs.

The charged ionophores called as Ion Pair complexes bind ions in a more strong and complex bonding than mere electrostatic interaction. [41,35,39,42] The strength of association constants in Ion pair complexes has been found to be several magnitudes higher than those in ion exchangers. [43-45] As a result, we can say that ISEs based on charged ionophores (Ion pair complexes) show much higher selectivity towards the primary target ion than ISEs based on Ion exchangers.

While Ion Pair complexes based ISEs have been widely used for potentiometric detection, for detection of Ca^{2+}, alkali earth metals and even pharmaceutical drugs [46-51], they were not used for detecting biological markers until

2008. Stoica et al., pioneered the use of Ion Pair complexes using a nitrogenous base and the cobaltabis(dicarbollide) anion. [52] The cobaltabis(dicarbollide) anion was used in conjunction with nitrogenous base of the type $[R\text{-}NH]^+$ to produce two novel ion-pair complexes which were incorporated into PVC-type potentiometric sensors for the detection of isoniazide and pyrazinamide in the application of tuberculosis drug analysis. This was the first time an ISE based on the ion pair complex of the type $[cation\text{-}NH]^{n+}n[3,3'\text{-}Co(1,2\text{-}C_2B_9H_{11})_2]^-$ had been used and it paved the way for using this type of complex for the detection of almost any compound with a protonable amine group. Since then, the cobaltabis(dicarbollide) anion has been established as an ideal hydrophobic anion for use in Ion pair complexes based ISEs. [53-54]

The advantage of using cobaltabis(dicarbollide) anion stem from its advantages over traditional ion exchangers. The traditional ion exchangers over time, suffer from a loss of ions and hence decrease in sensitivity and selectivity. On the other hand, cobaltabis(dicarbollide) can be non-covalently bonded to the plasticizer through $C_{cluster}$-H···O hydrogen bond and produce weak B-H···H-N dihydrogen bonds with the electro-active cations leading to improved stability of the membrane. Its ability to produce B–H···H–N dihydrogen bonds with the protonated amines of the antibiotics to be detected further enhance the stability and hence sensitivity.

It also shows a massive advantage in increasing selectivity when compared to traditional ion exchangers. Due to the electronegativity difference between B and C relative to H, we can say the B-H and C-H bonds have inverted

polarities. This causes the B-H bond to have tendency to generate hydrogen and dihydrogen bonding. On the other hand, the C-H bonds in the $[Co(C_2B_9H_{11})_2]^-$ are also more polarized than usual in organic compounds. This also facilitates hydrogen and dihydrogen bonding. This leads to $[Co(C_2B_9H_{11})_2]^-$ acting as a thistle, particularly with molecules having the opportunity to generate hydrogen bonding and their interaction with amines and protonated amines is very strong. This is, the remarkable aspect that this anion provides stability to all participating agents in the membrane. In principle the anion $[Co(C_2B_9H_{11})_2]^-$ is not the sensing part, but the cation (the $NRR'H^+$) that leads to the selectivity

The reasons for using the cobaltabis(dicarbollide) anion to form ion pair complexes with protonable amine groups for detection of the respective antibiotics have been further elaborated in Section 3.1-3.3 of the Results and Discussions Section.

1.1.1.3 Conducting Polymer Layer

Miniaturizing of ISEs provides certain challenges, such as stability of the solid state (micro) ISEs. This is because in conventional ISEs, the internal filling solution is responsible for the stability of the ISE, but in micro-ISEs this solution is removed, thus leading to reduced stability and also poor reproducibility. [39] To counter this problem, the use of conducting polymers was proposed. The solid-contact (micro) ISEs comprise of an electronically conducting substrate covered with a transducer layer and a sensitive membrane on the top of the transducer (sensing) layer. Conducting polymers are

mostly p-type semiconductors which are oxidized and doped with anions to maintain the macroscopic electroneutrality. Conducting Polymers work as transducers from ionic to electronic conductivity due to the doping/de-doping in conjunction with the oxidation-reduction of the polymer. The conducting polymers provide another advantage, since they can be cast into the desired shape that covers the entire area of the electroactive region, thus improving the adhesion of the sensitive membrane, which results in improvement of the mechanical contact of the sensitive layer with the metal transducer surface. Polythiophenes such as polytrioctylthiophene (POT), polyethylenedioxythiophene (PEDOT), polyaniline (PANI), and polypyrrole (PPy) are the most popular conducting polymers reported in literature.

The electrochemical properties of a conducting polymer layer can be altered by changing the doping ion which compensates the polymer's electrical charge. The use of the $[3,3'\text{-}Co(1,2\text{-}C_2B_9H_{11})_2]^-$,as doping anion in Ppy conductive polymers plays precisely this role. Using the cobaltabis(dicarbollide) anion as a doping agent on PPy conducting layers leads to improved thermal stability and a marked improvement in the electrical conductivity of the ISE. (**Fig. 5**) [18–25,55].

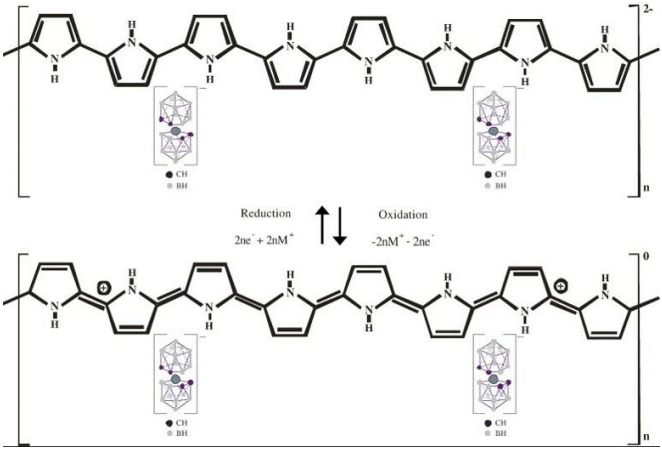

Figure 5. Charge delocalization in [Ppy][3,3′-Co(1,2-$C_2B_9H_{11})_2$] layer. [56]

1.1.1.4 Role of Plasticizers

Plasticizers are an important component of the sensitive polymeric membrane. While not directly responsible for sensing of the target ion, they nevertheless are play the crucial role of membrane solvent. They ensure mobility of the ions and ionophore through the polymeric membrane. Since, the Glass transition temperature of PVC is around 100^{o}C and most of the ISE measurements are done at room temperature [57-58], without the plasticizers, the mobility of ions in the polymeric membrane will be greatly hindered.

A plasticizer should ideally fulfil certain critical criteria-

- Be sufficiently lipophilic
- Must not crystallize in membrane phase
- No exudation

It has been observed that the lower the value of dielectric constant (ε) is, the less the affinity of the species to the membrane. [59] Hence, low polar plasticizers are generally unfavourable for ISEs for detection of divalent ions, while polar plasticizers are unsuitable for monovalent ions.

o-nitrophenyloctyl ether (o-NPOE) and Bis (2-ethyl hexyl) Sebacate (DOS) are established in literature as plasticizers showing the longest lifetimes when incorporated in polymeric membranes. [60] Dibutyl Phthalate (DBP) and Dioctyl Phthalate (DOP) are the two other plasticizers used in the work described in this thesis (**Fig. 6**)

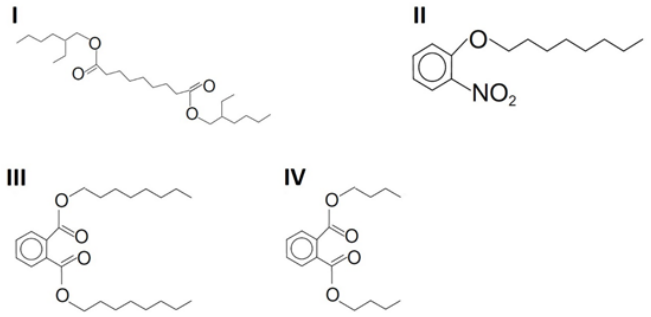

Figure 6. Structures of the plasticizers used in this thesis. **I**, di-octyl sebacate (DOS). **II**, o-nitrophenyloctly ether (o-NPOE). **III**, di-octyl phthalate (DOP). **IV**, di-butyl phthalate (DBP).

1.1.2 Carboranyl Ligands

The second part of this thesis deals with the use of spherical carboranyl ligands acting as capping agents for the synthesis of innovative Quantum nanocrystals and

gold nanoparticles. Icosahedral dicarba-*closo*-dodecacarboranes ($C_2B_{10}H_{12}$) have been used for this purpose. Below follows a brief overview of the carboranyl ligands used in this work as well as a brief introduction to Quantum nanocrystals and their basic principles.

1.1.2.1 Thiol derivatives of icosahedral dicarba-*closo*-dodecarboranes

The icosahedral dicarba-*closo*-dodecarboranes have 3 isomers as shown in **Fig. 7.**

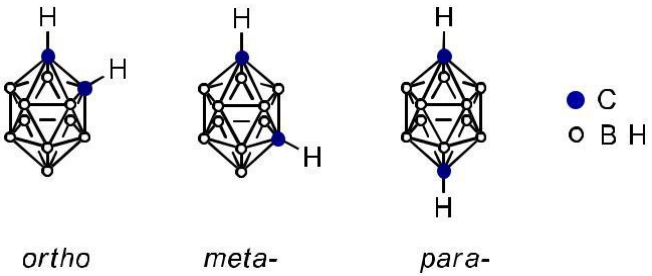

Figure 7. The three isomers of icosahedral dicarba-*closo*-dodecarboranes ($C_2B_{10}H_{12}$).

The *ortho-* and *meta-* carborane clusters show high reactivity given the right chemical conditions. Both these isomers demonstrate similar reactivity in terms of electrophilic substitution at the C_c-H carbon cluster vertices. In both cases, the hydrogen atoms of the C_c-H units show more acidity than those bonded to B-H vertices and hence, hydrogen atoms attached to carbon can be considered as acidic, although weakly acidic, while those bonded to boron are considered as hydride. The acidity and hence, the vulnerability to get deprotonated of the C_c-H vertices is more in *ortho-* than *meta-* clusters. This acidic

character of the C_c units allows for their feasible deprotonation using strong alkali and alkaline earth metal bases, n-butyllithium being the primary example. The negative charge generated on the carbon atom of the cluster following the deprotonation, attracts electrophilic reagents, opening the way for the introduction of functional groups at the C_c position of the cluster.

There are two ways for the substitution of one or both of the C_c atoms as shown in **Fig. 8.**

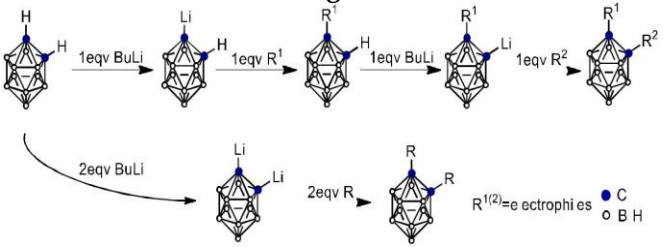

Figure 8. Deprotonation reaction of Cc-H units followed by substitution with electrophilic agents. [61]

The synthesis of monosubstituted carborane derivatives is more difficult compared to disubstituted due to the disproportionation of Li[1,2-$C_2B_{10}H_{11}$] into Li_2[1,2-$C_2B_{10}H_{10}$] and 1,2-$C_2B_{10}H_{12}$. [10] Many techniques have been proposed to overcome this problem, [62-64] but the most efficient and simple was found to be performing the monosubstitution reactions in ethereal solvents. It was found that the reaction worked best when performed at low temperature and with specific carborane concentration. It has been reported that depending on type of electrophile it is possible to find combination of conditions (chelating or non-chelating solvent,

temperature, carborane concentration) that facilitate the largest degree of monosubstitution. [65]

Bearing the above in mind, the thiol substitution of one of the C_c atoms was done on an *ortho*-carborane as depicted by the following schematic:

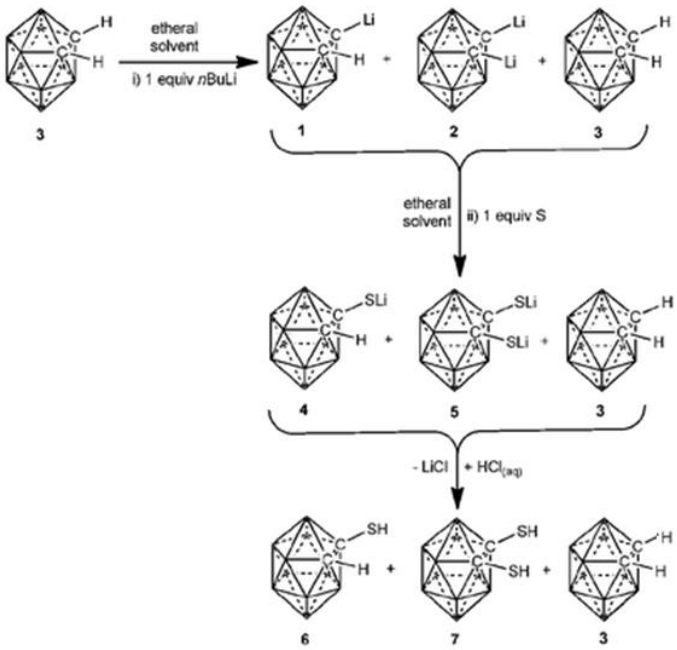

Figure 9. Synthesis procedure of *ortho*-carboranethiol. [63]

This 1-SH-1,2-$C_2B_{10}H_{12}$ has been referred to as *ortho*-carboranethiol further in this thesis.

For the synthesis of thiol derivatives of *meta*-carborane as well as the dithiol derivatives of *ortho*- and *meta*-carborane respectively, the reaction procedure is

essentially the same except for a few variations in the reaction temperature and the amount of reagents used.

Similarly, for the synthesis of 1-CH_3-2-SH-1,2- $C_2B_{10}H_{12}$, referred in this thesis as 1-methyl-2-*ortho*-carboranethiol, the same synthesis procedure was followed as for the synthesis of *ortho*-carboranethiol, with the only difference being that the commercially available, 1-CH_3-1,2-$C_2B_{10}H_{12}$ was used as the starting material.

These synthesis reactions have been described in detail in Section 3.4 of the Results and Discussion Section. For the synthesis of carborane capped Quantum Nanocrystals, described in this thesis, *ortho*-carboranethiol, *meta*-carboranethiol, *meta*-dicarboranethiol and 1-methyl-2-*ortho*-carboranethiol have been used and their structures are depicted below in **Fig. 10**.

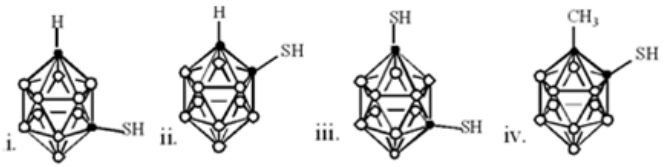

Figure 10. The ligand structures of (i) *meta*-carboranethiol, (ii) *ortho*-carboranethiol, (iii) *meta*-carboranedithiol (iv) 1-methyl-*ortho*-2-carboranethiol

1.1.2.2 Closo-carboranylphosphinic acids

Carboranyl phosphorous compounds, particularly phosphines (Carb-PRR') have been previously reported and are of particular interest due to their potential applications as ligands for organometallic chemistry and

enantioselective catalysis and have found use as catalysts in hydrogenation reaction of terminal [66-71] and internal olefins [72], cyclopropanation [73-74], radical polymerisation of vinyl monomers [75-76] as well as in Kharasch-type reaction, namely the "atom transfer radical addition" (ATRA). [77-79]

The case of phosphinic acids was completely different. They were good as reducing agents, particularly, the derivatives of Hypophosphorous acid $H_2P(O)(OH)$ or its organic equivalent RHP(O)(OH), but the latter received little relevance in coordination chemistry, most probably due to the reducing power of the compound, that prevented the formation and isolation of their metal complexes. The situation changed dramatically with the preparation of the carboranyl phosphinic acids. These compounds due to the electron-withdrawing characteristic of the cluster through C_c [80], did not show a reducing essence and allowed the preparation of some metal complexes and the immediate coordination of the Fe(O) outer layer of the magnetic nanoparticles.[81]

A reproducible synthetic procedure, with a high yield for producing *ortho-* and *meta*-carboranylphosphinic acids and its sodium salts was reported by Vinas and co. and is depicted in **Fig. 11** below. [82]

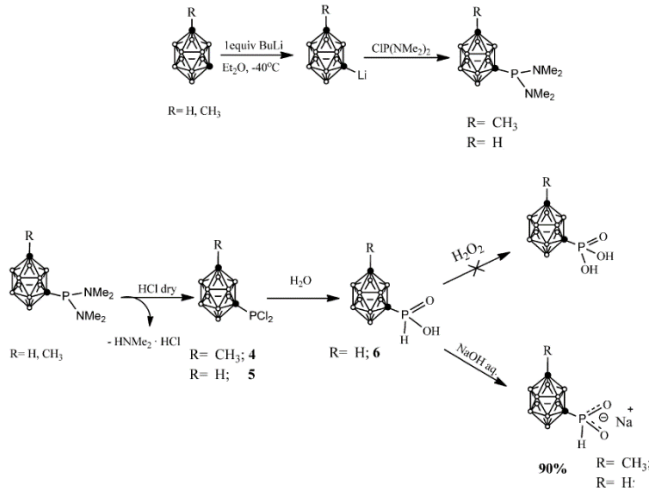

Figure 11. Synthesis procedure of *meta*-carboranyl phosphinic acid and its sodium salt.

The diphosphinic acid derivative of the meta-carborane was achieved by following a similar synthetic procedure as above (**Fig. 12**), the only difference being that twice the amount of n-butyllithium and CIP(NMe2)2 was taken.

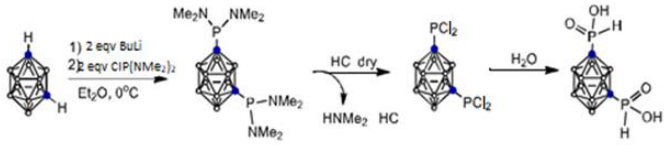

Figure 12. Synthesis of diphosphininc acid derivative of *meta*-carborane.

The monophosphinic and diphosphinic acid derivatives of the *meta*- 1,2-$C_2B_{10}H_{10}$ have been used in this thesis and are referred to *meta*-carboranylphosphinic acid and *meta*-carboranyl diphosphinic acid respectively and are depicted below in **Fig. 13**. Their detailed synthesis procedure has been described in Section 3.4 of the Results and Discussions section.

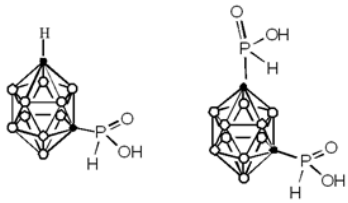

Figure 13. The chemical structures of *meta*-carboranylphosphinic acid (left) and *meta*-carboranyldiphosphinic acid (right).

1.1.2.3 Closo-carboranylcarboxylic acid

The 1-CH_3-2-COOH-1,2-*closo*-$C_2B_{10}H_{10}$ is synthesised following the same reaction conditions as the *meta*-carboranethiol, with the only difference being that dry ice is used instead of Sulphur. For the purpose of the work done in this thesis, only the *meta*- isomer was produced and is referred to as *meta*-carboranylcarboxylic acid henceforth in this thesis. (**Fig. 14**)

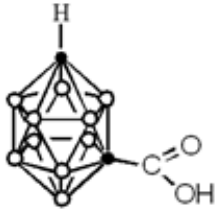

Figure 14. Chemical structure of the *meta*-carboranylcarboxylic acid

1.1.2.4 Quantum Nanostructures

Nanostructured materials have been well established in literature for many years now, with their fascinating properties long ago recognized for use in many applications in the fields of optoelectronics, and more recently in medicine. [83-86]

A solid can be categorized as a nanostructure when it has a particle size of less than 100 nm and it exhibits a distinct variation of optical and electronic properties. A nanostructure made up of a semiconductor material and having dimensions of less than 20 nm is referred to as a Quantum Dot (QD). They are zero dimensional and are the most studied amongst all the Quantum nanostructures, for this reason they have been used an example here to explain some of the basic concepts that apply to all Quantum Nanocrystals (QNCs)- Quantum Rods (QR_{ods}) and Quantum Rings (QRs). QDs typically comprise of a core, which is capped by a ligand that prevents the QD from growing in size and exceeding the dimensions at which they show their unique properties. QDs have dimensions and numbers of atoms between the atomic and bulk material level. For isolated atoms, sharp and narrow luminescent emission peaks are observed. However, a nanoparticle, composed of thousands of atoms exhibits distinct narrow optical line spectra. [87] These unique optical properties of the QDs are dependant predominantly on their size and morphology. This size dependence is brought about by changes in the surface to volume ratio and quantum confinement effects.

Consequently, QDs (and for that matter all QNCs) show varied color of emission upon change in size.

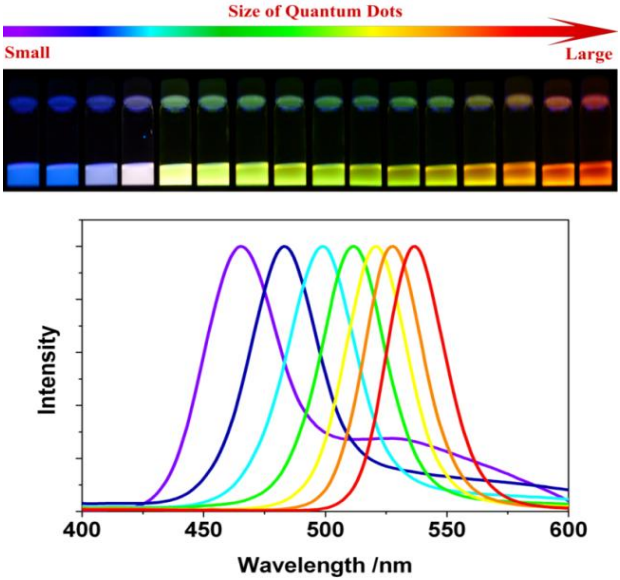

Figure 15. Top: Sixteen emission colors from small (blue) to large (red) CdSe QDs excited by a near-ultraviolet lamp; size of QDs can be from ~1 nm to ~10 nm. Bottom: Photoluminescence spectra of some of the CdSe QDs. [88]

1.1.2.4.1 Quantum Confinement

Quantum confinement is a unique property shown by all QNCs. Quantum confinement effects are observed when the size of a particles is so small that the energy level spacing of a nanocrystal exceeds kT (where k is *Boltzmann's* constant and T is temperature). When the energy differences are greater than kT, the mobility of the electron and holes in a crystal becomes restricted. This

leads to a blue shift (increase) in band gap energy when the particles are below a particular size, the size being different for each semiconductor material. The Quantum confinement effect allows for size dependant tuning of band gap. [89-90]

Quantum confinement usually leads to a widening of the band gap with a decrease in the size of the QDs. The band gap in a material is the energy required to create an electron and a hole at rest (*i.e.,* with zero kinetic energy) at a distance far enough apart that their coulomb attraction force is negligible. The distance between the electron and hole is called the Bohr Exciton radius (r_B) and for a bulk semiconductor, it can be expressed as:

$$r_B = \frac{\hbar^2 \varepsilon}{e^2}\left\{\frac{1}{m_e} + \frac{1}{m_h}\right\}$$

where ε: Optical dielectric constant

ħ: Reduced Planck's constant

e: Electron charge

m_e: Effective mass of electron

m_h: Effective mass of hole

If the radius (R) of a QD approaches r_B, i.e., $R \approx r_B$, or $R < r_B$, then the motion of the electrons and holes become confined spatially to the dimensions of the QD which results in an increase of the excitonic transition energy. This leads to the observed blue shift in the QD band gap and consequently, luminescence. The Bohr exciton radius

is a threshold value, and the confinement effect becomes important when the QD radius is smaller. [91]

1.1.2.4.2 Luminescence Properties

Upon excitation by an external energy source, the electron and hole in a QD, possess high energies due to transition of electron from its ground state to an excited state. This excited electron may form an electron-hole pair, called an exciton. The electron may recombine with the hole and relax to a lower energy state, ultimately reaching its ground state. This process of recombination and relaxation results in a release of excess energy which may be either radiative, thus emitting photons or nonradiative, thus emitting phonons. Upon being excited with UV light, most QNCs show the property of photoluminescence.

The spectral range of photoluminescence depends on the band edge emissions as well as defects in the QDs (or QNCs). The recombination of an excited electron in the conduction band with a hole in the valence band is called band edge emission. Radiative recombination of an exciton leads to near band edge emission at energies slightly lower than the band gap. There have also been studies that demonstrate that surface states of QDs are involved in photoluminescent emission. [92]

Defects in the band gaps also lead to radiative emission for QDs. [93] Defect states are expected at the surface of a QD because of their large surface-to-volume ratio. These surface states act as traps for charge carriers and excitons which increases the rate of nonradiative recombination, thus leading to a degradation of optical and electrical

properties. However, in some cases, the surface states can also lead to radiative transition.

1.1.2.4.3 Quantum Yield

The Fluorescent Quantum Yield may be defined as the ratio of the number of photons emitted to the number of photons absorbed. [94] There are several approaches to measuring the Quantum Yield (QY) of QNCs. In addition, obtaining an accurate QY can be complicated due to inappropriate concentrations or optical density of the samples, change of slits between samples and standards during the measurements and instrumentation error. In general, QY is determined by comparing the integrated emission intensity from the QDs to that from standards. The optical densities of the QDs and the standard(s) are determined using a fluorimeter.

A thorough examination of all the approaches used to calculate QY was done by Grabolle et al in 2009 and following the recommendations made in that paper, for measuring the QY in this thesis, relative fluorescence QY of a QD at different excitation wavelengths was measured. [95] Because of the typically narrow absorption bands of common QY standards this approach requires the use of different standards with reliably known fluorescence QYs for the different excitation wavelengths. The following formula was used for performing the calculations:

$$\mathbf{QY = QY_{ref}\{\eta^2 I A_{ref} (\eta_{ref} I_{ref} A)^{-1}\}}$$

Where QY_{ref} : Quantum Yield of the reference
η- Refractive index of the solvent
η_{ref}- Refractive index of the solvent of the standard

I- Integrated area of emission spectrum of sample
I_{ref} – Integrated area of emission spectrum of reference
A- Absorbance value of sample
A_{ref}- Absorbance value of the reference

1.1.2.4.4 Core-Shell concept of Quantum Nanocrystals

II-VI type semiconductors include the cations of zinc, cadmium and/or mercury combined with anionic oxygen, sulphur, selenium and/or tellurium. They compose the core of the QNC. This core is usually capped with a ligand shell to prevent excessive growth of the core material. This ligand can be either organic or inorganic. Monodispersed QDs are developed by introducing organic molecules that adsorb on the surface and act as capping agents. [96-98] Some advantages of organic capping layers include simultaneous achievements of colloidal suspension and the ability to bio-conjugate the QDs. However, most of the organic capping molecules are distorted in shape and larger than a surface site. Consequently, the coverage of surface atoms with the organic capping molecules is sterically hindered. Another issue with organic capping ligands is the simultaneous passivation of both anionic and cationic surface sites using such capping agents, which is not easy to achieve. Some dangling bonds on the surface are always present when the surface is passivated by organic agents. The QDs capped with organic ligands are photo-unstable. The bonding at the interface of the capping molecules and core surface atoms is generally weak leading to creation of new surface states under UV

irradiation. Some of the popular organic capping ligands are tri-n-octyl phosphine oxide–TOPO or mercapto (-SH) compounds like Mercaptoacetic acid.

To potentially overcome this issue of using organic ligands, the decision to use inorganic carboranyl ligands as capping agents was made, as shown in Section 3.4 of the Results and Discussion. They have a structure that because of its rigidness reminds of aromatic compounds, but they are spheres, not flat surfaces, although both are aromatic and thus highly stable. [8] They show all the advantages of organic moieties as capping agents, but since they are inorganic in nature, they do not suffer from the same disadvantages as organic capping agents.

1.1.2.5 Gold Nanoparticles

Gold nanoparticles (Au NPs) are amongst the most studied nanoparticles and have generated great interest. [99] They display high X-ray absorption coefficient, can be easily manipulated synthetically, enable precise control over a particle's physicochemical properties [100], show a strong binding affinity to thiols, disulfides and amines [101], and possess unique tunable optical and distinct electronic properties. [102]

1.1.2.5.1 Properties of Gold Nanoparticles

Au NPs have found use in many applications in various disciplines, due to their unique properties. The foremost amongst these properties that are most important for their use in a large variety of applications are shape related optoelectronic properties, large surface to volume ratio, remarkable biocompatibility and low toxicity. [103] It has

been well established that the Surface Plasmon Resonance (SPR) and physical properties of Au NPs are dependant on their morphology. [104-106] Hence, the size of the Au NPs is extremely important for applications where their optical properties are involved, such as their use as therapeutic agents, as the optical properties of the NPs change with size of the particles.

1.1.2.5.2 Applications of Gold Nanoparticles

As mentioned above, Au NPs have found applications in a variety of fields. Some of the major applications are briefly discussed below:

i. Photothermal Therapy- It is an applied method of cancer therapy with minimum invasion. [108-110] Au NPs with maximum absorption in the visible or near Infra-red region, receive light and generate heat which causes the death of malignant tumors. [109] Spherical Au NPs having a diameter greater than 50 nm are most commonly used in this method, the larger size of the Au NPs allows for stronger Near Infra-Red absorption.[107]

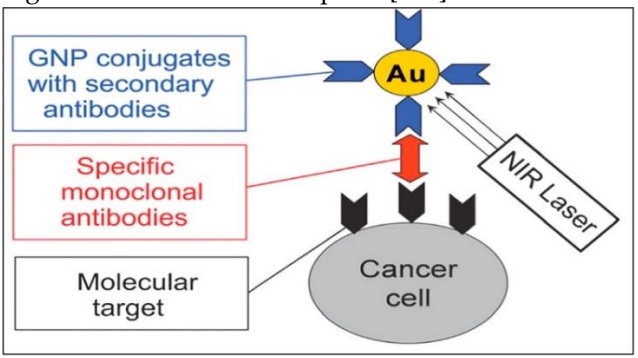

Figure 16. Scheme for a Photothermal Therapy employing active delivery of AuNPs to cancer cells. [110]

ii. Phtotodynamic Therapy- This technique involves using Au NPs as photosensitizers and light sensitizing agents. They are used in conjunction with a laser for the treatment of certain oncological and skin diseases. Effective fluorescence quenching and surface plasmon resonance (SPR) absorption are the properties of AuNPs that allow for their use in photodynamic therapy. Besides, gold complexed with conjugates facilitates intracellular penetration, due to its tendency to bind with thiols, disulfides, and amines. [110]

iii. Drug Delivery- The physical and biological properties of Au NPs make them ideal for use as nanocarriers in drug delivery systems. [111-113] They are capable of transferring various drugs such as proteins [114], plasmid DNAs, peptides [115] and chemotherapeutic agents. [116]

iv. Sensing- Perhaps the most important use of Au NPs has been as nano-biosensors. Au NPs have been used for sensing applications for a large number of analytes and molecules as depicted by the schematic below.

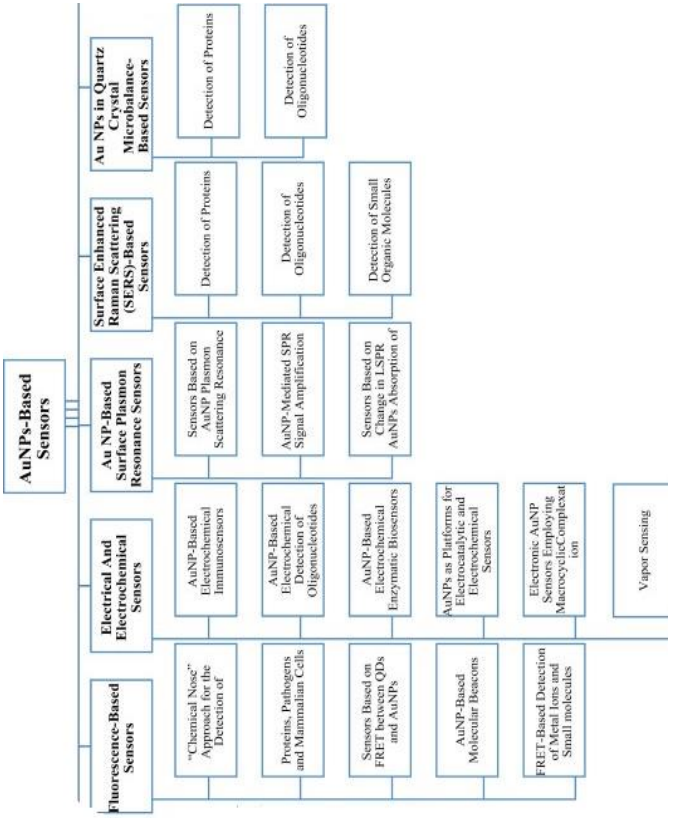

Figure 17. Summary of different types of gold nanoparticles biosensors. [103]

1.1.2.5.3 Synthesis of Gold Nanoparticles

The synthesis techniques for Au NPs can be divided into 3 broad categories:

i. Physical Methods- These methods include Microwave Irradiation, UV Radiation, Gamma Irradiation, Laser Ablation and Sonochemical method. [106] The physical methods allow for control over size by

optimizing the synthesis conditions. [117] The laser ablation method can be used to produce Au NPs with tuneable features.

ii. Biological Methods- Plant based compounds and derivatives as well as bacteria, fungi, algae, yeast, virus are used as common sources for Au NPs synthesis. Using of these biological media allow for an environmental-friendly synthesis procedure. Depending upon the type of biological source used for the synthesis, the size and shape of the Au NPs can be controlled. [112, 118-120]

iii. Chemical Methods- The Turkevich procedure is the most widely used procedure for the synthesis of colloidal Au NPs, owing to its ease of synthesis as well as control over the size and stability of the Au NPs. In this method Chloroauric Acid is reduced with a sodium citrate solution, leading to monodispersed spherical Au NPs. [121-122] In 1994, the Brust–Schiffrin method was reported which utilized potent thiol–gold interactions to protect AuNPs with thiol ligands. It involves the reaction of a chlorauric acid solution with tetraoctylammonium bromide (TOAB) solution in toluene and sodium borohydride. Here, $NaBH_4$ is the reducing agent, and TOAB is both the phase transfer catalyst and the stabilizing agent. This method led to synthesis of Au NPs of size 1-3 nm in diameter. [123]

Though highly stable, the Au NPs produced by these methods showed only a single-phase solubility, limiting their potential for use in biomedical applications. The pioneering work of Vinas and Co. by using *ortho*-carboranethiol as capping agent for Au NPs led to NPs which exhibit redox-dependent solubility and readily

phase transfer between water and nonpolar solvents depending on the electronic and ionic charge stored in the metal core and in the ligand shell, respectively. [124] This work opened the doors for further research in the fascinating phase transfer properties of the ortho-carboranethiol capped Au NPs, which has been explored in Section 3. 5 of the Results and Discussion section.

1.2 References

1. R. Hoffmann, W. N. Lipscomb, *J. Chem. Phys.*, **36** (1962) 3489.
2. Z. F. Chen, R. B. King, *Chem. Rev.*, **105** (2005) 3613.
3. H. C. Brown, *Science*, **210** (1980) 485.
4. H. I. Schlesinger, H. C. Brown, H. R. Hoekstra, L. R. Rapp, *J. Am. Chem. Soc.*, **75** (1953) 199.
5. H. C. Brown, H. I. Schlesinger, A. B. J. Burg, *J. Am. Chem. Soc.*, **61** (1939) 673.
6. K. P. C. Vollhardt, *Organic Chemistry, W. H. Freeman and Co.*, New York, 1987.
7. J. Poater, M. Sola, C. Vinas, F. Teixidor, *Chem- A Eur. J.*, 22 (2016) 7437.
8. J. Poater, M. Sola, C. Vinas, F. Teixidor, *Angew. Chemie.- Int. Ed.*, **53** (2014) 12191-12195.
9. J. Poater, M. Sola, C. Vinas, F. Teixidor, *Chem- A Eur. J.*, **19** (2013) 4169.
10. R. N. Grimes, *Carboranes, Elsevier*, Oxford, 3rd Ed., 2016.
11. M. F. Hawthorne, D. C. Young, P. A. Wegner, *J. Am. Chem. Soc.*, **87** (1965) 1818.
12. C. Masalles, J. Llop, C. Viñas, F. Teixidor, *Adv. Mater.*, **14** (2002) 826.
13. I. Bennour, A.M. Cioran, F. Teixidor, C.Vinas, *Green Chemistry*, **21** (2019) 1925-1928.
14. C.A. Reed, *Acc. Chem. Res.* **31** (1998) 133–139.
15. S.H. Strauss, *Chem. Rev.* **93** (1993) 927–942.
16. I.B. Sivaev, V.I. Bregadze, *Collect. Czechoslov. Chem. Commun.* **64** (1999) 783–805.
17. J. Plesek, K. Base, F. Mares, F. Hanousek, S. Hermanek, *Collect. Czech. Chem. Commun.* **49** (1983) 2776–2789.
18. O.A. Biloivan, S.V. Dzyadevych, A.V. El'skaya, N. J. Renault, N. Zine, J. Bausells, J. Samitier, A, Errachid, *Sens. Actuators B* **123** (2007) 1096–1100.
19. O.A. Biloivan, S. V. Verevka, S.V. Dzyadevych, N. J. Renault, N. Zine, J. Bausells, J. Samitier, A, Errachid, *Mater. Sci. Eng. C.* **26** (2006) 574–577.
20. I.A. Marques de Oliveira, M.P. Roca, L. Escriche, J. Casabo, N.Zine, J. Bausells, F. Teixidor, E. Crespo, A. Errachid, J. Samitier, *Electrochim. Acta.* **51** (2006) 5070–5074.

21. I.A. Marques de Oliveira, D. Risco, F. Vocanson, E. Crespo, F. Teixidor, N. Zine, J. Bausells, J. Samitier, A. Errachid, *Sens. Actuators B* **130** (2008) 295–299.
22. N. Zine, J. Bausells, F. Vocanson, R. Lamartine, Z. Asfari, F. Teixidor, E. Crespo, I. A. Marques de Oliveira, J. Samitier, A. Errachid, *Electrochim. Acta.* **51** (2006) 5075–5079.
23. N. Zine, J. Bausells, A. Ivorra, J. Aguilo, M. Zabala, F. Teixidor, C. Masalles, C. Vinas, A. Errachid, *Sens. Actuators B,* **91** (2003) 76–82.
24. Y. Marcus, A. K.SenGupta, J.A. Marinsky, Ion Exchange and Solvent Extraction: A Series of Advances, Volume 17, 2005.
25. R. Nunez, I. Romero, F. Teixidor, C. Vinas, Chem Soc. Rev., **45** (2016) 5147-5173.
26. R. Nunez, M. Tarres, A. F. Ugalde, F. F di Biani, F. Teixidor, Chem Rev., 116 (2016) 14307-14378.
27. A. J. Bard and L. Faulkner (2000). Electrochemical Methods: Fundamentals and Applications. Wiley
28. L.A.R. Pioda, V. Stankova, W. Simon, Anal. Lett. **2** (1969) 665–674.
29. D. Ammann et al., Ion-Selective Electrode Rev., Elsevier, 1983: 3–92.
30. C. Moore, B.C. Pressman, *Biochem. Biophys. Res. Commun.,* **15** (1964) 562–567.
31. A. Shatkay, *Anal. Chem.,* **39** (1967) 1057.
32. J.W. Ross, *Science,* **156** (1967) 1378–1379.
33. PhD thesis, Juan Gallardo-Gonzalez, 2018.
34. G. Dimeski, T. Badrick, A.S. John, *Anal. Lett*., **411** (2010) 309–317.
35. E. Bakker, P. Bühlmann, E. Pretsch, *Chem. Rev*., **97** (1997) 3083–3132.
36. Y. Umezawa, CRC handbook of ion-selective electrodes: Selectivity coefficients., 1990.
37. E. Bakker, E. Pretsch, P. Bühlmann, *Anal. Chem*. **72** (2000) 1127–1133.
38. F. Deyhimi, *Talanta*., **50** (1999) 1129–1134.
39. K.N. Mikhelson, Lecture Notes in Chemistry 81. Ion-Selective Electrodes, 2013.
40. C.J. Coetzee, H. Freiser, *Anal. Chem.,* **40** (1968) 2071.
41. P. Bühlmann, E. Pretsch, E. Bakker, *Chem. Rev*. **98** (1998) 1593–1688.

42. H. Freiser, Ion-selective electrodes in analytical chemistry, Springer Science & Business Media, 2012.
43. V. V. Egorov, P. L. Lyaskovski, I. V. Il'inchik, S. V. Vera, V. A. Nazarov, *Electroanalysis.* **21** 2061–2070.
44. M.A. Peshkova, A.I. Korobeynikov, K.N. Mikhelson, *Electrochim. Acta.,* **53** (2008) 5819–5826.
45. M. N. Konstantin, *Electroanalysis.,* **15** (2003) 1236–1243.
46. K. Vitras, J. Kalous, *Anal. Chim. Acta,* **177** (1985) 219–223.
47. R. Matesic-Puac, M. Sak-Bosnar, M. Bilic, B.S. Grabaric, Sens. Actuators B., **106** (2005) 221–228.
48. H.M. Abu Shawish, S.M. Saadeh, A.R. Al-Dalou, N.A. Ghalwa, A.A.A. Assi, *Mater. Sci. Eng. C.,* **31** (2011) 300–306.
49. P.G. Boswell, P. Bühlmann, *J. Am. Chem. Soc.* **127** (2005) 8958–8959.
50. M. Shamsipur, F. Jalali, S. Ershad, *J. Pharm. Biomed. Anal.*, **37** (2005) 943–947.
51. J.A. Ortuño, V. Ródenas, M.S. Garcia, M.I. Albero, C. Sánchez-Pedreño, *Sensors.* **7** (2007) 400–409.
52. A.I. Stoica, C. Vinas, F. Teixidor, *Chem. Commun*. (2008) 6492–6494.
53. A.-I. Stoica, C. Vinas, F. Teixidor, *Chem. Commun*. (2009) 4988–4990.
54. J. G. González et al., *Proc. Eurosensors Conf. Paris 2017*. **1** (2017) 2–5.
55. C. Masalles, S. Borros, C.Vinas, F. Teixidor, *Adv. Mater.,* **12** (2000) 1199–1202.
56. N. Zine, et al., *Mater. Sci. Eng. C.* **26** (2006) 399–404.
57. E. Malinowska, L. Gawart, P. Parzuchowski, G. Rokicki, Z. Brzózka, *Anal. Chim. Acta*., **421** (2000) 93–101.
58. G.J. Moody, B. Saad, J.D.R. Thomas, Analyst. 112 (1987) 1143–1147.
59. M.W. E., S. W, *Helv. Chim. Acta*. **54** (2018) 2683–2704.
60. M. De los A. Arada Pérez, L. Marín Pérez, J. Calvo Quintana, M. Yazdani-Pedram, *Sens. Actuators B*, **89** (2003) 262–268.
61. PhD thesis, Elena Oleshkevich, 2017.
62. F. A. Gomez, M. F. Hawthorne, *J. Org. Chem.* **57** (1992) 1384–1390.
63. C. Vinas, R. Benakki, F. Teixidor, J. Casabo, *Inorg. Chem.* **34** (1995) 3844–3845.
64. J. F. Valliant et al., *Coord. Chem. Rev*. **232** (2002) 173–230.

65. A. R. Popescu, *Chem. - A Eur. J.* **18** (2012) 3174–3184.
66. F. Teixidor, M. A. Flores, C. Viñas, R. Kivekäs, R. Sillanpää, *Angew. Chemie Int. Ed.,* **35** (1996) 2251–2253.
67. F. Teixidor, M. A. Flores, C. Viñas, R. Kivekäs, R. Sillanpää, *Angew. Chemie,* **108** (1996) 2388–2391.
68. F. Teixidor, M. A. Flores, C. Viñas, R. Kivekäs; R. Sillanpää, *Organometallics*. **17** (1998) 2278-2289
69. C.Viñas; R. Núñez, F. Teixidor, R. Kivekäs, R.Sillanpää, *Organometallics.* **17** (1998) 2376-2378.
70. F. Teixidor, S. Gomez, M. Lamrani, C. Vinas, R. Sillanpää, R. Kivekas, *Organometallics*, **16** (1997) 1278-1283.
71. C. Viñas, R. Nuñez, F. Teixidor, R. Kivekäs, R. Sillanpää, *Organometallics.* **15** (1996) 3850-3858
72. F. Teixidor, M. A. Flores, C. Vinas, R. Sillanpää, R. Kivekäs, *J. Am. Chem. Soc.* **122** (2000) 1963–1973.
73. A. Demonceau, et al., *Tetrahedron Lett.* **38** (1997) 4079–4082.
74. A. Demonceau, F. Simal, A. F. Noels, *Tetrahedron Lett.,* **38** (1997) 7879–7882.
75. S. Delfosse, Advances in Controlled/Living Radical Polymerization, 2003, 116–129.
76. O. Tutusaus, S. Delfosse, F. Simal, A. Demonceau, A. F. Noels, R. Nunez, C. Vinas, F. Teixidor, *Inorg. Chem. Comm*. **5** (2002) 941–945.
77. O. Tutusaus, S. Delfosse, A. Demonceau, A. F. Noels, R. Nunez, C. Vinas, F. Teixidor, *Tetrahedron Lett.* **43** (2002) 983-987.
78. O. Tutusaus, C. Vinas, R. Nunez, F. Teixidor, A. Demonceau, S. Delfosse, A. F. Noels, I. Mata, E Molins, *J. Am. Chem. Soc.*, **125** (2003) 11830–11831.
79. O. Tutusaus, S. Delfosse, A. Demonceau, A.F. Noels, C. Vinas, F. Teixidor, *Tetrahedron Lett.,* **44 (**2003) 8421-8425.
80. (a) G. Barbera, C. Vinas, F. Teixidor, G.M. Rosair, A.J. Welch, *J. Chem. Soc., Dalton Trans.*, (2002) 3647-3648; (b) R. Nunez, P. Farras, F. Teixidor, C. Vinas, R. Sillanpaa, R. Kivekas, *Angew Chem. Int. Ed*., **45** (2006) 1270-1272.
81. E. Oleshkevich, F. Teixidor, A. Rosell, C. Vinas, *Inorg. Chem*., **57** (2018) 462-470.
82. E. Oleshkevich, F. Teixidor, D.C. Lazarte, R. Sillanpaa, C. Vinas, Chem. Eur. J, **22** (2016) 3665-3670.
83. A. Henglein, *Chem. Rev.* **89** (1989) 1861–1873.

84. T. Trindade, P. O'Brien, N. L. Pickett, *Chem. Mater.* **13** (2001) 3843–3858.
85. S. Kuchibhatla, A.S. Karakoti, D. Bera, S. Seal, *Prog. Mater. Sci.* **52** (2007) 699–913.
86. D. Bera, S.C Kuiry, S. Seal, S. *JOM* **56** (2004) 49–53.
87. D. Bera, L. Qian, T. K. Tseng, P. H. Holloway, *Materials* **3** (2010) 2260-2345.
88. D. Bera, L. Qian, P. H. Holloway, InformaHeathcare: New York, NY, USA, 2009; Vol. 191.
89. A. D. Yoffe, *Adv. Phys.* **42** (1993) 173–266.
90. A. D. Yoffe, *Adv. Phys.* **50** (2001) 1–208.
91. V. I. Klimov, *J. Phys. Chem. B,* **110** (2006) 16827–16845.
92. M. G. Bawendi, et al., *Phys. Rev. Lett.* **65** (1990) 1623–1626.
93. A. Issac, C. von Borczyskowski, F. Cichos, *Phys. Rev. B.* **71** (2005) 161302.
94. R. J. Lakowicz, Principles of Photoluminescent Spectroscopy, Plenum Publishers, 1999.
95. M. Grabolle, M. Spieles, V. Lesnyak, N. Gaponik, A. Eychmuller , U. Resch-Genger, *Anal. Chem.* **81** (2009) 6285-6294.
96. E. Kucur, W. Bucking, R. Giernoth, T. Nann, *J. Phys. Chem. B*, **109** (2005) 20355–20360.
97. V. L. Colvin, A. N.Goldstein, A. P. Alivisatos, *J. Am. Chem. Soc.* **114** (1992) 5221–5230.
98. B. O. Dabbousi, C. B.Murray, M. F. Rubner, M. G. Bawendi, *Chem. Mater.* **6** (1994) 216–219.
99. Z. Zhang, et al., *J. Am. Chem. Soc.*, **136** (2014) 7317-7326.
100. Y. Zhang, et al., *Materials (Basel).*, **7** (2014) 5169-5201.
101. Y. Zhou, C.Y. Wang, Y.R. Zhu, Z.Y. Chen, *Chem. Mat.,* **11** (1999) 2310-2312.
102. Y. Zhang, J. Qian, D. Wang, Y. Wang, S. He, *Angew. Chem. Int. Ed*., **52** (2013), 1148-1151.
103. N. Elahi, M. Kamali, M. H. Baghersad, *Talanta*, **184** (2018) 537-556.
104. Y.-C. Yeh, B. Creran, V.M. Rotello, *Nanoscale*, **4** (2012) 1871-1880.
105. X. Ye, et al., *Nano Lett.*, **13** (2013) 2163-2171.
106. Z. Zhang, et al., *Nano-Micro Lett*., **9** (2017) 5.
107. P. Mishra et al., *Biochem. Eng. J*., **105** (2016) 264-272.

108. V.S. Marangoni, J. Cancino-Bernardi, V. Zucolotto, *J. Biomed. Nanotechnol.*, **12** (2016) 1136-1158.
109. H.M. Manjunath, C.G. Joshi, N.G. Raju, *IET Nanobiotechnol*., **11** (2016) 40-44.
110. J. Narang, N. Malhotra, G. Singh, C.S. Pundir, *Biosens. Bioelectron*., **66** (2015) 332-337.
111. X. Xu, X. Liu, Y. Li, Y. Ying, *Biosens. Bioelectron*., **47** (2013) 361-367.
112. J. Wang, et al., *ACS Nano*, **6** (2012) 5070-5077.
113. P. Luo, Y. Liu, Y. Xia, H. Xu, G. Xie, *Biosens. Bioelectron*., **54** (2014) 217-221.
114. A. J. Love, et al., *Front. Plant Sci*., **6** (2015).
115. X. Lu, et al., *Analyst*, **138** (2013) 642-650.
116. J. Liu, et al., *Small*, **11** (2015) 2323-2332.
117. S. Wang, X. Zhao, S. Wang, J. Qian, S. He, *ACS Appl. Mater. Interfaces*, **8** (2016) 24368-24384.
118. L. Vigderman, B.P. Khanal, E.R. Zubarev, *Adv. Mater*., **24** (2012) 4811-4841.
119. R. Venkatesan, et al., *J. Mater. Chem. B*, **1** (2013) 1010-1018.
120. A.K. Vala, Environ. *Prog. Sustain. Energy*, **34** (2015) 194-197.
121. J. Turkevich, P.C. Stevenson, J. Hillier, *Discuss. Faraday. Soc*., **11** (1951) 55-75.
122. J. Kimling, et al., *J. Phy. Chem. B*, **110** (2006) 15700-15707.
123. M. Brust, M. Walker, D. Bethell, D. J. Schiffrin, *J. Chem. Soc. Chem. Commun*. 7 (1994) 801–802.
124. A.M. Cioran, A.D. Musteti, F. Teixidor, Z, Krpetic, I.A. Prior, Q. He, C.J. Kiely, M. Brust, C. Vinas, *J. Am. Chem. Soc*. 134 (2012) 212-221.

2. Objectives

Abhishek Saini
ICMAB-CSIC (UAB)

2. Objectives of the Thesis

The objectives of this thesis were as follows:

- To study the use of $[Co(C_2B_9H_{11})_2]^-$ anion as an electroactive component of PVC based micro-Ion Selective Electrodes, incorporating an ion pair complex made up of the $[Co(C_2B_9H_{11})_2]^-$ anion and the target anion, an antibiotic with a protonable amine group.
- Potentiometric detection of antibiotics such as Irgarol, Sulphonamide and Amphetamine using the aforementioned micro-ISE. The selectivity, sensitivity, lifetime, response time and pH response of these micro-ISEs were to be studied to see how the incorporation of the $[Co(C_2B_9H_{11})_2]^-$ anion affected all these response parameters.
- To use carboranyl derivatives as capping agents for the formation of Quantum Nanocrystals (QNCs). The unique spherical structure of these carboranyl ligands as well as the presence of an appended coordinating site acted as the motivation to use them as capping agents to modify the shape of CdSe nanostructures. The reason for this being that spheres can ideally pack in a compact way with a hexagonal or square arrangement, thus influencing the inner core by the outer sphere packing. The linkage between the spheres and the CdSe core is through a coordinating site with a negative charge, $–S^-$, $–PH(O)O^-$. As we intended to facilitate dissolution in high boiling low polar solvents, we decided to use the neutral carboranes, owing to their lipophilicity.
- To study the unique phase transfer property of *ortho*-carboranethiol capped gold nps (Au NPs) by using

the previously untested di, tri and tetravalent ions such as Fe^{3+}, Ce^{4+}, Ni^{2+} etc. We wanted to test whether the *ortho*-carboranethiol capped Au NPs facilitated the transfer of these ions across different phases, thus opening avenues for their further use in biomedical applications.

- To study the capping of Gold coated magnetic nanoparticles (MNP@Au) with $H[[Co(C_2B_9H_{11})_2]$ (H[COSAN] which would allow the use of this complex to be used as a sensing layer in point of care devices for diagnostic purposes owing to redox tuneable properties of H[COSAN].

3. Results and Discussions Part 1 (Cobaltabis(dicarbollide) based Highly Selective Potentiometric micro-ISEs)

3.1. Potentiometric Ion-Selective Electrode For Irgarol Detection

The $[Irgarol\text{-}H]^+[Co(C_2B_9H_{11})_2]^-$ ion pair complex was used to prepare a PVC matrix based all solid state Irgarol selective microelectrode. This novel Ion Selective electrode gives low limit of detection and high selectivity for the detection of the algaecide Irgarol in water.

Abhishek Saini
ICMAB-CSIC (UAB)

CONTENTS

3.1.1 Introduction

Most paints have been known to contain algaecides as antifouling agents but these algaecides are notorious and highly damaging to marine life. These algaecides have been known to find their way into sea water and highly destructive towards the algae in sea water.[1] One of the most widely used anti fouling agent in paints is Irgarol (2-[tert-butylamino]-4-[cyclopropylamino]-6-[methylthio]-1,3,5-triazine]. It has been reported to be extremely harmful towards algal organisms. [2] Irgarol belongs to the s-triazine group of compounds, which act as photosystem- II (PSII) inhibitors, with the inhibition of photosynthetic electron capture transport in chloroplasts as their biochemical mode of action.[1] Irgarol contamination has been detected as far back as 1993 from the Cote d'azur to more recently in the southern coast of UK and in the Seto island sea in Japan.[2]-[7].

Over the years many methods have been used for its detection such as Nitrogen-Phosphorous Detector (GC-NPD) and Gas Chromatography-Mass Spectroscopy in Selected Ion Monitoring Mode (GC-MS SIM). Irgarol was detected in Japan using GC-MS and Electrospray Ionization Mass Spectroscopy with Tandem Mass Spectroscopy (ESI-MS/MS).[2][6][7] The disadvantage of these methods is that they require expensive equipment and long time for sample preparation.

Other techniques such as Immunosensors [8] for trace detection and competitive ELISA [9] have also been developed for the detection of Irgarol. But they face their own set of problems. The antibodies are usually inactive

in high concentrations of organic media and their use makes sample preparation a complex task as antibodies can only be used a finite number of times. [10] On the other hand, immunosensors require extraction procedures such as chromatographic methods.[9]

Therefore, there is an obvious need for development of cheaper and faster methods for the detection of antifouling agents like Irgarol in water. This acted as the motivation of this work and to this end we propose a potentiometric microsensor. A class of potentiometric sensor named Ion Selective Electrodes were used in a first of its kind in available literature for the detection of Irgarol in water. The proposed microsensor is miniature, simple to use and inexpensive to prepare. It also doesn't make use of any complicated pre concentration or extraction techniques. As explained in the introductory chapter, an Ion Selective Electrode's primary component is an Ionophore and in our case we used an Ion Pair complex made of the $[C_{11}H_{20}N_5S]^+[Co(C_2B_9H_{11})_2]^-$ ion pair complex.

3.1.1.1. Ion Selective Electrodes

Ion Selective Electrodes (ISEs) are a class of potentiometric sensors which are well established in literature as being cheap, simple and rapid method for electroanalytical detection of analytes. The use of ISEs does away with many of the problems faced while using chromatographic techniques as well as Immunosensors or competitive ELISA as detection methods for analytes. Contrary to the

aforementioned methods, ISEs do not require expensive equipment or complicated extraction techniques. They also don't need a long sample preparation time. The last few decades have seen a massive increase in use of ISEs based on Polyvinyl Chloride (PVC) polymeric membrane. [11]-[13] This has led to a remarkable enhancement in the performance of the ISEs in terms of their most important response parameters, namely, the limit of detection and selectivity. A conventional ISE typically consists of a polymer matrix (usually PVC), a plasticizer, ion complexing agent called ionophore and lipophilic ionic additives. [14]-[15]

The introduction of the$[Co(C_2B_9H_{11})_2]^-$ anion as an electroactive ion-generator in ISEs was a major breakthrough as it was demonstrated that ISEs based on solid membranes having ion-pair complexes [cation-NH]$^{n+}$ n$[Co(C_2B_9H_{11})_2]^-$ can be incorporated in PVC membranes and are suitable for determination of bioactive nitrogen containing compounds [cation-NH]$^{n+}$. [16]

3.1.1.2 Importance of Cobaltabisdicarbollide $[Co(C_2B_9H_{11})_2]^-$ anion

The $[Co(C_2B_9H_{11})_2]^-$ anion is a metallacarborane, which belongs to the boron cluster type of compunnds. These are deltahedra with most of their vertices being Boron atoms. It is well established that the carborane $[CB_{11}H_{12}]^-$ gives better performance when used as a lipophilic anion additive for ISE membranes when compared to

tetraphenylborate, which is commonly used for this purpose. [17]-[20] Closo-boranes are lipohilic, have a bulky structure and possess sufficient charge delocalization to produce weak ion pairs. [21]

For Ion sensing microsensors, the lifetime of sensors is increasingly dependant upon membrane residence time of the active sensing components [22] and upon using traditional ion exchangers, with time, the loss of these ion exchangers leads to decrease in selectivity. The advantage of using $[Co(C_2B_9H_{11})_2]^-$ anion as the electroactive component in an ion pair complex is that its lipophilic, it's a weakly coordinating anion, has lower charge density than other boranes and carboranes and it can self assemble through the formation of $C_{cluster}$-H···H-B dihydrogen bonds. [23]-[25] It can be non-covalently bonded to the plasticizer through $C_{cluster}$-H···O hydrogen bond and produce weak B-H···H-N dihydrogen bonds with the electro-active cations leading to improved stability of the membrane. [26]

The ability of the $[Co(C_2B_9H_{11})_2]^-$ anion to produce self assembled layers were used to produce simple ISEs in which the aforementioned anion is the ion-pair generator and it could produce complexes with antibiotics that could be protonated to produce HN bonds intended for B–H···H–N dihydrogen bonds. The protonated form of an antibiotic and the $[Co(C_2B_9H_{11})_2]^-$ anion can be combined to form an ion pair complex which when incorporated in a PVC matrix can be used to form an Ion Selective Electrode.

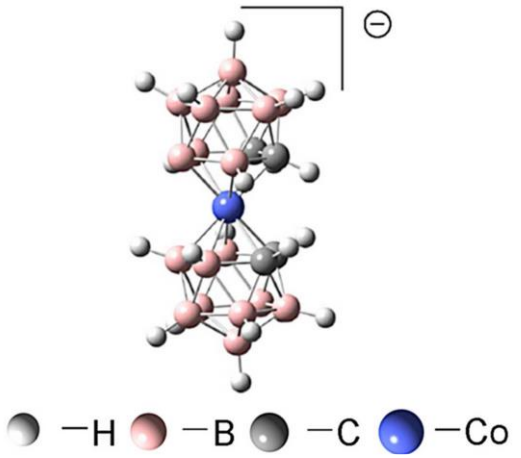

Figure 1. Chemical structure of Cobalt bis(dicarbollide) anion

3.1.2 Microelectrode Preparation and Ion Pair complex synthesis

3.1.2.1 Ion Pair Complex Synthesis

The synthesis of the$[C_{11}H_{20}N_5S][Co(C_2B_9H_{11})_2]$ complex (**Fig. 2**) was carried out by extracting $Cs[Co(C_2B_9H_{11})_2]$ (300 mg, 0.657 mmol) with HCl 1 M (15 mL) and diethyl ether (20 mL). The organic layer was shaken three times with HCl 1 M (15 mL 3x). Then, the organic layer was evaporated and the residue was diluted with water to generate 0.05 M solution of $H[Co(C_2B_9H_{11})_2]$ (solution 1). Irgarol was dissolved in water and with the minimum quantity of HCl to prepare 0.05 M acidic solution (solution 2). Then 15 mL of both Solution 1 and solution 2 were mixed under stirring until a yellow precipitate was

obtained. This was filtered, washed with HCl 0.1 M and dried under vacuum.

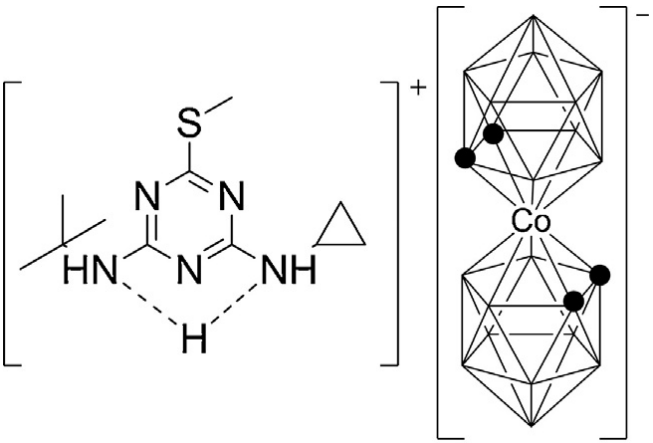

Figure 2. Chemical structure of the $[C_{11}H_{20}N_5S][Co(C_2B_9H_{11})_2]$ ion pair complex

The chemical composition of the generated ion pair complex was studied by Nuclear Magnetic Resonance (NMR) (^1H, $^1H\{^{11}B\}$, ^{11}B,$^{11}B\{^1H\}$ $^{13}C\{^1H\}$), Fourier Transform Infrared Spectroscopy (FTIR), Elemental Analysis (EA) and MALDI-TOF-MS spectroscopies.

IR spectra were obtained on PerkinElmer® Universal ATR Accessory spectrophotometer. The ^1H- and $^1H\{^{11}B\}$-NMR (300.13 MHz), $^{13}C\{^1H\}$-NMR (75.47 MHz) and ^{11}B- and $^{11}B\{^1H\}$-NMR (96.29 MHz) spectra were recorded on a Bruker ARX 300 instrument equipped with the appropriate decoupling accessories. All NMR spectra were performed in acetone deuterated solvent at 22°C. The ^{11}B- and $^{11}B\{^1H\}$-NMR shifts were referenced to external $BF_3 \bullet OEt_2$, while the ^1H, $^1H\{^{11}B\}$, and $^{13}C\{^1H\}$-NMR shifts were referenced to $SiMe_4$. Chemical shifts are

reported in units of parts per million downfield from reference, and all coupling constants in Hz. The mass spectra were recorded in the negative ion mode using a Bruker Biflex MALDI-TOF-MS [N_2 laser; λ_{exc} 337 nm (0.5 ns pulses); voltage ion source 20.00 kV (Uis1) and 17.50 kV (Uis2)].

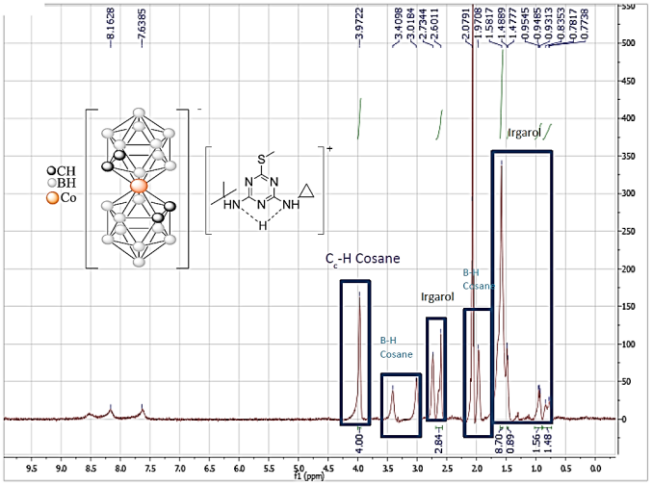

Figure 3. ^{1}H-NMR of the Irgarol-Cosane ion pair complex.

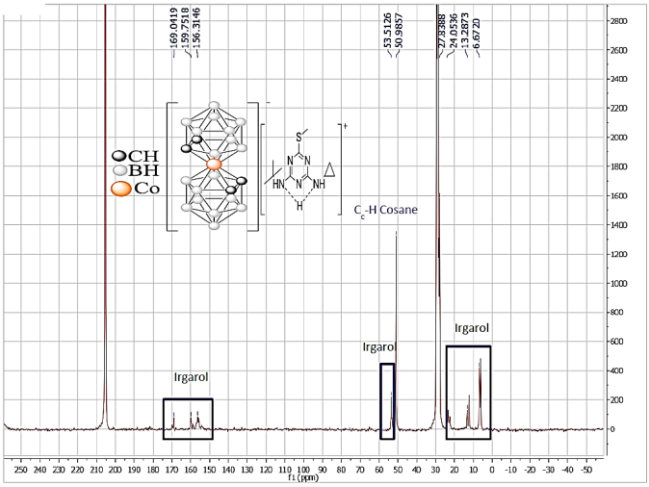

Figure 4. ^{13}C-NMR of the Irgarol-Cosane Ion Pair complex

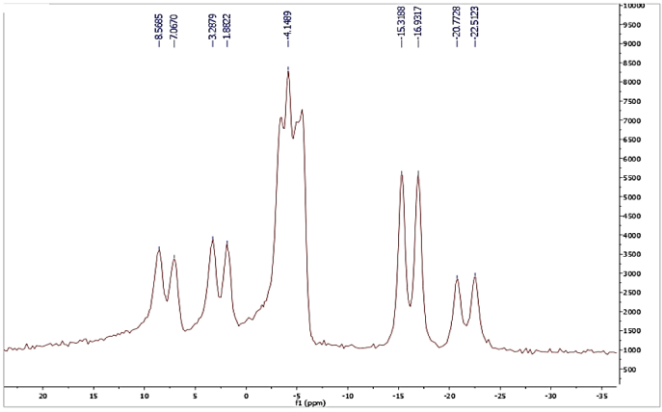

Figure 5. ^{11}B-NMR of the Irgarol-Cosane Ion Pair complex

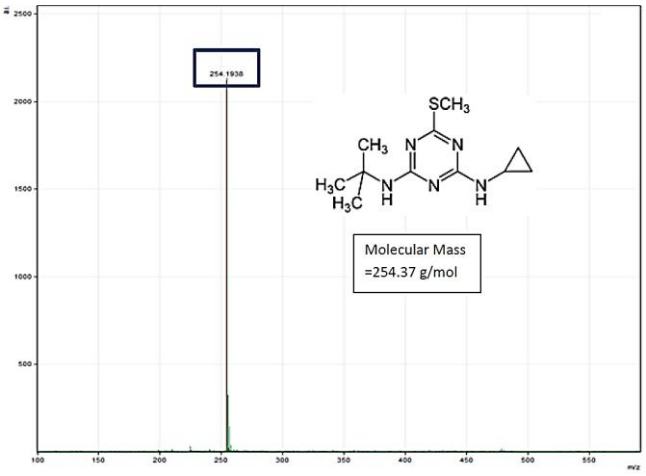

Figure 6. MALDI-TOF Spectra of the Cosane-Irgarol Ion Pair Complex. The peak at the expected molecular mass of the complex confirms the presence of the ion pair complex.

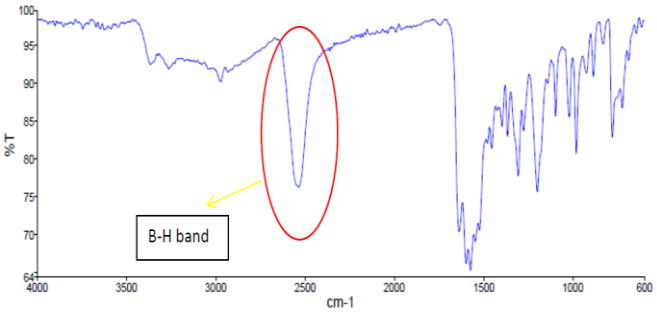

Figure 7. IR Spectrum of the Cosane Irgarol Ion pair complex. The band stretching in the IR spectrum of the ion pair complex around the 2500 cm^{-1} mark corresponds to the expected B-H band stretching of the Carboranyl group thus confirming the presence of Cosane in the complex.

3.1.2.2 Microelectrode Preparation

The microelectronics fabrication process for the planar microelectrodes was performed at the Centro Nacional de Microelectronica (CNM).[27] The fabrication procedure consists of two photolithographic steps. A P-type <100> silicon wafer, 100 mm in diameter with a nominal thickness of 525 μm acts as the starting material, upon which an oxide layer of 0.8 μm thickness is grown by thermal oxidation. Following the application of a first photoresist layer, a double metal layer (50 nm Ti plus 150 nm Pt) layer is deposited. The metal layer is patterned by the so-called lift-off technique. This is followed by the deposition of two PECVD layers of SiO_2 and Si_3N_4, which act as a passivation layer. The second photolithographic process opens up the passivation on the active Pt microelectrodes and on the soldering pads.

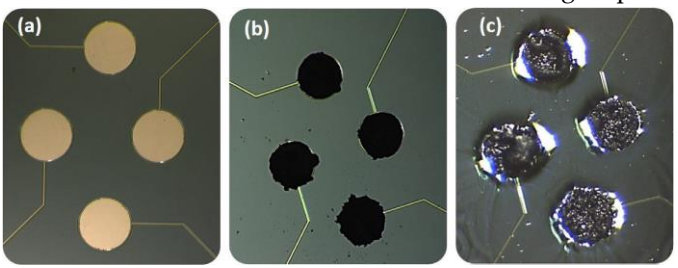

Figure 8. (a) bare Pt microelectrodes, (b) Ppy-conductive-layer modified microelectrodes and (c) microelectrodes covered with the Irgarol selective polymeric membrane.

The passivation layer is then etched, followed by dicing the wafer and mounting the chips to a specially designed printed circuit board (PCB) as shown in **Fig. 8** and then wire-bonded in the usual manner. The entire region of the PCB, including the bonding area and wires are protected

using an epoxy resin to protect them from the liquid environment.

3.1.2.3 Conductive Polymer layer growth

Polypyrrole doped with $[Co(C_2B_9H_{11})_2]^-$anion was grown on the platinum substrate to improve the mechanical and electrical contact between the surface of the electrode and the polymeric membrane containing the ion pair complex which is deposited later upon the electrode.. To this end, a layer of conductive polymer, $PPy[Co(C_2B_9H_{11})_2]$ was grown galvanostatically to act as the solid internal contact on the microelectrode. This layer was grown by electropolymerization on the platinum micro-electrodes with a solution of 0.035M $Cs[Co(C_2B_9H_{11})_2]$ and 0.1 M Pyrrole in acetonitrile with 1 wt.% in water. The electrochemical polymerization of polypyrrole doped with $[Co(C_2B_9H_{11})_2]^-$ anion was carried on by applying 10 potential sweep cycles between -0.6 V and 1.2 V, at a scan rate of 100 mV/s by means of CV. Polypyrrole gets oxidised upon the application of an anodic potential, which leads to localization of positive charges in bipolar states and stabilization by resonance in the conjugated polymer chain [28].The introduction of $[Co(C_2B_9H_{11})_2]^-$anion leads to charge neutrality. The many advantages of using this anion for this purpose have already been discussed in the introductory chapter. The porous polypyrrole layer formed enables the polymeric membrane to establish full contact between the sensing membrane and the electrode contributing to the long shelf life of the sensors as it prevents the appearance of air and liquid bubbles between the flat transducer surface and the

polymeric membrane, avoiding partial detachment. This leads to an enhancement in the electrical properties of the electrode. It can be seen from the CV plot in **Fig. 9** how redox peaks increase in current intensity due to the presence of a conducting polymer that enhances the electrical properties of the electrode. After polymerization, the micro-electrodes were rinsed with water and dried under nitrogen before the deposition of the polymeric membrane layer containing the Ion Pair complex.[29]

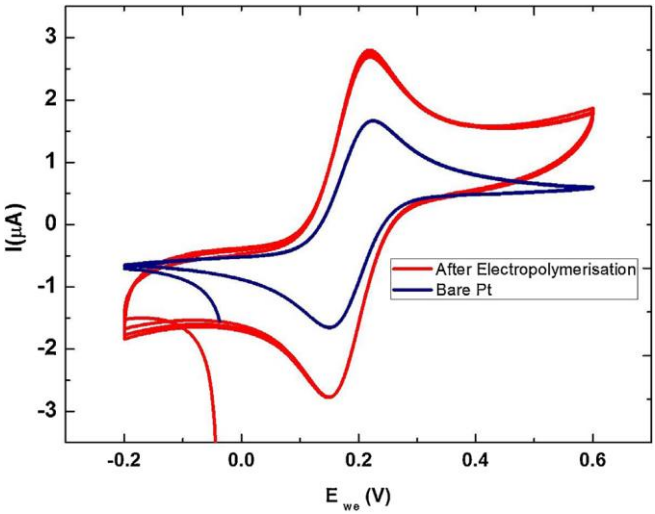

Figure. 9. Cyclic voltammograms of platinum microelectrode before and after electrochemical polymerization of PPy[$Co(C_2B_9H_{11})_2$] conductive layer. Scan Rate:100 mV/s. Cyclic voltammogram of gold microelectrode was carried out in redox probe $K_3[Fe(CN)_6]/K_4[Fe(CN)_6]$ 5 mM in phosphate buffer solution. Potential scanned from −0.2 to 0.6 V vs SCE at scan rate of 100 mV/s.

3.1.2.4 Polymeric Membrane Preparation

The membrane to be deposited on top of the microelectrode consists of the following components-

a) Polymeric matrix
b) Plasticizer
c) Ion Pair complex

As mentioned above, PVC is the standard choice as polymeric matrix to be used in potentiometric sensors of this type. We used 3 different plasticizers, namely, O-Nitrophenyl Octyl Ether (NPOE), Bis (2-ethyl hexyl)Sebacate (DOS) and Di-Octyl Phthalate (DOP) to prepare 3 different ISEs, each with one different plasticizer. Many different compositions in terms of w/v ratio of the 3 different components were tried but the best results were obtained by the following composition- 30 wt.% PVC, 63 wt.% plasticizer and 7 wt.% $[C_{11}H_{20}N_5S][Co(C_2B_9H_{11})_2]$ ion pair complex. All of these components were dissolved in 1.5 mL of TetrahydroFuran (THF) and deposited directly on top of the electroactive area of the microelectrode and left overnight to dry.

3.1.2.5 Potentiometric Measurements

The potentiometric measurements were done using multichannel homemade data acquisition system connected with four micro-electrodes simultaneously. These measurements were done at room temperature and controlled via a personal computer. A saturated calomel electrode with KCl as inner solution was used as the

reference electrode. Irgarol solutions of concentrations ranging from

10^{-5} M to 10^{-1}M were prepared and successive aliquots of these were added to 25 mL distilled water under magnetic stirring. This was in keeping with the Generalized Standard Addition Method and Irgarol concentration in the media was increased from 10^{-8}M to 10^{-3}M.

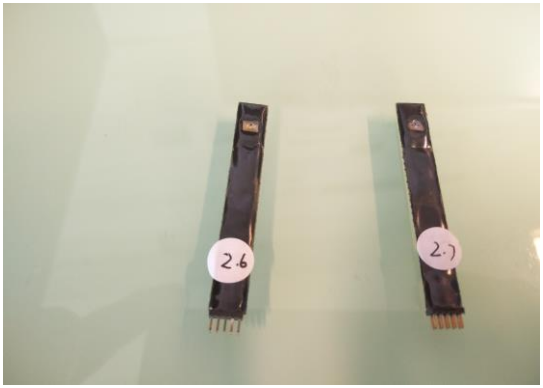

Figure 10. a) The actual micro-ISE used for measurements

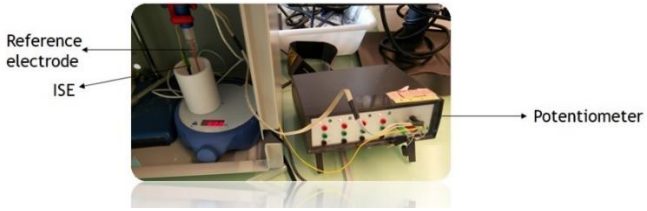

Figure 10. b) The Potentiometric measurement apparatus. The system is controlled by a homemade multichannel potentiometer.

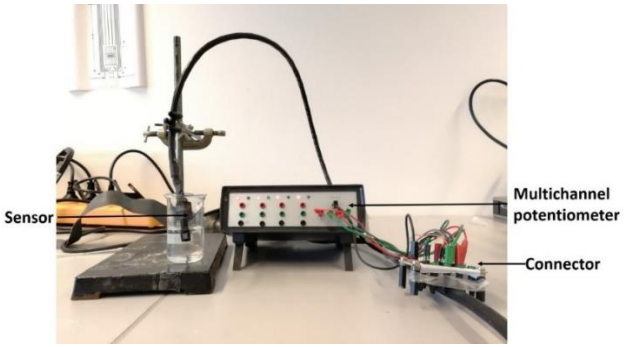

Figure 10. c) A single-device electrochemical cell operating simultaneously with four WEs enabling to perform electrochemical measurements in small volumes.

3.1.3 Response Characteristics

All the different components of the polymeric membrane play crucial roles in the performance of the ISE. The Ion Pair Complex acts as the recognition site in a potentiometric sensor. The use of $[Co(C_2B_9H_{11})_2]^-$ anion based ion pair complexes leads to great selectivity and hydrophobicity. The many advantages of using $[Co(C_2B_9H_{11})_2]^-$ anion in Ion Pair Complexes have already been mentioned in the introductory chapter section 1.2 of this chapter.

Microelectrode characteristics such as dielectric constant of the membrane, ionophore mobility and ligand state are influenced by the nature of the plasticizer used. In addition, plasticizers should also have high molecular weight, high lipophilicity and should be compatible with other membrane components to provide stability. The choice of plasticizer is influenced by the use of the ISE. In

this case, we tested 3 different plasticizers, NPOE, DOS and DOP. Since this ISE is designed for use in water, a polar solvent, deposits of charged species may cause potential drifts and hence non polar plasticizers like DOS and DOP are preferred. Expectedly, they showed better results when used in the polymeric membrane when compared to the highly polar NPOE.

3.1.3.1 Potentiometric Response

3 different ISEs, each with a different plasticizer, were fabricated and each ISE had 4 working microelectrodes. The analytical performance parameters of the different ISEs prepared for detection of Irgarol are summarized in Table 1. One of the most important parameters that characterizes the performance of an ISE is the limit of detection. As can be seen from Table 1, the plasticizers affected the performance of the ISE and the best results were obtained with using DOS as the plasticizer.

Plasticizer	Slope (mV/decade)	Correlation Coefficient	Detection limit (mol/dm^3)	Response Time (s)	Lifetime (day)
DOP	56.67$\pm$ 2.3	0.9990	3 x 10^{-6}	<10	>45
DOS	57.17 $\pm$ 1.7	0.9992	2 x10^{-6}	<10	>45
NPOE	48.21 $\pm$ 6.4	0.9996	4 x 10^{-6}	<10	>45

Table 1. The primary response parameters of an ISE. Sensitivity (Nernstian slope), correlation coefficient, detection limit, time response and lifetime of different plasticizers-based ISEs for the detection of Irgarol.

Fig. 11 represents the potentiometric response of the 3 ISEs with different plasticizers. From Table 1 and Fig. 10

it is clear that the ISE with DOS as the plasticizer gives the best results with a lowest detection limit of 2 μm/L and a Nernstian slope of 57.17. Hence, the ISE with DOS was chosen for further studies about pH response and selectivity.

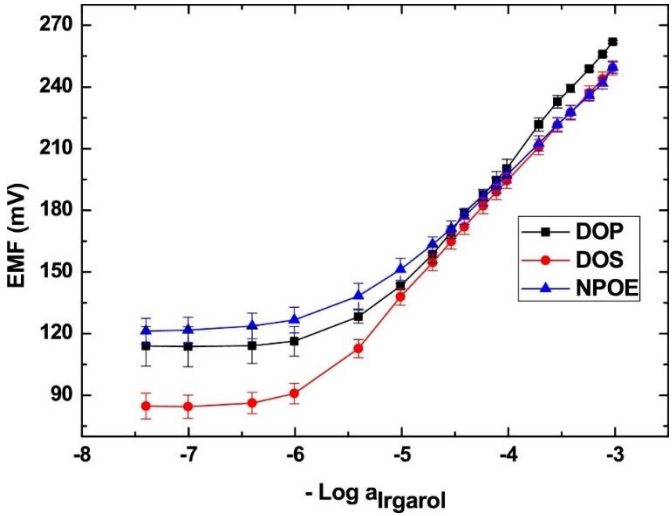

Figure 11. Potentiometric response of Irgarol-Ion Selective microelectrodes with different membrane composition of plasticizers.

3.1.3.2 Selectivity

Any ISE used for potentiometric detection in water will encounter a lot of interfering species other than the analyte of interest. To be sure that the ISE readings are not affected by the presence of these interfering species, the ISE needs to have high selectivity. We made use of the Nicolsky Eisenmann equation to determine the Potentiometric Selectvity Coefficient, $K_{A,BPot}$. [30]-[31] The Fixed Interference Method (FIM) was used to calculate this coefficient, this method involves measurement of

solutions of constant interference activity, in this case having concentration 10^{-3}mol/dm^3 of the interfering ion while increasing the activity of Irgarol from 10^{-8} to 10^{-3}mol/dm^3. Algaecides belonging to the same structural group as Irgarol (**Fig. 12**) were chosen to act as interfering ions for the selectivity studies. Ions commonly found in water such as NaCl and KCl were also used for these studies. The electrochemical cell used was based on a reference and a working electrode immersed in 25 mL of 1 mM solution of an interfering species. The response of Irgarol in the presence of interferences was compared to the response in water. For the calculation of $K_{A,Bpot}$ the EMF values obtained were plotted as a function of the logarithm of the activity of the analyte. By extrapolating the value at the intersection point of the linear portions of this plot, we get analyte activity that is used to calculate $K_{A,Bpot}$ from the Nikolsky-Eisenman equation. The results obtained from the potentiometric selectivity coefficient measurements are presented in Table 2.

Name of Interference (10^{-3} mol/dm^3)	**Log $K_{A,Bpot}$**
Ametryn	-3.000
Atrazine	-1.698
Cyanazine	-2.698
Prometryn	-3.000
Propazine	-2.000
Simazine	-3.000
Terbutryn	-2.698
Terbumeton	-2.698
Terbutylazine	-1.397
NaCl	-3.020
KCl	-3.015

Table 2. Cross-selectivity of the ISE prepared with DOS as plasticizer. Selectivity coefficient obtained through the FIM for a fixed interference concentration of 10^{-3} mol/dm^3.

Its clear from the values in Table 2 that this ISE is highly selective towards Irgarol even in the presence of similarly structured interfering ions. In the case of Ametryn, Prometryn, Simazine, NaCl and KCl it showed 3 orders of magnitude more selectivity towards Irgarol than the interfering ions, i.e, in other words it was 1000 times more selective towards Irgarol than it was towards the respective interfering ion. In the case of Cynazine, Propazine, Terbutryn and Terbumeton the ISE was at least 2 orders of magnitude more selective towards Irgarol. Atrazine and Terbutylazine caused the most interference but even in these cases, the ISE was at least 10 times more selective towards Irgarol.

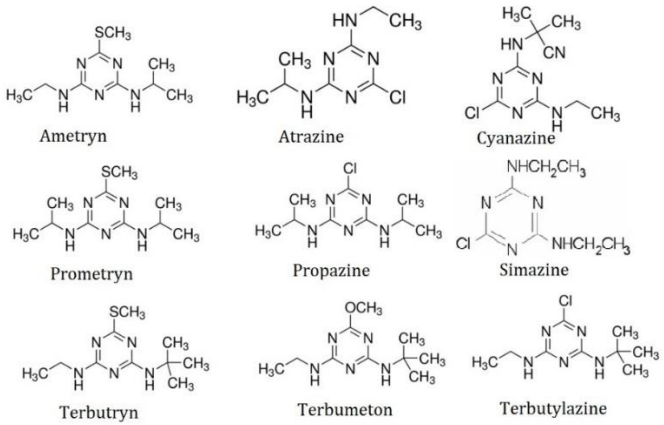

Figure 12. Chemical structures of compounds used as Interferences.

3.1.3.3 Lifetime

Lifetime of the ISE is dependant upon the sensitivity of the polymeric membrane. As the sensitivity of the membrane

decreases, the performance of the ISE is adversely affected. The lipohilicity and stability of the Ion pair complex and the plasticizer are responsible for the sensitivity and hence, lifetime of the ISE. As previously mentioned, properties of the $[Co(C_2B_9H_{11})_2]^-$ anion such as its lipophilicity, low charge density, the ability to form dihydrogen bonds and to be covalently bonded to the plasticizer lead to good stability between the plasticizer and ion pair complex, hence increasing the overall stability of the polymeric membrane. It is these advantages that the $[Co(C_2B_9H_{11})_2]^-$ anion has over other organic and inorganic anions which makes it so attractive for use in ISEs. Another important property of this anion which leads to increased stability (and hence lifetime) is its ability to produce weak B H· · ·H N dihydrogen bonds with the electro-active cations. This increased stability maintains the sensitivity of the polymeric membrane for a longer period, hence, increasing the lifetime of the ISE.

Here, the lifetime of the ISE with DOS as plasticizer was studied for a period of 45 days since membrane preparation to see if it showed any appreciable degradation, but there was none. As it can be observed from Table 3 and **Fig. 13** the response parameters and the calibration curve characteristics of the membrane remain the same over a time period of 45 days. So, it can be demonstrated that the ISE remains functional without any degradation in performance, despite repeated use over a period of 45 days.

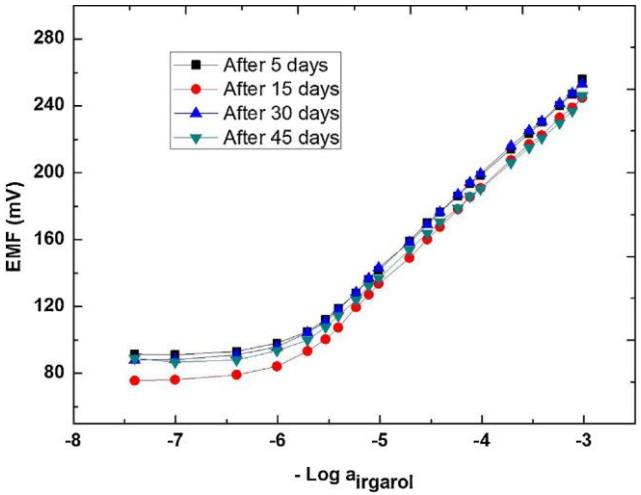

Figure 13. Response of Irgarol ISEs over different time periods with DOS as plasticizer

Time period since membrane preparation	Slope (mV/decade)	Concentration Range (mol/dm^3)	Limit of detection (mol/dm^3)
5 days	56.00	1 x 10^{-8} to 1 x 10^{-3}	2 x 10^{-6}
15 days	57.16	1 x 10^{-8} to 1 x 10^{-3}	2 x 10^{-6}
30 days	56.31	1 x 10^{-8} to 1 x 10^{-3}	2 x 10^{-6}
45 days	53.56	1 x 10^{-8} to 1 x 10^{-3}	2 x 10^{-6}

Table 3. Response of Irgarol ISE prepared with DOS as plasticizer over different time periods.

3.1.3.4 Response Time

The response time of the ISE is dependant on the thickness of the polymeric membrane as well as the thickness of the conductive polymer PPy[Co($C_2B_9H_{11}$)$_2$] layer. The time taken for the ISE to register a response is a very important parameter with regards to its application for real time detection. As a consequence, the ISE must give a very fast response and in the case of this particular ISE, an equilibrium response was observed in less than 10 seconds as demonstrated in **Fig. 14**. The **Fig. 14** shows the corresponding potential versus time plot after the concentration of Irgarol was changed from 8 x 10^{-6} M to 1 x 10^{-5} M by GSAM in 25 mL of distilled water. Since the response of the ISE is very fast, it can be concluded that the thickness of the polymer layers are of an appropriate level and not so thick as to interfere with response of the ISE.

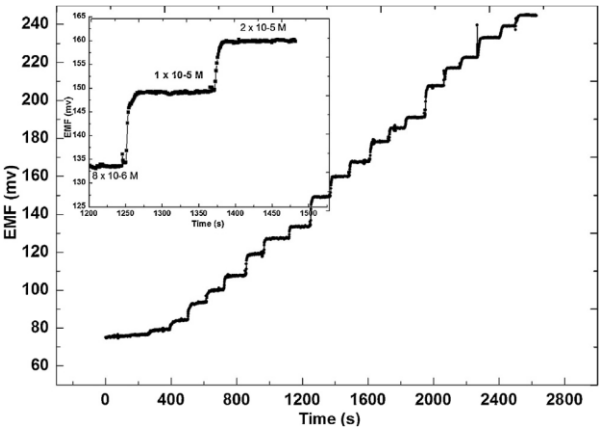

Figure 14. Dynamic response of one of the Irgarol ISEs for step changes in the concentration of Irgarol. Potentiometric measurements carried out using a two-electrode electrochemical cell following the GSAM.

3.1.3.5 pH Response

To the test response of the ISE at different pH, a 10^{-3}M solution of Irgarol was taken and its pH was increased from 1.5 to 12 using 1M NaOH solution. The ISE was unstable in pH range from 1.5 to 6 but showed a relatively stable response from pH 6 to 12. Since, this ISE was designed to be used for detection of Irgarol in water, which has a pH of 7, the working range of this ISE is appropriate. There is a slight change of around 20 mV in the working pH range and that can be explained as follows- The electroactive part of the ISE consists of Irgarol-H^+ in a protonated form in the membrane. It acts as the cation to compensate the negative charge of $[Co(C_2B_9H_{11})_2]^-$, which is necessary to provide stability to the membrane. The analyte is not totally in this form, owing to the need for good solubility of the analyte. Thus, there is a difference between the Irgarol form within the membrane and in the water solution and this leads to potential shift of around 20 mV/decade in the working pH range, but this has not been found to have an appreciable effect on the measurements. The Reiley diagram showing the effect of pH on the electric potential of the ISE is depicted in **Fig. 15.**

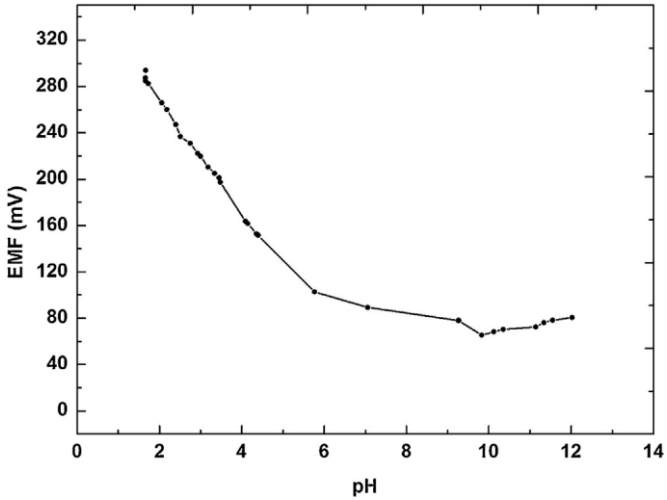

Figure 15. Reilley diagram showing the effect of pH on the emf of the Irgarol ISE. The pH working range is measured increasing the pH of a 1 mM solution of Irgarol by titration of small aliquots of NaOH 1 M solution.

All the results and figures presented in this chapter have been published in Sensors and Actuators B: Chemical. [32]

3.1.4 Conclusions

The previously problematic detection of Irgarol in water has been simplified using a micro Ion Selective Electrode. This ISE makes use of a polymeric membrane comprising of $[C_{11}H_{20}N_5S][Co(C_2B_9H_{11})_2]$ as the ion pair complex. The metallacarborane anion $[Co(C_2B_9H_{11})_2]^-$which is available as the Cesium salt can be either hydrophobic or hydrophilic depending upon the cation. Its ability to produce weak hydrogen and dihydrogen bonds along with its electroactivity and redox reversibility make it an

extremely appealing anion to be used in sensing materials. The Ion pair complex is incorporated into a PVC membrane along with different plasticizers. In this work, the ISE prepared for Irgarol detection having composition as 63% Bis(2-ethylhexyl) Sebacate (plasticizer),30% PVC (polymer matrix) and 7% $[C_{11}H_{20}N_5S][Co(C_2B_9H_{11})_2]$ ion-pair complex worked better than different compositions. ISE prepared with Bis(2-ethylhexyl) Sebacate as plasticizer showed better performance than ISEs prepared using other plasticizers. The ISE reported here showed extremely promising results and the lowest detection limit achieved was 2×10^{-6} mol/dm^3 and it showed a stable response between pH 6 and 12 making it ideal for use in water. It also showed great selectivity in presence of interfering ions belonging to the same class of compounds as Irgarol. The ISE reported here gave a very quick response time of less than 10 seconds and could be used repeatedly for a period of 45 days without any degradation in its response parameters.

3.1.5. References

1. B. Dahl, H. Blanck, *Mar. Pollut. Bull.* **32** (1996) 342–350.
2. S. Balakrishnan, K. Takeda, H. Sakugawa, *Geochem. J.* **46** (2012) 169–177.
3. J.W. Readman, et al., *Environ. Sci. Technol*. **27** (1993) 1940–1942.
4. M.A. Gough, J. Fothergill, J.D. Hendrie, *Mar. Pollut. Bull.***28** (1994) 613–620.
5. S.D.W. Comber, M.J. Gardner, A.B.A. Boxall, *J.Environ. Monit*. **4** (2002) 417–425.
6. H. Okamura, I. Aoyama, Y. Ono, T. Nishida, *Mar. Pollut. Bull*. **47** (2003) 59–67.
7. H. Harino, Y. Mori, Y. Yamaguchi, K. Shibata, T. Senda, *Arch. Environ. Contam. Toxicol.* **48** (2005) 303–310.
8. J. Penalva, et al., *Anal. Chim. Acta*. **387** (1999) 227–233.
9. B. Ballesteros, D. Barcelo, F. Sanchez-Baeza, F. Camps, M.P. Marco, *Anal.Chem*. **70** (1998) 4004–4014.
10. J. Williams, A. Thorpe, L. Reynolds, *Int. J. Environ. Anal. Chem*. **65** (1996) 149–152.
11. R. Bloch, A. Shatkay, H.A. Saroff, *Biophys. J.* **7** (1967) 865–877.
12. G.J. Moody, R.B. Oke, J.D.R. Thomas, *Analyst.* **95** (1970) 910–918.
13. Z. Stefanac, W. Simon, *Microchem. J.* **12** (1967) 125–132.
14. S. Peper, M. Telting-Diaz, P. Almond, T. Albrecht-Schmitt, E. Bakker, *Anal. Chem.*, **74** (2002) 1327-1332.
15. S. Peper et al., *Anal. Chem.*, **75** (2003) 2131-2139.
16. A. I. Stoica, C. Vinas, F. Teixidor, *Chem. Commun.* **48** (2008) 6492–6494.
17. A. Errachid, et al., *Nanotechnology*, **18** (2007), 485301.
18. N. Zine, et al., *Mater. Sci. Eng., C*, **26** (2006), 399-404.
19. M. Krondak, R. Volk, V. Kral, *Collect. Czech. Chem. Commun.*, **66** (2001), 1659-1664.
20. C. Masalles, F. Teixidor, S. Borrós , C. Viñas, *J. Organomet. Chem.*, **657** (2002), 239-246.
21. C. Masalles, J. Llop, C. Viñas, F. Teixidor, *Adv. Mater. (Weinheim, Ger.)*, **14** (2002), 826-829.
22. E. Bakker, E. Pretsch, *Angew. Chem., Int. Ed.*, **46** (2007), 5660-5668.
23. C. Masalles, J. Llop, C. Vinas, F. Teixidor, *Adv. Mater.* **14** (2002) 826–829.

24. J. Giner-Planas, et al., *J. Am. Chem. Soc*. **127** (2005)15976–15982.
25. L.M. Epstein, E.S. Shubina, *Coord. Chem Rev*. **231** (2002) 165–181.
26. A.I. Stoica, C. Kleber, C. Vinas, F. Teixidor, *Electrochim. Acta.* **113** (2013) 94–98.
27. N. Zine, et al., *Sens. Actuators B* **91** (2003) 76–82.
28. A.J. Heeger, S. Kivelson, J.R. Schrieffer, W. P. Su, *Rev. Mod. Phys*. **60** (1988) 781–850.
29. C. Masalles, S. Borros, C. Vinas, F. Teixidor, Adv. Mater. **12** (2000) 1199–1202.
30. Analytical chemistry division, commission on analytical nomenclature, Recommendations for nomenclature of ion-selective electrodes, Recommendations –1975, *Pure Appl. Chem*., **48**, (1976) 127.
31. R. Buck, E. Lindner, Recommendations for nomenclature of ion selective electrodes (IUPAC Recommendations 1994), *Appl. Chem*. **66** (1994)2527–2536.
32. A. Saini, et al., *Sens. Actuators B* **268** (2018) 164-169.

3.2. Potentiometric Ion-Selective Electrode For Sulfapyridine Detection

The [Sulfapyridine-H]$^{+}$[Co($C_2B_9H_{11}$)$_2$]$^{-}$ ion pair complex was used to prepare a PVC matrix based selective microelectrode for detection of Sulphonamides. This novel Ion Selective electrode gives low limit of detection and high selectivity for the detection of Sulfapyridine in water.

Abhishek Saini
ICMAB-CSIC (UAB)

CONTENTS

3.2.1 Introduction

Sulphonamides are anti-bacterial agents that have been known to be carcinogenic if ingested. [1]-[2] They enter the food chain as they are used amongst livestock to prevent infections and cure infectious diseases, but their residues are left among meat and dairy products consumed by humans, thus causing potential danger to humans. [3]-[4]

Over the years, there have been many attempts to trace the presence of sulphonamides in our food chain and many methods have been employed to this end. These include Thin layer chromatography, Gas Chromatography coupled to Electron Ionization Mass Spectroscopy, Gas Chromatography with Atomic Emission Detection, Capillary zone electrophoresis coupled with nano-electrospray Mass Spectroscopy, Liquid Chromatography interfaced with fluorescence detection. [5]-[11] But most of these techniques have severe drawbacks limiting their widespread use. These drawbacks are listed below in Table 1.

Detection Technique	Drawback
Thin Layer Chromatography	Poor selectivity and prone to interferences
Gas Chromatography	Requires complex pre-conditioning
Capillary Zone Electrophoresis	Requires pre detection cleaning procedure
Liquid Chromatography	Non-specific detection and poor resolution

Table 1. Drawbacks of common Sulphonamide detection techniques.

These drawbacks highlight the necessity for the development of a cheaper and simpler method of

detection for Sulphonamides. In the past few decades, electrochemical methods of detection were developed and they reported faster and accurate detections as well as being cost effective. [12]-[16] It was the success of these Electrochemical methods of detection that acted as the motivation to try and develop a simple to use and inexpensive microsensor for Sulphonamide detection in water.

3.2.1.1 Micro Ion Selective Electrode for Sulfapyridine detection

Here, it is described a micro ISE for the potentiometric detection of Sulfapyridine, a compound belonging to the Sulphonamides class of compounds. Sulfapyridine was chosen as a representative of the Sulphonamide class of compounds to demonstrate that the technique of developing an Ion Pair complex with the [3,3'-Co(1,2-closo-$C_2B_9H_{11})_2]^-$ anion (as described in Section 3.1) could also be applied to the Sulphonamides class of compounds for their detection in water. Although a large number of ISEs have been generated using the [Co(1,2-closo-$C_2B_9H_{11})_2]^-$ anion based on ion pair complexes of the type [cation- NH]$^{n+}$ [3,3-Co(1,2-closo-$C_2B_9H_{11})_2]^-$, this type of interaction for Sulphonamides has not been studied. Hence, the development of a new ISE for potentiometric detection of Sulphonamides, using Sulfapyridine as an example.

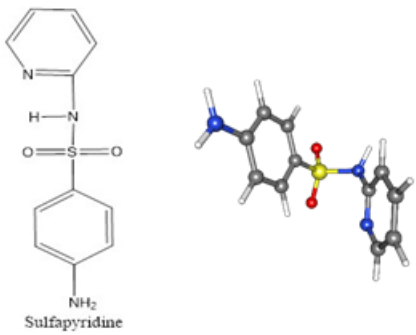

Figure 1. Sulfapyridine molecule

3.2.1.2 Use of Cobaltabisdicarbollide $[Co(C_2B_9H_{11})_2]^-$ anion

The reasons for using the $[Co(C_2B_9H_{11})_2]^-$ anion for use in Ion Pair complexes have already been elaborated in Section 3.1 and in the Introduction. The major reasons for its use are due to its properties as an electroactive ion-generator of the interactions within the components of the membrane that leads to a stable entity. [17]-[20]

As explained previously, polymeric (PVC) membranes are used in ISEs due to their simple and low-cost nature as instruments for electrochemical detection. [21]-[23]

As established in the previous chapter, the use of ISEs based on the composition: 30 wt.%- PVC

- 63 wt.%- Plasticizer
- 7 wt.%- Ion pair-complex

leads to low limit of detection and high selectivity for the detection of protonated antibiotics in water. Hence, this composition was applied to the micro ISE for the detection of sulfapyridine.

3.2.2 Microelectrode Preparation and Ion Pair Complex formation

3.2.2.1 Ion Pair Complex Formation

The $[C_{11}H_{12}N_3O_2S][3,3'\text{-}Co(1,2\text{-}closo\text{-}C_2B_9H_{11})_2]$ (**Fig. 2**) ion pair complex was synthesized in aerobic conditions at room temperature as follows :

Cs $[3,3'\text{-}Co(1,2\text{-}closo\text{-}C_2B_9H_{11})_2]$ (300 mg, 0.657 mmol) was extracted with aqueous HCl 1M (15 mL) and diethyl ether (20 mL). The organic layer was shaken three times with fresh HCl 1M (with 15mL each time). Then, the diethyl ether was evaporated and the residue was diluted with water to generate 0.05M solution of H $[3,3'\text{-}Co(1,2\text{-}closo\text{-}C_2B_9H_{11})_2$ (solution 1). Sulfapyridine was dissolved in water by adding the minimal quantity of HCl 1M to prepare 0.05M acid solution (solution 2). Next,15 mL of solution 1 and 15 mL of solution 2 were mixed and after stirring a yellow precipitate was obtained. This was filtered off, washed with HCl 0.1M and dried in vacuum.

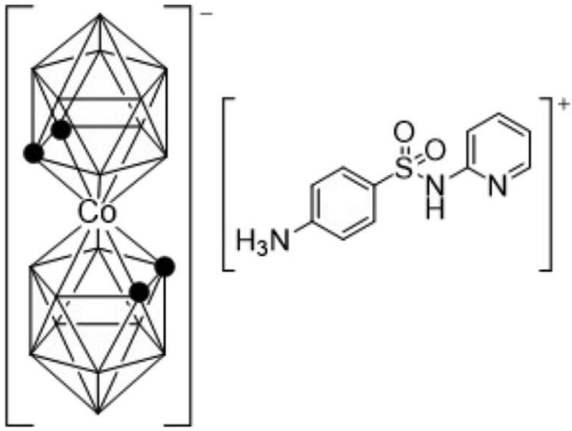

Figure. 2. Ion pair Complex: Chemical structure of the 3,3′-[Co(1,2-closo-$C_2B_9H_{11})_2$]·[Sulfapyridine]$^+$ ion pair complex.

The Ion Pair complex was analyzed by ^{1}H NMR integrating the C-Hs of metallacarborane resonances and comparing them with the aromatic 1H- resonances due to Sulfapyridine. The integration provided 4:8, these for metallacarborane C-H (4) and aromatic Sulfapyridine protons (8) indicating a 1:1 salt.

The ^{1}H- and ^{1}H{^{11}B}-NMR (300.13 MHz), ^{13}C{1H}-NMR (75.47 MHz) and ^{11}B- and ^{11}B{1H}-NMR (96.29 MHz) spectra were recorded on a Bruker ARX 300 instrument equipped with the appropriate decoupling accessories. All NMR spectra were performed in acetone deuterated solvent at 22^{o}C. The ^{11}B- and ^{11}B{1H}-NMR shifts were referenced to external BF3·OEt2, while the ^{1}H, ^{1}H{^{11}B}, and ^{13}C{^{1}H}- NMR shifts were referenced to $SiMe_4$. Chemical shifts are reported in units of parts per million downfield from reference, and all coupling constants in Hz.

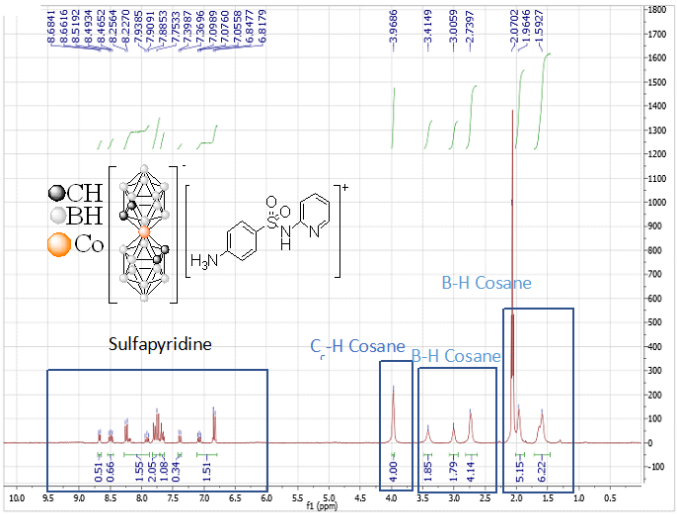

Figure 3. H-NMR of the $[Sulfapyridine\text{-}H]^{+}[Co(C_2B_9H_{11})_2]^{-}$ ion pair complex.

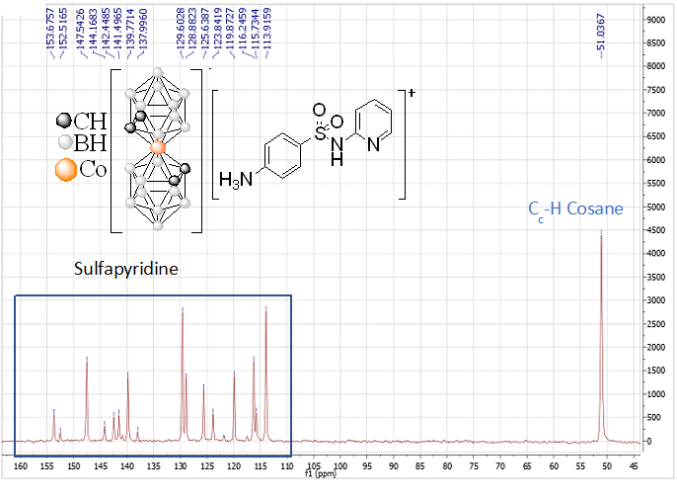

Figure 4. C-NMR of the $[Sulfapyridine\text{-}H]^{+}[Co(C_2B_9H_{11})_2]^{-}$ Ion Pair complex.

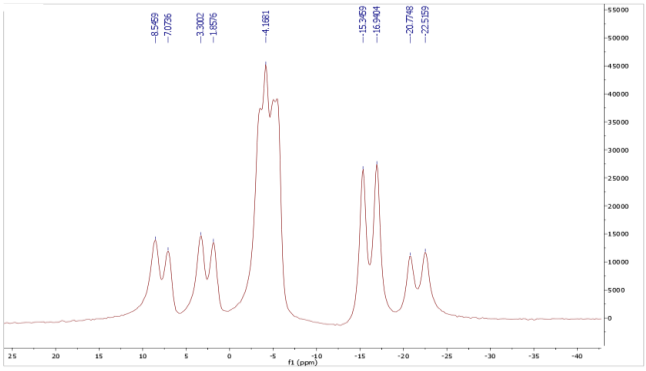

Figure 5. B-NMR of the [Sulfapyridine-H]$^{+}$[Co($C_2B_9H_{11}$)$_2$]$^{-}$ Ion Pair complex.

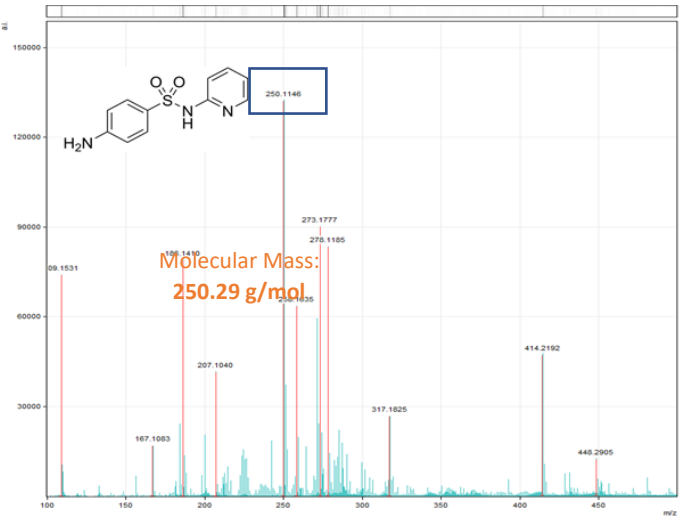

Figure 6. MALDI-TOF Spectra of the [Sulfapyridine-H]$^{+}$[Co($C_2B_9H_{11}$)$_2$]$^{-}$ Ion Pair Complex. The peak at the expected molecular mass of the complex confirms the presence of the ion pair complex.

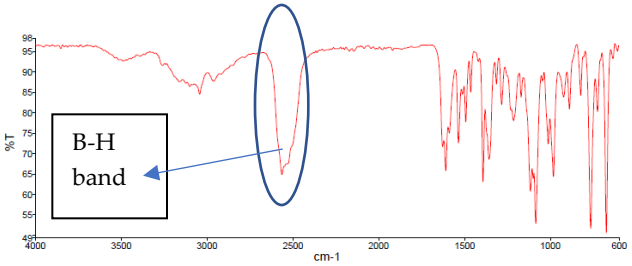

Figure 7. IR Spectrum of the [Sulfapyridine-H]$^{+}$[Co($C_2B_9H_{11}$)$_2$]$^{-}$ Ion pair complex. The band stretching in the IR spectrum of the ion pair complex around the 2500 cm^{-1} mark corresponds to the expected B-H band stretching of the Carboranyl group thus confirming the presence of [Co($C_2B_9H_{11}$)$_2$]$^{-}$ in the complex.

3.2.2.2 Microelectrode Preparation and Conductive Polymer layer growth

The microelectrode fabrication process and the subsequent growth of the conductive Polypyrrole [Co($C_2B_9H_{11}$)$_2$] layer has already been described in Section 3.1. The polymeric membrane is able to establish full contact between the sensing membrane and the electrode due to the porous polypyrrole layer. This leads to an enhanced lifetime for the sensors. This can be explained by the fact that the polypyrrole layer prevents the appearance of air and liquid bubbles between the flat transducer surface and the polymeric membrane, hence avoiding partial detachment which leads to an improvement in the electrode's electrical properties [20]. The introduction of [Co($C_2B_9H_{11}$)$_2$]$^{-}$ leads to charge neutrality. There are various other reasons for using [Co($C_2B_9H_{11}$)$_2$]$^{-}$ for this purpose and they have already been reported [24]. Similarly, it is well established in

literature and was also explained in Section 3.1 that the cyclic voltammogram of the platinum microelectrode in redox probe K_3 [$Fe(CN)_6$]/K_4 [$Fe(CN)_6$] 5mM in phosphate buffer solution after electrochemical polymerization of PPy [3,3′-Co(1,2-closo-$C_2B_9H_{11})_2$] show a marked increase in current intensity than the voltammogram before electropolymerization. It is due to the presence of a conducting polymer that enhances the electrical properties of the electrode [25]. The increase in surface area due to the electropolymerization of the pyrrole may also play a role in the increase in intensity of the electrode.

3.2.2.3 Polymeric Membrane Preparation

The membrane to be deposited on top of the microelectrode consists of the following components-

a) Polymeric matrix
b) Plasticizer
c) Ion Pair complex

As established in Section 3.1, the best composition for potentiometric detection by ISEs was found to be - 30 wt.% PVC, 63 wt.% plasticizer and 7 wt.% ion pair-complex. PVC was used as the polymeric matrix and we used 3 different plasticizers, namely, O-Nitrophenyl Octyl Ether (NPOE), Bis (2-ethyl hexyl)Sebacate (DOS) and Di-Octyl Phthalate (DOP) to prepare 3 different ISEs, each with one different plasticizer.

The performance of polymeric membranes is dependant on plasticizers to quite an important extent. The nature of the plasticizer used heavily influences the dielectric

constant of the membrane, the mobility of the ionophore molecules and state of the ligands. A plasticizer should be well matched with the other components of the polymeric membrane to provide stability. This is even more imperative when $[Co(C_2B_9H_{11})_2]^-$ acts as the companion ion of the electroactive cation, due to the strong non-bonding interaction between the $[Co(C_2B_9H_{11})_2]^-$ and the oxygen lone pairs of the plasticizer. It is also helpful if a plasticizer has high molecular weight and high lipophilicity. The choice of plasticizer is influenced by the nature of the ISE. In polar solvents like water, deposits of charged species may cause potential drifts and hence non polar plasticizers like DOS and DOP are preferred. The polar plasticizer NPOE was also used to compare its performance with the other 2 plasticizers.

All of these components were dissolved in 1.5 mL of Tetrahydrofuran (THF) and deposited directly on top of the electroactive area of the microelectrode and left overnight to dry.

3.2.2.4 Potentiometric Measurement

All electrochemical experiments were done by using a three-electrode electrochemical cell. It consists of a saturated calomel reference electrode, a platinum wire counter electrode and working microelectrode made of platinum substrate. The potentiometric measurements were done using multichannel homemade data acquisition system connected with four micro-electrodes simultaneously. These measurements were done at room temperature and controlled via a personal computer. A

saturated calomel electrode with KCl as inner solution was used as the reference electrode.

Sulfapyridine solutions with a concentration range of 10^{-5}M to 10^{-1}M were prepared to obtain the calibration curves. Successive aliquots of these solutions were added to 25 ml of distilled water for the potentiometric measurements. The measurements were made between the concentration range of 10^{-8} to 10^{-3} M, following the Generalized Standard Addition Method [26].

The Debye-Huckel equation is used in an aqueous solution for the measurement of the activity of an organic cation. This activity was reflected by the potential variations recorded whose value was plotted as a logarithmic function of Sulfapyridine activity.

The apparatus used for performing the measurements is the same as that shown in Section 3.1.

3.2.3 Response Characteristics

3.2.3.1 Potentiometric Response

The 3 ISEs, each with a different plasticizer were calibrated using the GSAM. The most important parameter for any ISE is its limit of detection and as can be seen from Table 2, the ISE using DOS as plasticizer gave the best response with a lowest detection limit of 1×10^{-6} mol/dm^3 and an almost Nernstian slope.

Plasticizer	Slope (mV/decade)	Correlation Coefficient	Detection Limit (mol/dm^3)	Response Time (s)	Lifetime (days)
DOP	61.26	0.9690	1 x 10^{-5}	<10	45
DOS	61.29	0.9936	1 x 10^{-6}	<10	45
NPOE	47.69	0.9787	4 x 10^{-6}	<10	45

Table 2. Response Characteristics of the ISE elaborated. Slope, correlation coefficient, concentration range, detection limit, time response and lifetime of different plasticizers for the detection of Sulfapyridine.

Fig. 8 represents the potentiometric response of the 3 ISEs, each with a different plasticizer. From Table 2 and **Fig. 8** we can conclude that the ISE with DOS as the plasticizer gives the best response and hence, was chosen for further studies regarding selectivity, lifetime and pH response.

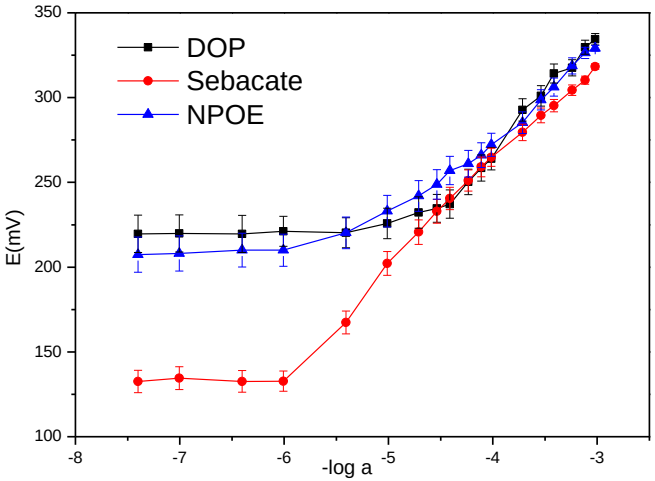

Figure 8. ISE response: Potentiometric response of Sulfapyridine selective ISE with different plasticizers in the membrane.

3.2.3.2 Selectivity

Selectivity of an ISE is an extremely important parameter with regards to its real-life usage. This is even more imperative in the case any compound belonging to the family of Sulphonamides as all these compounds are extremely similar in structure and this could easily lead to a false detection value.

The use of the $[Co(C_2B_9H_{11})_2]^-$ anion in this scenario is what makes the polymeric membrane extremely sensitive only to Sulfapyridine and not its sister compounds. Due to the electronegativity difference between B and C relative to H, it can be said that B-H and C-H bonds have inverted polarities. This causes the B-H bond to have tendency to generate hydrogen and dihydrogen bonding. Additionally, the C-H bonds in the $[Co(C_2B_9H_{11})_2]^-$ are highly polarized in comparison to organic compounds, which further enables hydrogen and dihydrogen bonding. In such a scenario $[Co(C_2B_9H_{11})_2]^-$ acts as a thistle, especially with molecular species that can form hydrogen bonds and their interaction with amines and protonated amines is very strong. So, in context of the polymer membrane described in this work, the $[Co(C_2B_9H_{11})_2]^-$ anion does not act as the sensing part, but it is the cation Sulfapyridine-H^+ that acts as the sensing part and hence leads to extremely high selectivity even amongst the presence of other sulphonamides.

The Nikolsky Eisenman equation was used to determine the potentiometric selectivity coefficient, $K_{A,Bpot}$. [27]-[28] The Fixed Interference Method (FIM) was employed to determine this potentiometric selectivity coefficient. This

method involves measuring solutions of constant activity, in this case having concentration 10^{-3} mol/dm3 of the interfering ion while varying the activity of Sulfapyridine from 10^{-8} to 10^{-3} mol/dm^3.

As mentioned above, compounds belonging to the Sulphonamide family were chosen for study as interfering ions, namely, Sulfamethizole, Sulfamethoxazole, Sulfanilamide and Sulfisoxazole (Fig. 9). The electrochemical cell used was based on a reference and a working electrode immersed in 25 ml of 1mM solution of an interference. The response of Sulfapyridine in the presence of interferences is compared to the response of ISE in water.

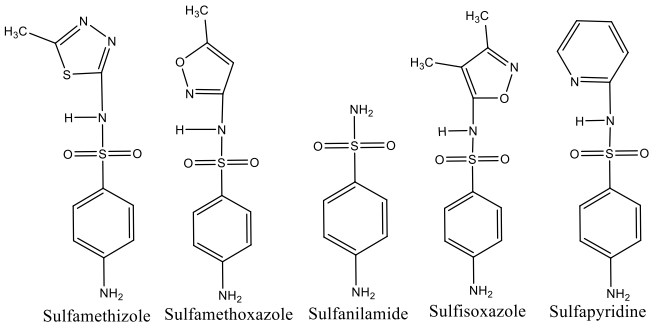

Figure 9. Interfering Ions: Chemical structures of compounds belonging to Sulphonamide class of compounds which have been used as interferences to measure selectivity of the ISE.

To calculate the $K_{A,Bpot}$, the EMF values obtained are plotted vs the logarithm of the activity of the analyte. From this plot, the value of the $K_{A,Bpot}$ was extrapolated at the intersection points of the linear portions of the plot. From this intersection point the $K_{A,Bpot}$ value is calculated using the Nikolsky Eisenmann equation. [29] The results

obtained from the potentiometric selectivity coefficient measurements are presented in Table 3.

Name of Interference	log $K_{A,BPot}$
Sulfamethizole	-2.698
Sulfamethoxazole	-3.000
Sulfanilamide	-3.096
Sulfisoxazole	-2.397

Table 3. Selectivity of ISE against interfering Sulphonamides.

As is clear from Table 3, Sulfisoxazole is the most interfering ion, but even in this case, the ISE is more than 2 orders of magnitude more selective towards Sulfapyridine than towards Sulfisoxazole, i.e, the ISE is at least 100 times more selective towards Sulfapyridine than any other Sulphonamide.

3.2.3.3 Lifetime

The lifetime of the ISE is essentially dependant on the ability of the polymeric membrane to maintain the concentration of the ion pair complex. Therefore, it is the lipophilicity of the membrane and the interaction of binding forces within its components that determine the lifetime of the ISE. The $[Co(C_2B_9H_{11})_2]^-$ anion is helpful in this regard due to its ability to self-assemble through dihydrogen C-H···H-B and N-H···H-B bonds and its amphiphilic character depending on the cation.[30]-[34] The ability of the $[Co(C_2B_9H_{11})_2]^-$ anion to covalently bond with the plasticizer has already been elaborated upon in Section 3.1. All these properties lead to a long and stable lifetime of the ISE. As the best performing ISE, the ISE with plasticizer DOS was subjected to longevity tests and

the ISE displayed a stable response for a period of 45 days as evidenced by Table 4 and **Fig. 10.**

Time since membrane preparation	Slope (mV/decade)	Concentration Range (mol/dm^3)	Limit of detection (mol/dm^3)
5 days	61.29	1 x10^{-8} to 1x 10^{-3}	1 x 10^{-6}
15 days	63.95	1 x10^{-8} to 1x 10^{-3}	1 x 10^{-6}
30 days	59.23	1 x10^{-8} to 1x 10^{-3}	4 x 10^{-6}
45 days	61.79	1 x10^{-8} to 1x 10^{-3}	4 x 10^{-6}

Table 4. Response of Ion Selective Electrode over different time periods.

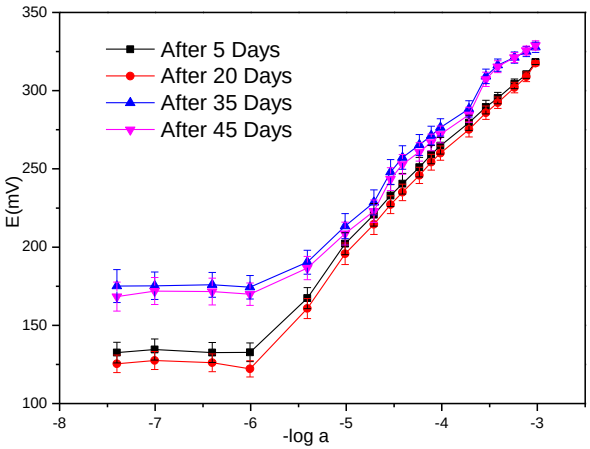

Figure 10. Lifetime of ISE: Potentiometric response of Sulfapyridine selective μISE over different time periods with Bis (2-ethyl hexyl) Sebacate as plasticizer.

3.2.3.4 Response Time

The response time is the time taken by the electrode to achieve a stable potential and in this study, it was found to be less than 10 seconds in all cases.

The response time is strongly dependant on the polymeric membrane and the conducting polymer PPy[$Co(C_2B_9H_{11})_2$] being of optimal thickness. This is because, more the concentration of anionic sites in the membrane, lesser is the coextraction of the primary ion and, hence, quicker is the response time. [35] If the thickness of the polymer layer is too much, it will hinder the coextraction and hence increase the response time, hence, necessitating the thickness to be optimal.

3.2.3.5 pH Response

To the test the pH dependence of the ISE, a 10^{-3}M solution of Sulfapyridine was taken and its pH was increased from 1.5 to 12 using 1M NaOH solution.

The effect of the $[Co(C_2B_9H_{11})_2]^-$ anion and Ion Pair complex on the pH dependence of the ISE has already been described in Section 3.1. As shown in Fig. 11 the pH influence on the EMF value is negligible in the range of pH between pH 6 and 9. This led us to avoid buffered solutions to do the testing while adjusting the pH within this interval by addition of NaOH 1M. Since the purpose of the ISE is to test presence of Sulfapyridine in water bodies, which have pH around 7, the working range of pH 6-9 is appropriate.

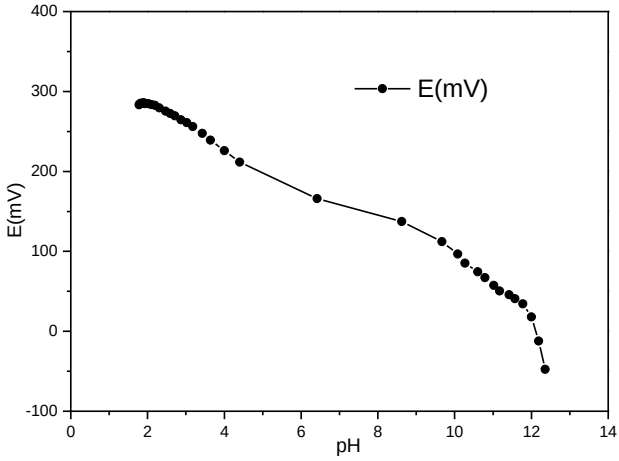

Figure 11. pH response: Reilley diagram showing the effect of pH variation on the EMF of the Sulfapyridine selective ISE. The μISE gives a stable EMF signal between pH 6 and 8. The pH working range is measured by increasing the pH of a 1 mM solution of Sulfapyridine by titration with small aliquots of NaOH 1 M solution.

All the results and figures presented in this chapter have been published in the Journal of Organometallic Chemistry. [36]

3.2.4 Conclusions

A micro Ion Selective Electrode for the potentiometric detection of Sulfapyridine in water has been described here. The compound Sulfapyridine has been used as an example of the Sulphonamides class of compounds and the same methodology can be used to prepare an ISE for the detection of any Sulphonamide. The polymeric membrane in the ISE consists of protonated sulfapyridine and the organometallic anion cobaltabisdicarbollide, $[C_{11}H_{20}N_5S][3,3'\text{-}Co(1,2\text{-}closo\text{-}C_2B_9H_{11})_2]$ ion-pair complex, PVC and different plasticizers. In the context of this work, the polymeric membrane composed of 63% Bis(2-ethylhexyl) Sebacate (plasticizer), 30% PVC (polymer matrix) and 7% $[C_{11}H_{20}N_5S][3,3'\text{-}Co(1,2\text{-}closo\text{-}C_2B_9H_{11})_2]$ ion-pair complex showed a lowest limit of detection of 1×10^{-6} mol/dm^3, a working pH range between 6-9, a lifetime of at least 45 days and was at least 2 orders of magnitude more selective towards Sulfapyridine than other Sulphonamides.

3.2.5 References

1. O. W. Parks, *J. Assoc. Off., Anal. Chem.*, **68** (1985) 20-23.
2. N. A. Littlefield, W. G. Sheldon, R. Allen, D.W. Gaylor, *Food Sci. Toxicol*., **28** (1990) 157-167.
3. C. M. Stowe, in Veterinary Pharmacology and Therapeutics, ed. L. M. Jones, *Iowa University Press, Ames,* IA, (1965) 457.
4. D. E. D. Holland, S. E. Katz, *J. Assoc. Off. Anal. Chem*., **74** (1991) 784-789.
5. G. J. Reimer, A. Suarez, *J. Chromatogr. A.*, **555** (1991) 315-320.
6. V. B. Reeves, *J. Chromatogr. B.*, **723** (1999) 127-137.
7. A. Cannavan, S. A. Hewitt, W. J. Blanchflower, D. G. Kennedy, *Analyst*., **121** (1996) 1457-1461.
8. B. Chiavarino, M. E. Crestoni, A. DiMarzio, S. Fornarini, *J. Chromatogr. B*., **706** (1998) 269- 277.
9. K. P. Bateman, S. J. Locke, D. A. Volmer, *Int. J. Mass Spectrom*., **32** (1997) 297-304.
10. N. Takeda, Y. Akiyama, *J. Chromatogr. A.*, **607** (1992) 31-35.
11. P. Vinas, C. L. Erroz, N. Campillo, M. H. Cordoba, *J. Chromatogr. A.,* **726** (1996) 125-131.
12. I.F. Abdullin, N.N. Chernysheva, G.K. Budnikov, *J. Anal. Chem*., **57** (2002) 629-631.
13. O.C. Braga, I. Campestrini, I.C. Vieira, A. Spinelli, *J. Braz. Chem. Soc*., **21** (2010) 813-820.
14. A. Preechaworapun, et al., *Talanta*., **68** (2006) 1726-1731.
15. S.M. Ghoreishi, M. Behpour, M. Delshad, A. Khoobi, *Cent. Eur. J. Chem*., **10** (2012) 1824-1829.
16. S.M. Ghoreishi, M. Behpour, A. Khoobi, *Anal. Methods*., **4** (2012) 2475-2485.
17. A.I. Stoica, C. Viñas, F. Teixidor, *Chem. Commun*.,**48** (2008) 6492-6494.
18. A.I. Stoica, C. Viñas, F. Teixidor, *Chem. Commun*., **33** (2009) 4988-4990.
19. A.I. Stoica, C. Kleber, C. Viñas, F. Teixidor, *Electrochim. Acta*., **113** (2013) 94-98.
20. J. Gallardo-Gonzalez, et al., *Sens. Actuators B*., **266** (2018) 823-829.
21. R. Bloch, A. Shatkay, H.A. Saroff, *Biophys. J*., **7** (1967) 865.
22. G.J. Moody, R.B. Oke, J.D.R. Thomas, *Analyst*, **95** (1970) 910-918.

23. Z. Stefanac, W. Simon, *Microchem. J.*, **12** (1967) 125-132.
24. N. Zine, et al., *Sens. Actuators B.*, **91** (2003) 76-82.
25. A. Saini, et al., *Sens. Actuators B.*, **268** (2018) 164-169.
26. B. E. H. Saxberg, B. R. Kowalski, *Anal. Chem.*, **51** (1979) 1031–1038.
27. Analytical chemistry division, commission on analytical nomenclature, Recommendations for nomenclature of ion-selective electrodes, Recommendations – 1975, *Pure Appl. Chem.*,**48** (1976), 127.
28. R. Buck, E. Lindner, Recommendations for nomenclature of ionselective electrodes (IUPAC Recommendations 1994), *Appl. Chem.*, **66** (1994) 2527-2536.
29. E.Bakker , E. Pretsch, P. Bühlmann, *Anal. Chem.*, **72** (2000), 1127–1133.
30. N. V. Belkova, L. M. Epstein, O. A. Filippoy, E. S. Shubina, *Chem. Rev.*, **116** (2016) 8545-8587.
31. R. Custelcean, J. E. Jackson, *Chem. Rev.*, **101** (2001) 1963-1980.
32. G. Chevrot, R. Schurhammer, G. Wipff, *J. Phys. Chem. B.*, **110** (2006) 9488- 9498.
33. C. Viñas, et al., *Dalton Trans.*, **43** (2014) 5062- 5068.
34. R. Fernandez-Alvarez, V. Ďorďovic,̌ M. Uchman, Matejǐcek, *Langmuir.*, **34** (2018) 3541- 3554.
35. E. Bakker, P. Buhlmann, E. Pretsch, *Chem. Rev.*, **97** (1997) 3083-3132.
36. A. Saini, et al., *J. Organomet. Chem.*, **893** (2019) 32-38.

3.3. Potentiometric Ion-Selective Electrode For Amphetamine Detection

The [Amphetamine-H]$^{+}$[Co($C_2B_9H_{11}$)$_2$]$^{-}$ ion pair complex was used to prepare a PVC matrix based selective microelectrode for detection of the illicit drug Amphetamine in wastewater. This micro- Ion Selective electrode gives low limit of detection and high selectivity for the detection of Amphetamine in wastewater.

Abhishek Saini
ICMAB-CSIC (UAB)

CONTENTS

3.3.1 Introduction

Amphetamine and Amphetamine type stimulants (ATS) are amongst the most abused illicit drugs with a European market of around 1.8 billion euros, amounting to consumption of around 76 tonnes of amphetamine annually.[1]

Amphetamine, (±)-1-phenylpropan-2-amine is among the oldest synthetic stimulant put into widespread production. It was first reported to have been synthesized in 1885 following the Leuckart method. [2-3] Following this method, certain ketones and aldehydes are converted to their corresponding amines by heating with excess of ammonium formate. [4] This synthesis procedure incorporates multiple steps, the first of which is the formation of N-formylamphetamine (NFA). This is done by a high temperature reaction between the precursor BMK and ammonium formate. BMK is also referred to as phenylacetone and it is an illicit drug whose production for commercial purposes is prohibited. The NFA is hydrolysed using HCl to form amphetamine chloride, which is then reacted with NaOH. This results in an oil-like liquid, which upon crystallization with H_2SO_4 leads to the formation of Ammonium Sulfate. Since the 1990s, this has been the most common method incorporated for the illegal synthesis of amphetamine. [5]

During this synthesis procedure, nearly 8.7 L of wastes is produced with water being the main component resulting from the water-vapour distillations performed at every step. However, for the purpose of detection of these illicit facilities, the most interesting waste produced is organic

waste, which amounts to between 0.7 and 0.8 L per kilogram of final product. This organic waste contains BMK, NFA and Amphetamine, which can be detected. [6-9]

The amount of amphetamine and ATS producing facilities are on the rise despite the efforts of European Police Agencies. Most of those illegal facilities are sited in Eastern Europe with most of the manufacturing done in medium to large, sometimes industrial sized facilities. [10] As mentioned, the synthetic procedure of these ATS produces a large amount of liquid waste, it is estimated that for every 1 kg of Amphetamine sulphate produced, 8 litres of liquid waste is generated. [11-12] This liquid waste is often disposed off in nearby sewage systems, making it possible to pinpoint the location of an ATS producing facility by detecting the presence of Amphetamine and its precursors in wastewater. The presence of these specific markers in wastewater of a particular region would make it easier to narrow down the location of an ATS producing facility.

Ex-situ analytical techniques are the most common for the detection of amphetamine and its derivatives in wastewater samples. These ex-situ techniques include colorimetric measurements, capillary electrophoresis and chromatographic analyses coupled with mass spectrometry techniques. [13–15] SPE with HPLC-MS/MS have also been used recently to some success. [16] However, these aforementioned methods suffer from drawbacks such as being complex, methodical, slow response time and need of trained personnel to constantly handle them, thus invariably increasing their cost.

To overcome these drawbacks, chemical sensors have been proposed as a viable alternative, owing to their nature as inexpensive and easy to handle devices for obtaining real time data. The most often used strategy involves the development of active sites that enhance Amphetamine and ATS interactions with cyclodextrins, enzymes, nanotubes etc, to improve performance of current detection techniques. [17-20]

Ion Selective Electrodes (ISEs) have been reported in literature using crown ethers dibenzo-18-crown-6 and dibenzo-24-crown-8 for Amphetamine capture. [21-22] Although ISEs have great advantages such as fast response time and ease of use, they also suffer from the drawback of being selective towards structurally similar compounds to the target molecule. The aforementioned ISEs while showing low limit of detection and a respectable response time were found to be not very selective towards amphetamine. As explained in previous chapters, the use of Ion-pair complex comprising of the target molecule and the $[3,3\text{-}Co(1,2\text{-}C_2B_9H_{11})_2]^-$ anion does away with the problem of low selectivity, leading to ISEs with low limit of detection, low response time and very high selectivity.

In this work, a potentiometric ISE with the $[Amphetamine]^+$ $[3,3\text{-}Co(1,2\text{-}C_2B_9H_{11})_2]^-$ ion pair complex was developed for the real time and fast detection of amphetamine in wastewater. The reasons for using $[3,3\text{-}Co(1,2\text{-}C_2B_9H_{11})_2]^-$ for this purpose have already been explained in detail in previous chapters.

This work was done in collaboration with the group of Prof. Abdelhamid Errachid, in association with Dr. Juan Gallardo-Gonzalez at Institut des Sciences Analytiques, UMR 5280, Villeurbanne, France. Since the importance of the ion pair complex, conductive polymer layer growth, plasticizers, response time, pH response and selectivity and the concepts behind them have already been explained in previous chapters in detail, they have not been elaborated upon here. Only the results of the characteristic response parameters while using the ISE for detection of amphetamine are presented here.

3.3.2 Microelectrode Preparation and Ion Pair Complex formation

3.3.2.1 Ion Pair Complex Formation

The ion-pair complex $[C_9H_{13}NH]^+[3,3'\text{-}Co(1,2\text{-}closo\text{-}C_2B_9H_{11})_2]^-$ has been obtained by ion-exchange procedure. $Cs[3,3'\text{-}Co(1,2\text{-}C_2B_9H_{11})_2]$ (300 mg, 0.657 mmol) was extracted with H_2SO_4 1M (15 mL) and diethyl ether (20 mL). The organic layer was shaken three times with H_2SO_4 1M (15 mL 3×). Then, the diethyl ether was evaporated and the residue was diluted with water to generate 0.05 M solution of $H[3,3'\text{-}Co(1,2\text{-}C_2B_9H_{11})_2]$ (solution 1). Amphetamine sulfate was dissolved in water and with the minimum quantity of H_2SO_4 1M to prepare 0.05 M acidic solution (solution 2). Next, 20 mL of solution 1 and 20 mL of solution 2 were mixed and after stirring a yellow precipitate was obtained. This was filtered off, washed with H_2SO_4 0.1 M and dried under vacuum.

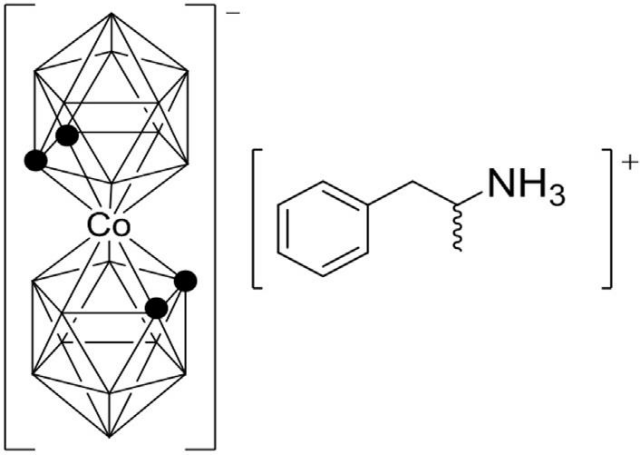

Figure. 1. Ion pair Complex: Chemical structure of the 3,3′-[Co(1,2-closo-$C_2B_9H_{11})_2$]·[Amphetamine]$^+$ ion pair complex.

The ^{1}H- and ^{1}H{^{11}B}-NMR (300.13 MHz), ^{13}C{1H}-NMR (75.47 MHz) and ^{11}B- and ^{11}B{1H}-NMR (96.29 MHz) spectra were recorded on a Bruker ARX 300 instrument equipped with the appropriate decoupling accessories. All NMR spectra were performed in acetone deuterated solvent at 22^{o}C. The ^{11}B- and ^{11}B{1H}-NMR shifts were referenced to external BF3·OEt2, while the ^{1}H, ^{1}H{^{11}B}, and ^{13}C{^{1}H}- NMR shifts were referenced to SiMe4. Chemical shifts are reported in units of parts per million downfield from reference, and all coupling constants in Hz.

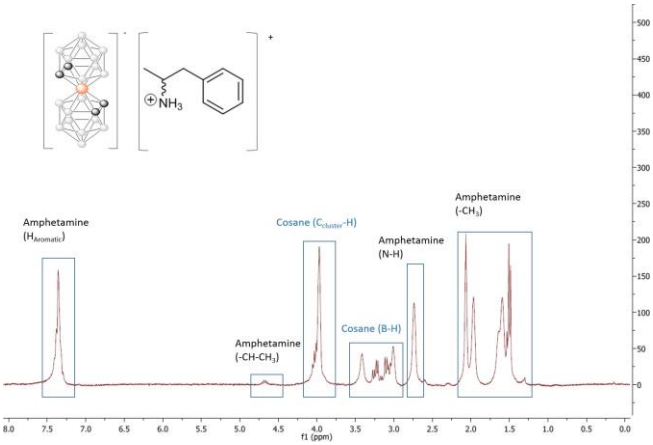

Figure 2. ^{1}H-NMR of the Amphetamine-[Co($C_2B_9H_{11}$)$_2$] Ion pair complex.

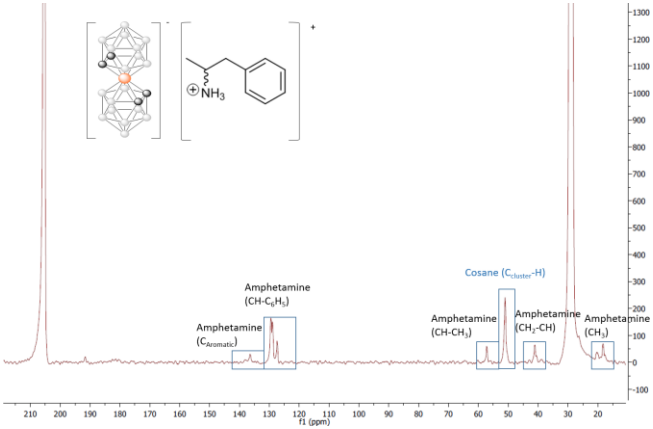

Figure 3. ^{13}C-NMR of the Amphetamine--[Co($C_2B_9H_{11}$)$_2$] Ion pair complex.

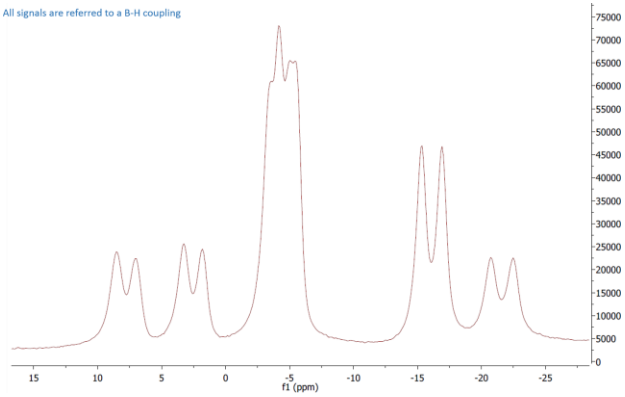

Figure 4. ^{11}B- NMR of Amphetamine-[Co($C_2B_9H_{11}$)$_2$] Ion pair complex.

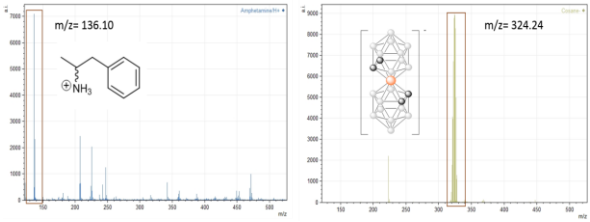

Figure 5. MALDI-TOF spectra of Amphetamine-[Co($C_2B_9H_{11}$)$_2$] Ion pair complex.

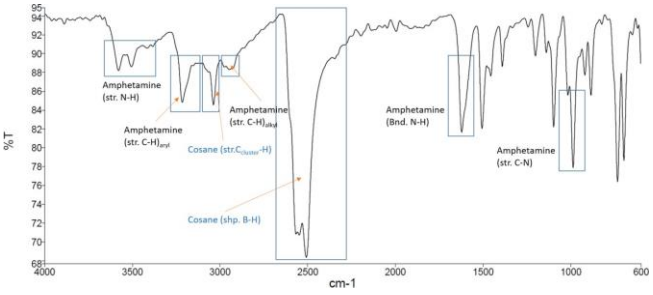

Figure 6. FTIR of the Amphetamine-[Co($C_2B_9H_{11}$)$_2$] Ion pair complex.

3.3.2.2 Microelectrode Preparation and Conductive Polymer layer growth

Electrochemical Impedance Spectroscopy (EIS) and Cyclic Voltammetry (CV) were used for electrode characterization and electrochemical polymerization of the polypyrrole conductive layer. The microelectrode fabrication process and the subsequent growth of the conductive Polypyrrole [$Co(C_2B_9H_{11})_2$] layer has already been described in previous chapters. The polymeric membrane is able to establish full contact between the sensing membrane and the electrode due to the porous polypyrrole layer which leads to an enhanced lifetime for the sensors. A gold microelectrode having the following dimensions: Working Electrode area 0.64 mm^2, Reference Electrode Area 0.13 mm^2 and Auxilary Counter Electrode area 1.37 mm^2, having 4 gold Working Electrodes, one gold Counter Electrode and 2 Ag/AgCl Reference electrodes was chosen for the fabrication of the Ion selective Electrode as these dimensions were found to give the most intense signal among microelectrodes of different dimensions tested.

A solid contact layer of conductive polymer, Polypyrrole[3,3′-$Co(1,2\text{-}C_2B_9H_{11})_2$] was galvanostatically grown by electrochemical polymerization onto gold microelectrodes. The solution was made of 0.035 M of Cs[3,3′-$Co(1,2\text{-}C_2B_9H_{11})_2$] and 0.1 M of pyrrole in acetonitrile 1 wt.% in water. The electrochemical polymerization of pyrrole doped with [3,3′-$Co(1,2\text{-}C_2B_9H_{11})_2]^-$ anion was carried out by applying 5 potential sweep cycles between -0.6V and 1.2V, at scan rate of 100

mV/s by means of cyclic voltammetry (CV). After polymerization, the microelectrodes were rinsed with deionised water and dried under nitrogen flow.

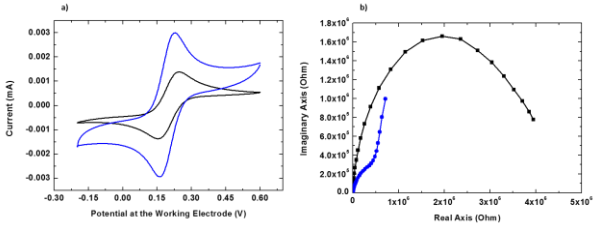

Figure 7. a) Cyclic voltammogram of gold microelectrode in redox probe $K_3[Fe(CN)_6]/K_4[Fe(CN)_6]$ 5mM in phosphate buffer solution. Potential scanned from -0.2 to 0.6 V vs SCE at scan rate of 100mV/s. In black: bare gold microelectrode. In blue: gold microelectrode after electrochemical polymerization of Polypyrrole[3,3′-Co(1,2-$C_2B_9H_{11})_2$] conductive layer. **b)** . Nyquist diagram of gold microelectrode in redox probe $K_3[Fe(CN)_6]/K_4[Fe(CN)_6]$ 5mM in phosphate buffer solution. Potential applied, E vs SCE = -0.2 V, frequencies scanned from 200 KHz to 100 mHz. Sinus amplitude = 75 mV. In black: bare gold microelectrode. In blue: gold microelectrode after electrochemical polymerization of Polypyrrole[3,3′-Co(1,2-$C_2B_9H_{11})_2$] conductive layer.

As is clear from **Fig. 7**, there's a marked increase in the redox peak of the cyclic voltammogram after deposition of the Polypyrrole[3,3′-Co(1,2-$C_2B_9H_{11})_2$] conducting layer. This implies an enhancement in the electric charge transfer properties of the electrode. This is further confirmed by the Nyquist plot showing a decrease of the electrochemical impedance.

The microelectrode fabrication and preparation procedure has already been explained in detail in Section 3.1. **Fig. 8** depicts the different stages of the microelectrode preparation.

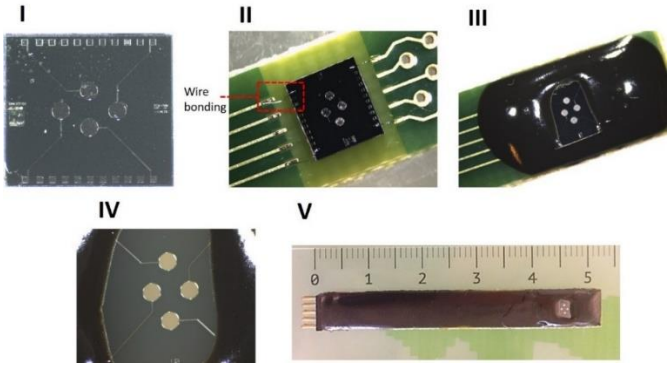

Figure 8. I) Transducer with four bare Pt microelectrodes. **II)** the transducer was wire-bonded to a PCB. **III**) the electrical connections have been isolated using an epoxy resin. **IV**) bare Pt microelectrodes after cleaning procedure. **V**) final device.

3.3.2.3 Polymeric Membrane Preparation

The membrane to be deposited on top of the microelectrode consists of the following components-

a) Polymeric matrix
b) Plasticizer
c) Ion Pair complex

Contrary to the ISEs described in the previous chapters, for this particular ISE for potentiometric detection of Amphetamine, the composition that gave the best results was found to be - 31 wt.% PVC, 65 wt.% plasticizer and 4 wt.% ion pair-complex. PVC was used as the polymeric matrix and in this case, 4 plasticizers were used namely, di-butyl phthalate (DBP), di-octyl phthalate (DOP), Bis (2-ethyl hexyl) Sebacate (DOS) and o-nitrophenyloctyl ether

(o-NPOE). 4 different ISEs were prepared each with a different plasticizer.

The ion-pair complex plays the role of both the ionophore and ion-exchanger when added to the polymeric membrane and is largely responsible for its impressive performances.

The ion-pair complex gets dissociated into $[C_9H_{13}NH]^+$ and $[3,3'\text{-}Co(1,2\text{-}C_2B_9H_{11})_2]^-$ in the membrane phase, due to its high hydrophobicity. The impurities left over from the ion pair complex synthesis are in the form of $H[3,3'\text{-}Co(1,2\text{-}C_2B_9H_{11})_2]$ which spread in the lipophilic membrane due to which, the former dissociation pair serves as amphetamine-ionophore when a gradient of concentration at the interface membrane/solution is created. The latter dissociation pair plays the role of a bulky ion-exchanger to prevent the anions from interacting with the membrane. It also supports the ionic flux through the interface membrane/solution and across the lipophilic membrane thus enhancing the performance of the sensor and also increasing its lifetime.

All of these components were dissolved in 1.5 mL of Tetrahydrofuran (THF) and deposited directly on top of the electroactive area of the microelectrode and left overnight to dry.

3.3.2.4 Potentiometric Measurement

All measurements were carried out at room temperature using a multichannel homemade-data-acquisition system setup with four microelectrodes connected at the same time and controlled by a personal computer.

Measurements were made relative to an Ag/AgCl reference microelectrode integrated in the transducer and under magnetic stirring. Since potentiometric measurements are commonly carried out under the zero current conditions, there is no need to connect the counter electrode and hence, it can be functionalized as Reference Electrode, hence allowing the simultaneous measurement of four Working Electrodes using only one Reference Electrode.

The Counter Electrode was transformed into Ag/AgCl pseudo-Reference Electrode in-situ by an electrochemical reduction of a solution made of $NaNO_3$ 1M and $AgNO_3$ 25mM at pH 1 by Cyclic Voltammetry. The potential was scanned from -0.5 and 0.3 V at scan rate of 50 mV/s for 16 s. The Working Electrode with the conducting polymer layer and the polymeric membrane is shown in **Fig. 9**. The apparatus used for performing the measurements is the same as depicted in Section 3.1.

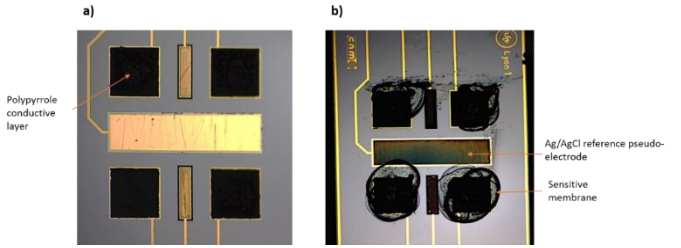

Figure 9. (a) WEs electrochemically modified with Polypyrrole[3,3′-Co(1,2-$C_2B_9H_{11}$)$_2$] solid conductive layer. **(b)** The polymeric membrane including the ion-pair complex[$C_9H_{13}NH$]$^+$[3,3′-Co(1,2-closo-$C_2B_9H_{11}$)$_2$]$^-$ drop cast on the top of the WEs.

Amphetamine solutions with a concentration range of 10^{-5}M to 10^{-1}M were prepared to obtain the calibration curves. Successive aliquots of these solutions were added to 25 ml of distilled water for the potentiometric measurements. The measurements were made between the concentration range of 10^{-7} to 10^{-3} M, following the Generalized Standard Addition Method [23].

The Debye-Huckel equation is used in an aqueous solution for the measurement of the activity of an organic cation. This activity was reflected by the potential variations recorded whose value was plotted as a logarithmic function of Amphetamine activity.

3.3.3Response Characteristics

3.3.3.1 Potentiometric Response

The 4 ISEs, each with a different plasticizer were calibrated using the GSAM. As can be seen from Table 1, the ISE with DOP gave the lowest limit of detection, but its slope is not near the Nernstian slope limit of 59, so the ISE with the best overall response was the ISE with DBP as the plasticizer.

Plasticizer	Slope (mV/decade)	Detection Limit (mol/dm^3)	Response Time (s)	Lifetime
DBP	60	1 x 10^{-5}	<10	5 months
DOP	42	8 x 10^{-6}	<10	Not tested
DOS	53	4 x 10^{-5}	<10	Not tested
NPOE	45	2 x 10^{-5}	<10	Not tested

Table 1. Response Characteristics of the ISE elaborated. Slope, detection limit, time response and lifetime of different plasticizers for the detection of Amphetamine.

Fig. 10 represents the potentiometric response of the 4 ISEs, each with a different plasticizer. From Table 1 and **Fig. 10** we can conclude that the ISE with DBP as the plasticizer gives the best response and hence, was chosen for further studies regarding selectivity, lifetime and pH response.

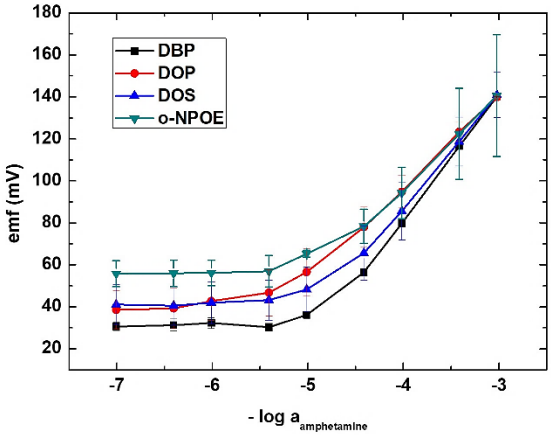

Figure 10. ISE response: Potentiometric response of Amphetamine selective ISEs with different plasticizers in the membrane.

3.3.3.2 Selectivity

As already elaborated upon previously, selectivity of an ISE is an extremely important parameter with regards to its real-life usage. The use of the $[Co(C_2B_9H_{11})_2]^-$ anion and incorporating the target molecule in the ion pair complex is what makes the polymeric membrane extremely sensitive only to the target molecule.

To test the selectivity of the ISE three molecules structurally similar to Amphetamine were studied as possible interferences. N-formyl amphetamine, an intermediary compound formed during the synthesis of Amphetamine [24] whose presence in wastewater can only be attributed to nearby illicit amphetamine laboratories, was chosen as one of the interferences . Methylbenzylamine and phenylalanine were the other two molecules chosen as interferences, owing to their structural similarity to amphetamine.

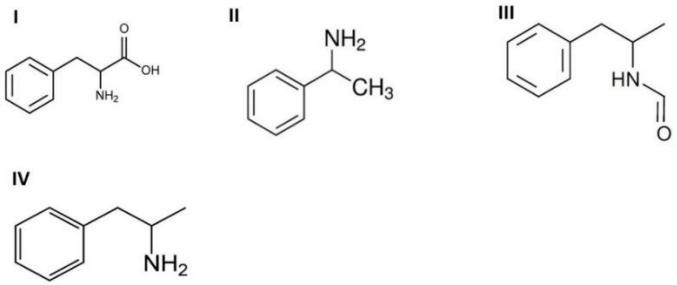

Figure 11. Chemical structures of i) Phenylaniline ii) Methylbenzylamine iii) N- formyl Amphetamine iv) Amphetamine.

The Nikolsky Eisenman equation was used to determine the potentiometric selectivity coefficient, $K_{A,Bpot}$. [25-26] The Fixed Interference Method (FIM) was employed to

determine this potentiometric selectivity coefficient. This method involves measuring solutions of constant activity, in this case having concentration 10^{-3} mol/dm^3 of the interfering ion while varying the activity of Amphetamine from 10^{-7} to 10^{-3} mol/dm^3.The electrochemical cell used was based on a reference and a working electrode immersed in 25 ml of 1mM solution of an interference. The response of Amphetamine in the presence of interferences was compared to the response of ISE in water.

To calculate the $K_{A,Bpot}$, the EMF values obtained are plotted vs the logarithm of the activity of the analyte. From this plot, the value of the $K_{A,Bpot}$ was extrapolated at the intersection points of the linear portions of the plot. From this intersection point the $K_{A,Bpot}$ value is calculated using the Nikolsky Eisenmann equation. [27] The results obtained from the potentiometric selectivity coefficient measurements are presented in Table 2.

Name of Interference	**log $K_{A,BPot}$**
N-formyl Amphetamine	-2.15
Phenylaniline	-2.09
Mehtylbenzylamine	-2.09

Table 2. Selectivity of ISE against interfering compounds**.**

As evidenced from Table 2, the ISE was at least 2 orders of magnitude more selective towards Amphetamine than any of the tested interferences.

3.3.3.3 Lifetime

The ISE was tested over a period of 5 months to gauge its stable lifetime. It was used multiple times on an at least weekly basis during this time period. The Amphetamine

selective ISE showed only a slight change in performance over the period of 5 months, as can be seen from **Fig. 12.** The decrease in a sensor's sensitivity over time can be attributed to the exudation of the ionophore from the polymeric membrane. The more the ionophore is chemically stable inside the membrane the less the ionophore bleeds from this latter. The role of the $[Co(C_2B_9H_{11})_2]^-$ anion and especially its ability to form $C_{cluster}$-H···H-B dihydrogen bonds in increasing the lifetime of an ISE has already been explained in the previous chapter.

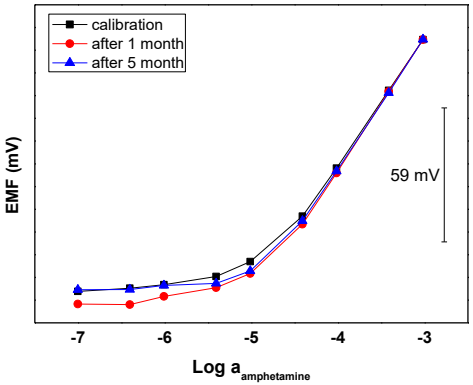

Figure 12. Lifetime of ISE: Potentiometric response of Amphetamine selective μISE over different time periods with Dibutyl Phthalte as plasticizer.

3.3.3.4 Response Time

The response time is the time taken by the electrode to achieve a stable potential and in this study, like the ISEs described in previous chapters, it was found to be less than 10 seconds in all cases (**Fig. 13**), hence making this

ISE a practical tool for real time detection of Amphetamine.

The optimal thickness of the polymeric membrane and conducting polymer layer PPy[Co($C_2B_9H_{11}$)$_2$] is essential for obtaining a quick response time.

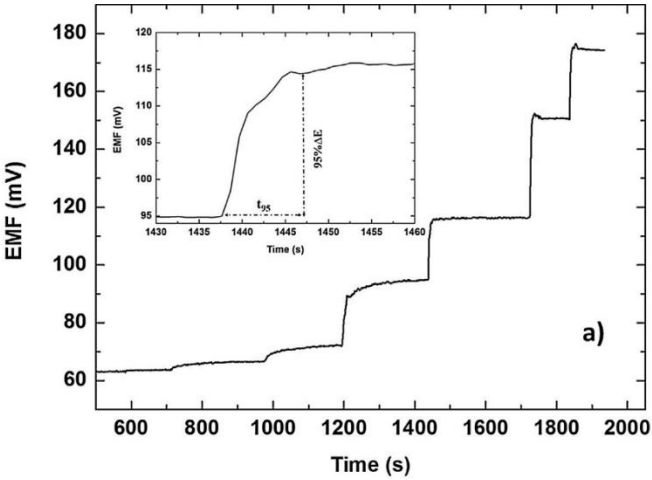

Figure 13. Dynamic response of one of the amphetamine-selective ISE for step changes in the concentration of amphetamine sulfate.

3.3.3.5 pH Response

To test the stable pH range of the ISE, the emf variation was followed over a pH range between 1.50 and 12.5 in 25 ml of a 1 mM acidic solution of amphetamine sulphate. The pH of the solution was increased by small additions of NaOH 1 M solution. The ISE was found to have a stable response in the pH range of 1.5 to 8.5. (**Fig. 14**) Since, this ISE is designed for use in water, which has a pH around 7, this working pH range was appropriate.

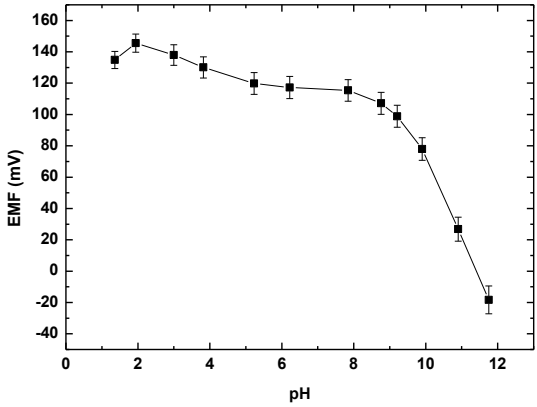

Figure 14. pH response: Reilley diagram showing the effect of pH variation on the EMF of the Amphetamine selective ISE. The μISE gives a stable EMF signal between pH 1.5 and 8.5. The pH working range is measured by increasing the pH of a 1 mM solution of Amphetamine sulfate by titration with small aliquots of NaOH 1 M solution.

3.3.3.6 Comparison with other potentiometric Amphetamine Sensors

The Amphetamine selective micro-ISE described here was compared with other potentiometric sensors for Amphetamine described in literature.

Sensor 1- Amphetamine selective ion pair complex based micro-ISE described in this work.

Sensor 2- αCyclodextrins-based amphetamine sensor. [17]

Sensor 3- Dibenzo-18-crown 6-ether amphetamine sensor (liquid membrane macrosensor). [21]

Sensor 4- Dibenzo-24-crown 8-ether amphetamine sensor (liquid membrane macrosensor). [21]

Sensor 5- Dibenzo-18-crown 6-ether-based Amphetamine microsensor. [22]

Response Parameter	Sensor 1	Sensor 2	Sensor 3	Sensor 4	Sensor 5
Slope (mV/decade)	60.1	50	58	55	53
Lowest limit of detection (mol/dm^3)	1×10^{-5}	2.5×10^{-4}	8×10^{-6}	3×10^{-5}	4×10^{-5}
pH range	1.5-8.5	N. A	3-7	3.5-6.5	1.5-8.5
Response time (s)	<10	N. A	30-60	30-60	12-16

Table 3. Response Parameter of Amphetamine selective micro-ISE described in this work with other potentiometric Amphetamine sensors.

As is clear from Table 3, the ISE described here gives a lower limit of detection than all the amphetamine sensors in literature, except the Dibenzo-18-crown 6-ether amphetamine sensor. But the Amphetamine selective micro-ISE has a faster response time and is a microsensor, unlike the Dibenzo-18-crown 6-ether amphetamine sensor, which is a microsensor and hence cannot be used for real time applicative purposes. Thus, it is clear that the Ion-Pair complex based Amphetamine selective micro-ISE described in this work is a clear step forward from all the existing sensors for real time detection of Amphetamine.

All the results and figures presented here have been published in Sensors and Actuators B: Chemical. [28]

3.3.4 Conclusions

An all solid state and highly selective microsensor for the detection of the illicit drug Amphetamine has been described in this work. This potentiometric Ion Selective Electrode is based on an ion-pair complex of $[C_9H_{13}NH]^+[3,3'\text{-}Co(1,2\text{-}closo\text{-}C_2B_9H_{11})_2]^-$. This ion pair complex acts as the active part of the PVC enforced polymeric membrane for the amphetamine detection. The composition of the polymeric membrane that gave the best result was found to be 31 wt.% of PVC, 65 wt. % of DBP (Plasticizer) and 4 wt. % of the ion-pair complex. The micro-ISE produced showed an almost perfect Nernstian slope with a lowest limit of detection of 1×10^{-5} mol/dm^3 and a pH working range of 1.5 to 8.5. The micro-ISE was also highly selective towards Amphetamine, found to be at least 100 times more selective towards Amphetamine than structurally similar compounds.

3.3.5 References

1. European Monitoring Centre for Drugs and Drug Addiction and Europol, EU Drug Markets Report. In-depth Analysis, EMCDDA – Europol Joint publications, Publications Office of the European Union, Luxembourg, 2016.
2. R. Adams et al., Organic Reactions, 1949.
3. M. Nevešćanin, S.B. Stević, S. Petrović, V. Vajs, *J. Serbian Chem. Soc.* **73** (2008) 691–701.
4. R. Leuckart, *Chem. Gesellschaft*. **154** (1885) 72–75.
5. M. Bohn, G. Bohn, G. Blaschke, *Int. J. Legal Med*. **106** (1993) 19–23.
6. F. Palhol, S. Boyer, N. Naulet, M. Chabrillat, *Anal. Bioanal. Chem.* 374 (2002) 274–281.
7. D. Blachut, K. Wojtasiewicz, Z. Czarnocki, *Forensic Sci. Int.* **127** (2002) 45–62.
8. V. Kunalan, N.N. Daéid, W.J. Kerr, H.A.S. Buchanan, A.R. McPherson, *Anal. Chem*. **81** (2009) 7342–7348.
9. M. Lambrechts, K.E. Rasmussen, *Bull. Narc.* **36** (1984) 47–57.
10. EMCDDA, EMCDDA – Europol joint publications: Amphetamine (2011) doi:10.2810/49525.
11. T. Hague, Amphetamine-Type Stimulants in the European Union 1998-2007 (2007).
12. EMCDDA, Wastewater analysis and drugs: a European multi-city study, (2016) 1–5.
13. Z. Xu, et al., *Sci. Total Environ*. **601-602** (2017) 159–166.
14. I. Senta, I. Krizman, M. Ahel, S. Terzic, Multiresidual, *J. Chromatogr. A* **1425** (2015) 204–212.
15. T.H. Boles, M.J.M. Wells, *Electrophoresis* 37 (2016) 3101–3108.
16. E. Zuccato, et al., *Drug Alcohol Depend*. **178** (2017) 285–290.
17. R. Kataky, D. Parker, P.M. Kelly, *Scand. J. Clin. Lab. Invest.* **55** (1995) 409–419.
18. M.A.C. Fresqui, M.M.C. Ferreira, M. Trsic, *Anal. Chim. Acta* **759** (2013) 43–52.
19. H. Hafizi, A. Najafi Chermahini, G. Mohammadnezhad, A. Teimouri, *Appl. Surf. Sci.* **329** (2015) 87–93.
20. S. Bashiri, E. Vessally, A. Bekhradnia, A. Hosseinian, L. Edjlali, *Vacuum* **136** (2017) 156–162.
21. S.S.M. Hasan, E.M. Elnemma, *Anal. Chem*. **61** (1989) 2189–2192.
22. J. Gallardo-González, et al., *Anal. Lett.* **58** (2018) 348–358.

23. B. E. H. Saxberg, B. R. Kowalski, *Anal. Chem*., **51** (1979) 1031–1038.
24. K. Graniczkowska, M. Pütz, F.M. Hauser, S. De Saeger, N.V. Beloglazova, *Biosens. Bioelectron.* **92** (2016) 741–747.
25. Analytical chemistry division, Commission on analytical nomenclature, recommendations for nomenclature of ion-selective electrodes, Recommendations – 1975, *Pure Appl. Chem.*,**48** (1976), 127.
26. R. Buck, E. Lindner, Recommendations for nomenclature of ionselective electrodes (IUPAC Recommendations 1994), *Appl. Chem.*, **66** (1994), 2527-2536.
27. E.Bakker , E. Pretsch, P. Bühlmann, *Anal. Chem*., **72** (2000), 1127–1133.
28. J. Gallardo-Gonzalez et al., *Sens. Actuators. B.*, **266** (2018) 823-829.

3. Results and Discussions Part 2 (Carboranyl Ligands as Capping agents for Innovative Nanostructures)

3.4. Spherical Carboranyl ligands to tune morphologies of colloidal Quantum Nanocrystals

Spherical carboranyl derivatives were used as capping agents to synthesize CdSe Quantum Nanocrystals of varying morphologies, having high intensity of PL emission and long lifetime, in a colloidal synthesis.

Abhishek Saini
ICMAB-CSIC (UAB)

CONTENTS

3.4.1 Introduction

3.4.1.1 Quantum Dots

Quantum Dots (QDs) are miniscule crystals of a semiconductor material having from a near hundred to a few thousand atoms. Due to their small size they behave like discreet electronic states [1] which makes them easily tuneable by simply modifying the size of the QDs. [2] This is due to the Quantum confinement affect explained in the Introductory chapter. Due to this property as well as their high excitation coefficient and photobleaching stability, they have found applications in fields such as solar light harvesting [3], Light Emitting Diodes [4], Low cost thin film transistors [5], Lasers [6], Bio Imaging [7], Chemo-sensing [8], Photocatalysis [9] among many others. [10-12]

The most common methods for synthesis of QDs are physical methods or chemical colloidal routes. [13] Using colloidal methods, they are mostly synthesized using a high-temperature hot-injection organic method. [14-15] For organic synthesis, 1-Octadence is the most prevalent amongst the solvents used due to its high boiling point.

The core of the QDs are usually composed of elements belonging to either II-VI or III-V group. It also consists of a shell which is usually another semiconductor of wide bandgap. [16] This shell layer is necessary to improve the quantum yield (QY). [17] This core-shell of the QD is encapsulated (or capped) with a ligand. This ligand is necessary so to limit the growth of the QD and ensuring its size remains within a dimension in which they can display its exceptional properties. [18] They prevent growth in size of the QD and also prevent formation of

aggregates thus ensuring the QD stays within the required dimension. Cadmium Chalcogenides CdX (X= Se, S or Te) QDs grab special attention due to their emission spectrum that spreads over the entire visible region. [19-20]

3.4.1.2 Quantum Rods

Quantum Rods (QR_{ods}) are a 1-D morphology distinct from the more studied QDs. They are of great interest too due to their elongated lengths providing a number of advantages over the traditional QDs. Similar to QDs, QR_{ods} are semiconductor materials too but with diameters in the range of 2 to 10 nm and lengths of about 10-200 nm, with the diameter sizes responsible for the band gap. [21] QR_{ods} are highly sought after as they not only possess all the advantageous properties of QDs due to boasting a tunable diameter, but also have a large number of unique properties of their own such as a bigger Stokes Shift, [22] faster radiative decay rate [23] and larger absorption cross section. [24] A big difference between the QDs and QR_{ods} is in their emission properties. While the QDs emit plane-polarized light, QR_{ods} emit linearly polarized light [25] and the emission of single QR_{ods} can be reversibly switched on-off by external electric fields. [26] These unique properties make QR_{ods} highly desirable in the field of various applications like fluorescent labels and markers. [27] The reason that QR_{ods} aren't as commercially used as QDs is due to a lack of efficient synthesis methods. When synthesised using physical methods of preparation, the throughput is very low to be used for synthesis of learge quantities. To overcome this, colloidal methods for the synthesis of QR_{ods} have been reported, where they are

synthesized by TOPO oxidation in hot injection synthesis [28-29] and by controlled seeded synthesis. [30]

3.4.1.3 Quantum Rings

Quantum Rings (QRs) are unique two-dimensional nanostructures. Their circular geometry sets them apart from QDs and QRods. Quantum Rings reported in literature such as InGaAs show an outer diameter between 60 and 140 nm, a height of about 2 nm and a centre hole of about 20 nm in diameter.[31] QRs are perhaps the least studied amongst Quantum Nanostructure (QNCs) due to difficulties in synthesizing them and there is a lot of fascination regarding their unique properties. [32] QRs provide the unique opportunity to study theoretical phenomenon such as magnetic flux bear persistent (dissipation less) circulating electron currents, oscillation in magnetization, Stark effect and Aharanov-Bohm Oscillations. [33-38] To be able to study these phenomena in depth, efficient methods to produce QRs are necessary. QRs have generally been produced by physical methods using electron beam lithography, and ion beam milling. Presently, the most frequently used procedure for their synthesis is the lattice-mismatched technique by the Stranski–Krastanov (S-K) model. [39-42] An alternative to this technique is the Droplet epitaxy (DE) method developed by Koguchi and his coworkers. [43-44] Both of the aforementioned techniques are based on epitaxially grown monolayers and rely on lattice mismatch induced strains. These techniques are fully compatible with Molecular Beam Epitaxy technology. For both the S-K and the DE methods,

the morphology of the nanostructures produced is determined by the interplay between deposit, desorption, and surface diffusion. But these methods of preparation suffer from the drawback of having very low throughput, hence making production of an appreciable quantity of QRs difficult. Talapin et al, reported a colloidal synthetic method for synthesis of QRs, albeit one that requires etching. [45] This represented a leap forward in synthetic methods for production of these QRs and opened the doors for further colloidal synthetic methods for synthesis of QRs.

The aim of the work presented in this chapter was the synthesis of CdSe QDs, QR_{ods} and QRs using a colloidal synthetic method. Since this has never been reported before in literature, the decision was made to use unconventional spherical carboranyl ligands to act as capping agent.

3.4.1.4 Importance of Carboranyl Ligands

As mentioned above, the fact that the size of QDs is dependent on the capping agent is well established in literature. There have also been works emphasising the importance of ligands for shape and size control of QRs and QR_{ods}. [46] Carboranyl ligands have been used previously as capping agents for gold nanoparticles with phase transfer properties [47] and aqueous QDs which showed the previously unreported phenomenon of Kinetic Fluorescence Switching. [48] These unique properties obtained by using carboranyl ligands as capping agents provided the motivation to attempt to use these unique spherical ligands as capping agents for the

synthesis of different morphologies of Quantum Nanocrystals (QNCs). These carboranyl ligands are spheres having an appended coordinating site. The reason for this being that spheres can ideally pack in a compact way with a hexagonal or square arrangement, thus influencing the inner core by the outer sphere packing. These carboranyl ligands are more readily available than the geometrically similar hydrocarbon dodecahedrane ($C_{20}H_{20}$) which is very difficult to synthesize. [49] The hydrophobicity of the spheres can be tuned by choosing the nature of the (car)borane. The linkage between the spheres and the CdSe core is through a coordinating site with a negative charge, $–S^-$, $–PH(O)O^-$. As we intended to facilitate dissolution in high boiling low polar solvents, we decided to use the neutral carboranes, owing to their lipophilicity. Carboranes have geometrical figures that correspond to deltahedra having atoms only in the periphery; the more stable are those with closed structures, and among these the most stable is the icosahedron. [50-51] They can resist harsh conditions, can be exposed to air for years and have a varied derivative chemistry. [52] In short, they are very attractive to be used in material's science, particularly by the monolayer mode of packing when placed on a surface, either hexagonal or square.

Seven different carboranyl ligands were used during the course of this work, namely *meta*-carboranethiol [53], *ortho*-carboranethiol [53], *meta*-carboranedithiol [53], 1-methyl-*ortho*-2-carboranethiol [53], *meta*-carboranephosphinic acid [54], *meta*-carboranediphosphinic acid [54] and *meta*-

carboranecarboxylic acid. [55] These ligands have been described in more detail in the introductory chapter and are represented here in **Fig**. 1.

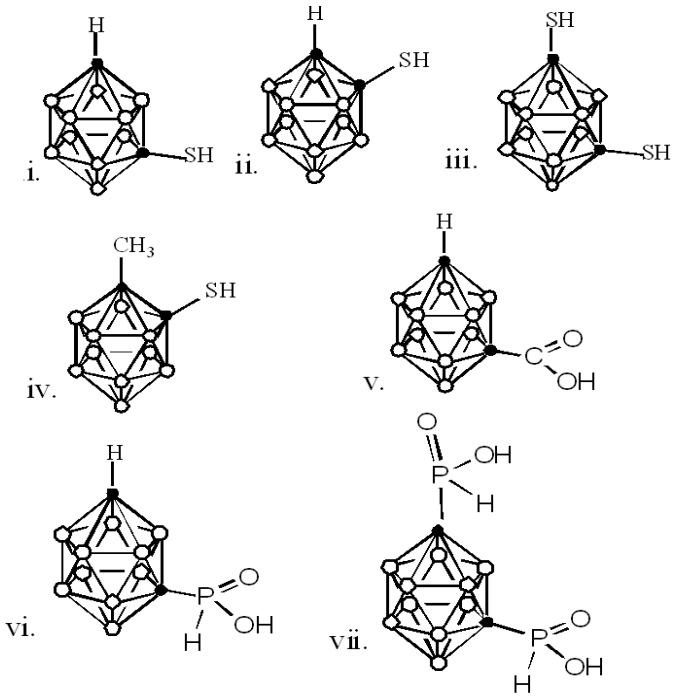

Figure 1. The ligand structures of (i) *meta*-carboranethiol, (ii) *ortho*-carboranethiol, (iii) *meta*-carboranedithiol (iv) 1-methyl-*ortho*-2-carboranethiol, (v) *meta*-carboranylcarboxylic acid, (vi) *meta*-carboranephosphinic acid and (vii) *meta*-carboranediphosphinic acid are shown here. The circles refer to B-H units while the black circles refer to Carbon units.

The advantage of using spherical ligands over straight chain ligands is that the compact arrangement of these spheres leads to curvatures. These curvatures are caused due to bending of these spheres which leads to creation of

a wide variety of geometrical figures. This concept is visually depicted in **Fig**. **2**.

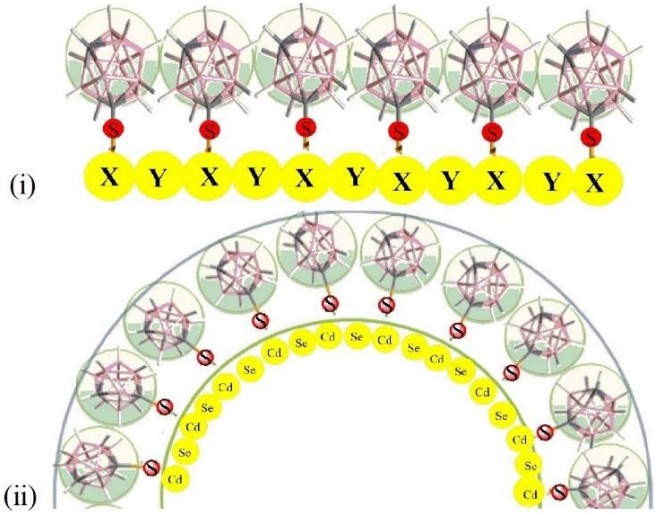

Figure 2. The Schematic of the sphere concept for different geometries. (i) Case for an ideal matching between the diameter of the sphere and the diameter of the X-Y unit. (ii) Case for a mismatch, as is the case of the carborane diameter and the CdSe covalent diameter.

The straight scheme in Fig. 2(i) depicts a perfect matching of the sphere Van der Waal's diameter and the covalent diameter of the Cd-Se. However, in reality this matching is not perfect as depicted, the two diameters being 656 pm vs 528 pm respectively, a mismatch of 24%. The only way for them to fit with each other would be through the model shown in Fig. 2(ii), i.e., the two concentric circles. This mismatch is the framework upon which the idea to produce curved structures like QRs and QR_{ods} was generated.

The aforementioned carboranyl ligands were used as capping agents to synthesise different CdSe QNCs. All of the ligands gave a different morphology as detailed below.

3.4.2 Experimental Procedure

3.4.2.1 Synthesis of Carboranyl Ligands

Ortho-carboranethiol was synthesized using the method developed by Vinas and co. as follows-

7 mmol (1 g) of 1,2-$C_2B_{10}H_{12}$ was dissolved in 25ml of dry TetraHydroFuran at 0 °C. 7.04 mmol of n- butyllithium was added to this solution and the suspension was stirred at this temperature for 30 min. The suspension was then stirred at room temperature for 30 min, following which it was again cooled down to 0 °C. Then 7 mmol (0.225 g) of sulphur powder was slowly added over a period of 30 min. The resulting solution was the stirred at 25 °C for 30 min and then the reaction was stopped. The solvent was removed by rotary evaporation and 25 ml of diethyl ether was added to the residue containing the compound. This mixture was stirred for some time at 0^oC and then it was added a 6-fold excess of 1 M HCl. The mixture was thoroughly shaken, and the two layers separated. The diethyl ether layer was washed with 1 M HCl (3 x 15 ml), and the aqueous layer, with diethyl ether (15 ml). The combined organic solutions were dried over $MgSO_4$. The filtrate was then removed by rotary evaporation to yield a practically pure yellowish compound containing 93% of 1-SH-1,2-$C_2B_{10}H_{12}$. The pure compound was obtained upon sublimation. [53]

For synthesis of *meta*-carboranethiol, the reaction procedure is essentially the same except for a few variations. The reaction is done in dry Diethyl ether instead of dry Tetrahydrofuran and instead of 0°C, the reaction is performed at -40°C. [53]

For the synthesis of *ortho*-carboranedithiol and *meta*-carboranedithiol, , the respective synthesis procedures for producing their monothiol derivatives were used, with the only difference being that twice the amount of n-butyllithium and Sulphur were added, leading to disubstitution of the C_c atoms, following the scheme depicted in Fig. 9 of the Introduction.

Meta-carboranylphosphinic acid and *meta*-carboranyldiphosphinic acid were produced following the reaction schematic represented in Fig. 10 in the Introduction. This method was developed by Vinas and co. [54] The method for obtaining *meta*-carboranylcarboxylic acid was similar to that of *meta*-carboranethiol, the only difference being the addition of dry ice to the reaction mixture instead of Sulphur. [55]

3.4.2.2 Synthesis of QNCs

This method is a modification of the method proposed by Ubani et al. [56] This is a pyrolysis reaction inspired by the QDs organic preparation procedure as reported by Ubani et al, utilizing 1- Octadecene as the solvent, metallic Selenium powder, CdO as the Cadmium source and the carboranyl ligands depicted above as capping agents.

First step: Synthesis of Selenium precursor: 60mg of Se powder (0.04mmol) and 0.4mL Tri-n-octylphosphine

were added to 10mL of 1-Octadecene. To dissolve the Se powder the mixture was heated to 60^{o}C and stirred for two hours until all the Se powder dissolved. This Se precursor solution was sealed and stored at room temperature undisturbed for 1 week to allow the precursor to form.

Second step (for QNCs): Synthesis of CdSe QNCs: 13 mg of CdO was dissolved in 10mL of 1-Octadecene. CdO and the required carborane derivative was taken in a molar ratio of 1:2. The appropriate amount of Carborane derivative (depending on the molar mass of the derivative) was taken and dissolved in 6mL of 1-Octadecene. Then this mixture of Carborane derivative in 1-Octadecene was added to the CdO solution and then it was heated stepwise till 150^{o}C (rise of 1^{o}C/min) using a heating mantle. To synthesize the different QNCs, a temperature ramp for the final 40-45^{o}C was needed. The temperature of the CdO/carborane ligand solution was increased stepwise up until 150^{o}C (1^{o}C/min) and then the temperature was augmented abruptly till it reached 195^{o}C (rise of 10^{o}C/min). At this point the selenium precursor was added. This represented time zero. The samples were then removed at time intervals of 20s, 30s, 45s, 1 min, and 5 min. Of notable importance is the sudden rise in temperature of the CdO/Carborane ligand solution to give the NCs their final appearance, particularly for the QRs and QR$_{ods}$. Upon reaching 195^{o}C, 1 ml of the preformed Se precursor was injected into the CdO/Carborane derivative mixture. The addition of the Se precursor lead to evolution of smoke which is due to the rapid formation of the CdSe QNCs.

3.4.2.3 Importance of Temperature Ramp

To synthesize QNCs other than QDs, a temperature ramp of 10^{o}C/min for the final stages of the reaction was necessary. After the reaction temperature reaches 150^{o}C, the temperature was raised abruptly until it reached 195^{o}C. If this abrupt temperature rise is not incorporated and then reaction mixture is allowed to reach 195^{o}C at a steady rate of rise (1^{o}C/min), then only QDs are formed, irrespective of the ligand used as capping agent. Such a temperature ramp has already reported to have been necessary for the production of QR$_{ods}$ using TOPO/Oleic Acid. [57]

A reason that this temperature ramp could be necessary for producing QRs and QR$_{ods}$ is that this abrupt increase in temperature leads to formation of nanobubbles which act as template to generate morphologies other than the QDs.

3.4.2.4 Isolation of QNCs

Efforts were made to isolate the synthesized QNCs from its mother solution. After unsuccessful efforts using PTFE filters, some success was achieved by using Ethanol to highly dilute the colloidal solution and then centrifuging it at very high speed. But the amount of Ethanol required for this was very high, more than 10 times the amount of colloidal solution containing the QNCs and even then a completely dry powder was not achieved. The isolated product was not a pure solid but was oil-like in nature as seen in **Fig. 3**.

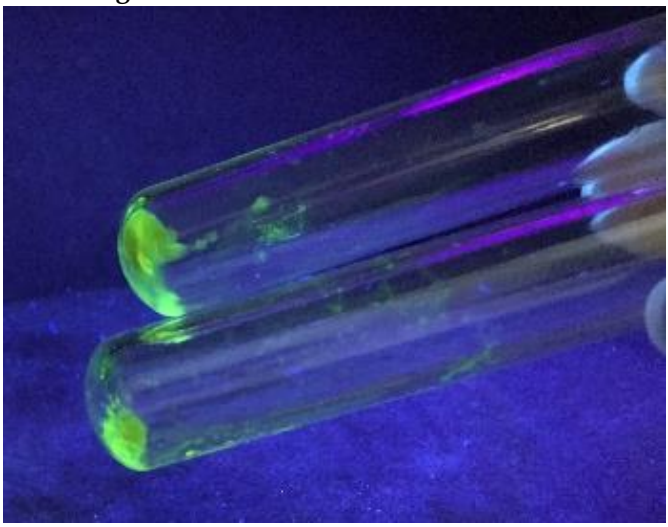

Figure 3. The separated QNCs obtained through centrifugation as viewed under UV lamp.

3.4.3Formation and Characterization of Quantum Nanocrystals

This section contains details of all the different QNCs formed using the aforementioned synthetic process. Each morphology has its own separate section, listing the ligand used for its formation, as well as characterization and fluorescent studies of that particular morphology.

3.4.3.1 Quantum Dots and their characterization

All the aforementioned carboranyl ligands were able to produce QDs, if the temperature ramp was not incorporated. But upon the incorporation of the temperature ramp, only using *meta*-carboranethiol as capping agent led to production of QDs. For the sake of symmetry and demonstrating how one synthetic procedure can lead to production of different types of QNCs just by tuning the ligands, only details of QDs produced upon incorporation of the temperature ramp is mentioned here.

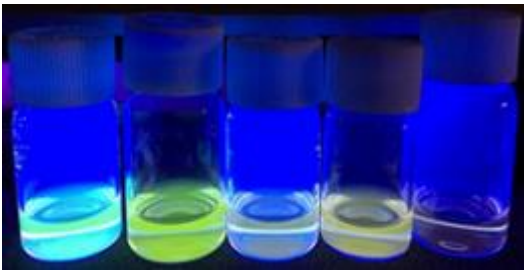

Figure 4. QDs produced using meta- carboranethiol as capping agent. These images show QDs pipetted out at 20s, 30s, 45s, 1 min and 5 min

respectively (from left to right) after Se addition. These images were taken under UV illumination at a wavelength of 365 nm.

The QDs synthesized here were found to have a mean size of 1.95 nm. **Fig. 4** depicts the fluorescent range of colors depicted by these QDs and **Fig. 5** shows the TEM, STEM and HRTEM images of the synthesized QDs.

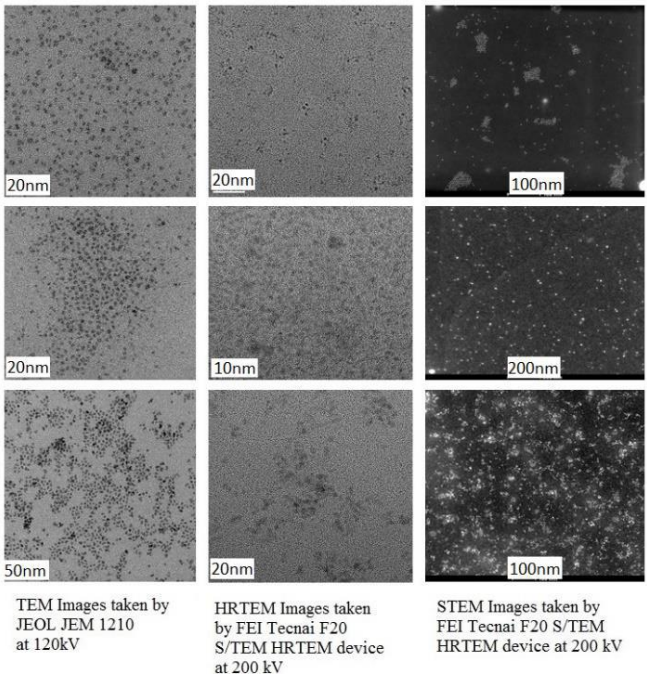

Figure 5. TEM (left), HRTEM (centre) and STEM (right) images of the quantum dots are shown in the above figure.

The existence of Boron, Cadmium, Selenium and Sulphur was proven by spectroscopic techniques as depicted in the figures below.

The EELS (Electron Energy Loss Spectroscopy) spectra in **Fig. 6** confirms the presence of Boron in the QD sample. The IR (Infra-Red) spectra in **Fig. 7** confirms the presence of the characteristic B-H bond present in carboranes. The ratio of Cd, Se and S are depicted in **Fig. 8** by EDX (Energy Dispersive X-Ray) studies.

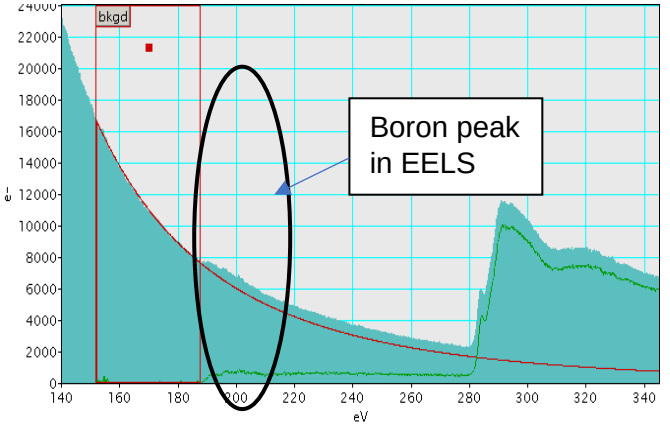

Figure 6. EELS of QDs with *meta*-carboranethiol. The EELS of the sample show the presence of boron in the sample thus proving that these dots are formed by the capping of *meta*-carboranethiol.

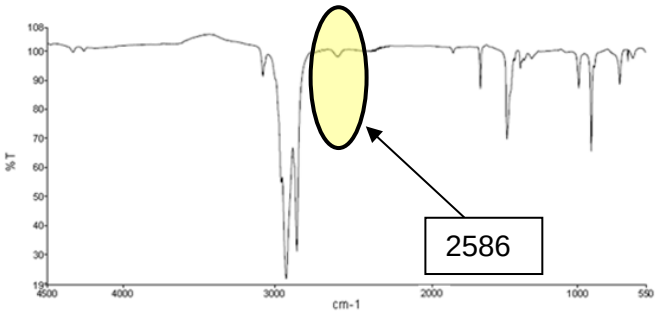

Figure 7. Infrared Spectrum of QDs with *meta*-carboranethiol. The IR of the sample shows the B-H bond stretching from meta-carboranethiol used to cap QDs.

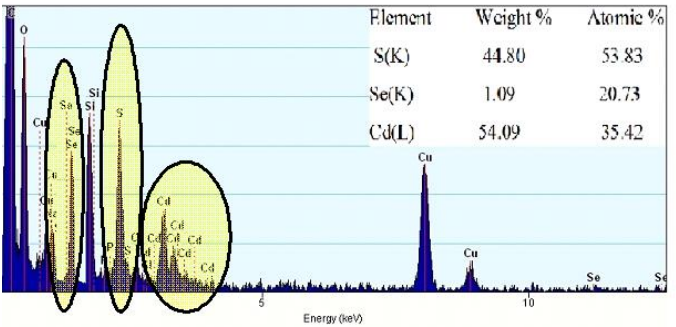

Figure 8. EDX of QDs with *meta*-carboranethiol. The EDX of the sample shows the ratio of Cd, Se and S present in the sample.

The ratio of Cd:Se is almost 2:1 by atomic wt. % which is slightly different from most conventional QDs, which though having a ratio skewed in favour of Cadmium, don't have so much as here. It is this coordination between Cd and Se that leads to the formation of these QDs. This ratio remains nearly constant even as the QDs age with time, as evidenced by ICP studies done 5 months after the synthesis, which showed a Cd: Se molar ratio of 2.13: 1.

Electron Diffraction studies showed that the CdSe QDs had a hexagonal phase and they had an amorphous diffraction pattern, as shown in **Fig. 9**. The mean size of the QDs in 1.95 nm and was calculated as follows: The TEM images were set to scale using ImageJ software, then 200-300 QDs were manually measured using the software and finally using the Gaussian function, the histograms were plotted (**Fig. 10**).

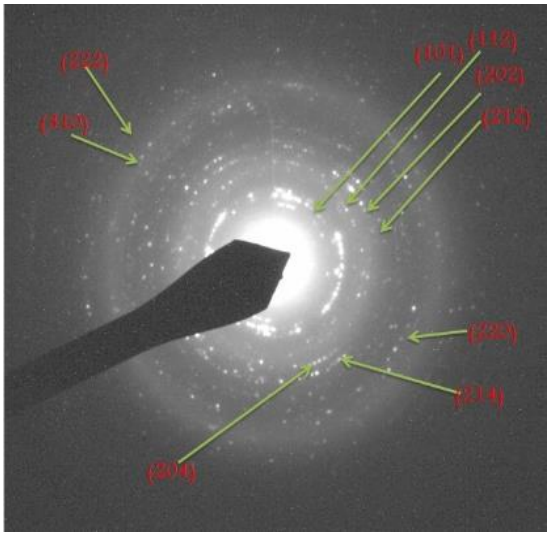

Figure 9. Electron diffraction of QDs capped with *meta*-carboranethiol. The electron diffraction pattern of the rods are monocrystalline and show a hexagonal phase.

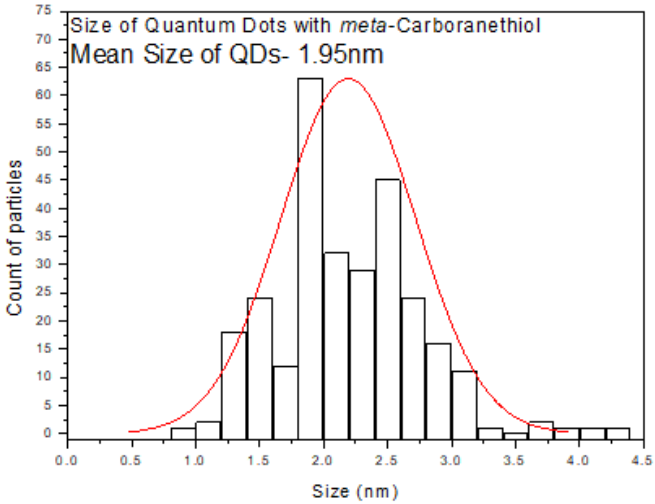

Figure 10. Gaussian size graph of QDs made with *meta*-carboranethiol.

The QDs synthesized using *meta*-carboranethiol showed range of colors from blue to yellow under UV light, depending upon the time at which they were pipetted out from the reaction mixture after Selenium addition. The intensity of Photoluminescent (PL) emission is depicted below in **Fig. 11** of the QDs formed at different times of pipetting out from the solution. The PL studies were conducted using Fluorometer Perkin Elmer LS45 and intensity of emission was recorded in arbitrary units using a filter that only allowed 1% of the total light to pass through, as without the filter, the readings were too high to be measured by the fluorometer. These studies were done by exciting the samples with a light of wavelength 365 nm.

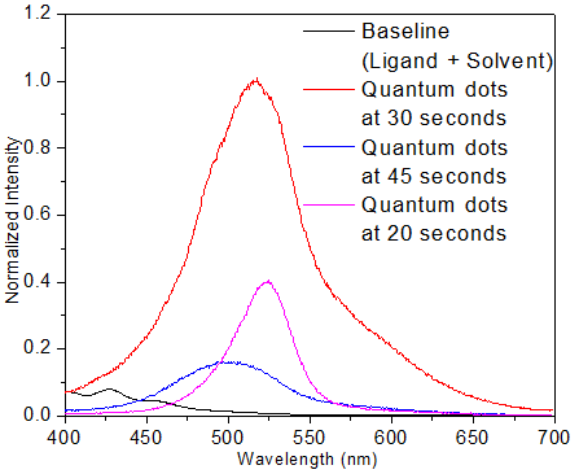

Figure 11. Intensity of PL emission. Intensities were normalized for a succinct depiction as the fluorometer shows intensity values in arbitrary units. The times written denote the time elapsed after Se addition to the reaction mixture when samples were pipetted out.

As is clear from **Fig. 11**, the sample pipetted out after 30s of Se addition shows the maximum PL intensity. After reaching this peak value, the PL intensity decreases, and the samples pipetted out at 1 min and 5 min showed no appreciable PL emission. The range of PL emission was between 500-550 nm. To make sure that any PL emission recorded by the fluorometer was solely due to the QDs and not due to any of the unreacted reagents that may be present in the colloidal solution, blank tests were done. PL emission of each of the reactants was tested individually in the solvent used. None of the reactants showed any appreciable PL emission, a very minute emission was shown by the carboranyl ligand and this value of emission acted as the baseline.

The Absorbance and Excitation spectra for the QDs are depicted below in **Fig. 12** and **Fig. 13** respectively.

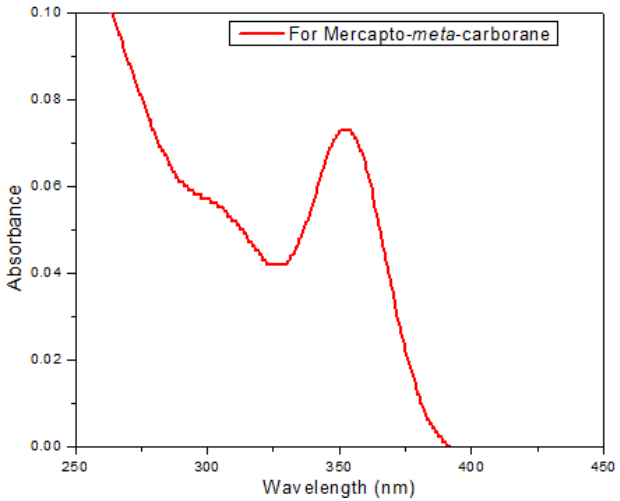

Figure 12. Absorbance spectra of QDs produced using *meta*-carboranethiol. Maximum absorbance is shown around 360 nm.

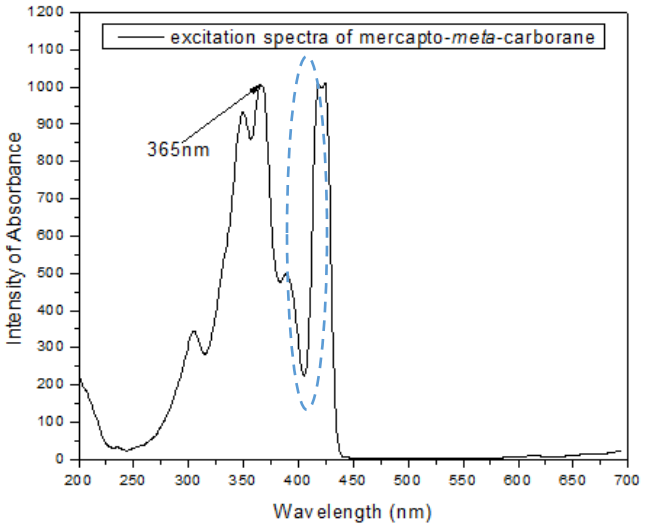

Figure 13. Excitation spectra of the QDs produced using *meta*-carboranethiol. The maximum excitation is shown at 365 nm. The peak highlighted by the blue circle is due to grating diffraction.

It should be noted that usually, for photoluminescent species, the shape of the absorption and the excitation spectra is same. But for QNCs synthesised using carboranyl ligands described here, this is not the case. There is no precedence for this in literature, but since blank tests for each individual reactant have already been conducted and none of them showed any meaningful PL emission or excitation, it is feasible to infer that the absorption and excitation spectra is solely due to the QNCs produced using the carboranyl ligands. At this juncture, there is no explanation for the unique shape of the Excitation and Absorbance spectra, but it is undoubtedly due to the presence of the carboranyl ligands as capping agents. Further studies in the future will need

to be conducted before a working theory can be developed regarding these excitation and absorbance spectra.

To measure the Quantum Yield (QY), the method specified by Grabolle et al was used. [58] Multiple excitation wavelength (325 nm and 348 nm) were used and two standards, namely, Rhodamine B and Rhodamine 6G in ethanol were used. The formula used to calculate is given below:

$$\mathbf{QY = QY_{ref}\{\eta^2\ I\ A_{ref}\ (\eta_{ref}\ I_{ref}\ A)^{-1}\}}$$

Where QY_{ref} – Quantum Yield of the reference (Rhodamine 6G or Rhodamine B)
η- Refractive index of the solvent (Octadecene)
η_{ref}- Refractive index of the solvent of the standard (Ethanol)
I- Integrated area of emission spectrum of sample
I_{ref} – Integrated area of emission spectrum of reference
A- Absorbance value of sample
A_{ref}- Absorbance value of the reference

Since, each sample pipetted out at different time would show different QY, only the QY of the sample showing the maximum intensity of PL emission was measured. In this case that was the sample pipetted out 30 seconds after addition of Se precursor. Two concentrations of the sample were used to measure the absorbance until the value of absorbance were less than 0.1. These absorbance values were taken for the QY measurement, while the excitation wavelength used were 325 nm and 348 nm to record the emission peaks. The integrated area under these emission peaks were used in the QY measurements. The final QY was calculated by taking the average of the QYs measured by using Rhodamine 6G (QY of 0.95) and

Rhodamine B (QY of 0.66) as references and was found to be 76.6%.

3.4.3.2 Quantum Rods and their characterization

Using *ortho*-carboranethiol and *meta*-carboranedithiol as capping agents in the aforementioned synthesis procedure led to the formation of QR_{ods}.

Sphere-to-Rod transitions of non-ionic surfactant micelles in aqueous solution have been reported [59-60] and a case could be made for a similar transition in the quantum regime (QDs to QR_{ods}) akin to what is being reported in this work. But the two processes are not related. In the first one, the transition is due to an increasing concentration of the same surfactant going through two CMC; in the case reported here the syntheses of both the QDs and QR_{ods} are done at the same concentration of Cd and Se precursors and the distinct carboranes. Further the solvent and temperature and temperature ramps are alike in the different processes. The only differences are the carboranes with their distinct ligating sites and non-binding substituents. Thus, it is theorized that the interplay of the hydrophobic interactions between carborane units, the hydrogen bonding, the electronically minor but sterically relevant carborane substituents, the sphere packings and the consequences of the mismatch described earlier is what leads to the formation of these geometric features. Additionally, as mentioned earlier, the nanobubbles generated due to the temperature ramp

could act as a template for generation of morphologies other than QDs. This is conjectural but may be an explanation to account for the necessity of abrupt temperature increase to generate different QR_{ods} (and also QRs), as opposed to the traditional QDs if the abrupt temperature raise does not take place.

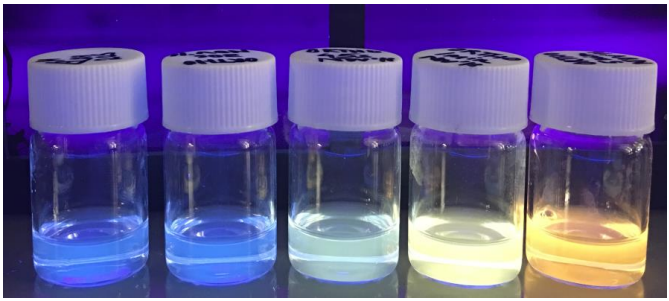

Figure 14. QR_{ods} produced using *ortho*-carboranethiol as capping agent. These images show QR_{ods} pipetted out at 20s, 30s, 45s, 1 min and 5 min respectively (from left to right) after Se addition. These images were taken under UV illumination at a wavelength of 365 nm.

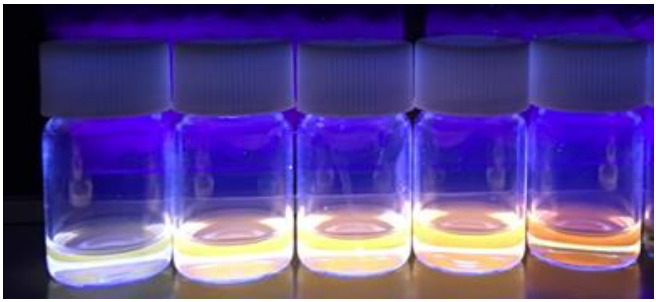

Figure 15. QR_{ods} produced using *meta*- carboranedithiol as capping agent. These images show QR_{ods} pipetted out at 20s, 30s, 45s, 1 min and 5 min respectively (from left to right) after Se addition. These images were taken under UV illumination at a wavelength of 365 nm.

Fig. 14 and **Fig. 15** show the fluorescent emission of QR_{ods} formed by using *ortho*-carboranethiol and *meta*-carboranedithiol as capping agents, respectively. **Fig. 16** depicts the TEM and HRTEM images of these QR_{ods}.

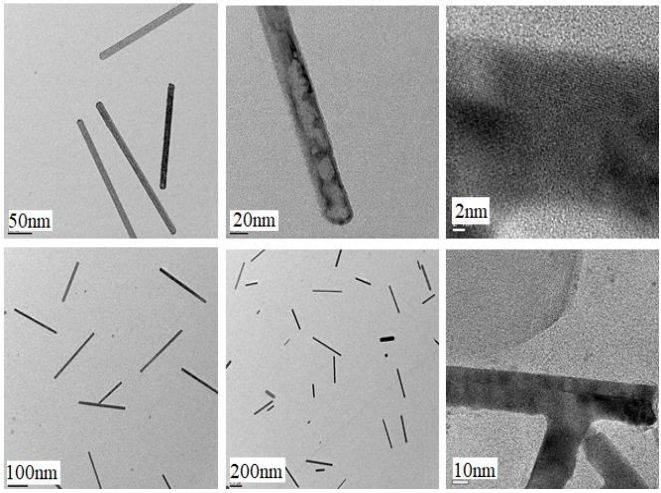

Figure 16. TEM images (First two rows) and HRTEM images (Last row) of the QR_{ods} are shown in the above figure.

The presence of Boron, Cadmium, Selenium and Sulphur were proven by the spectroscopic techniques listed below. The EELS spectra in **Fig. 17** and **Fig. 18** confirms the presence of Boron in the QR_{ods} sample. The IR spectra in **Fig. 19** confirms the presence of the characteristic B-H bond present in carboranes. The ratio of Cd, Se and S are depicted in **Fig. 20** and **Fig. 21** by EDX studies.

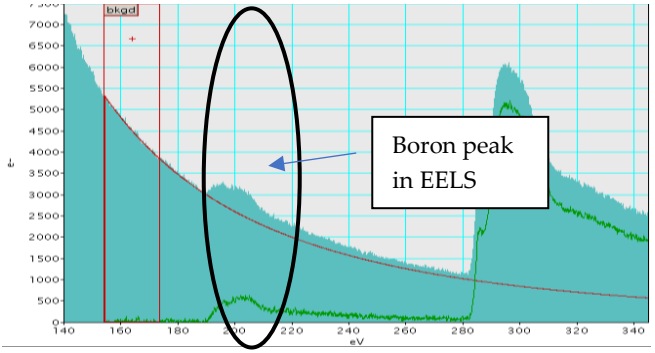

Figure 17. EELS of QR_{ods} with *ortho*-carboranethiol. The EELS of the sample show the presence of boron in the sample thus proving that these rods are formed by the capping of *ortho*-carboranethiol.

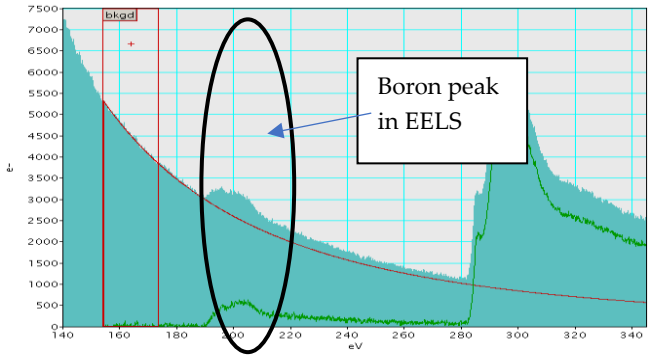

Figure 18. EELS of QR_{ods} with *meta*-carboranedithiol. The EELS of the sample show the presence of boron in the sample thus proving that these rods are formed by the capping of *meta*-carboranedithiol

.

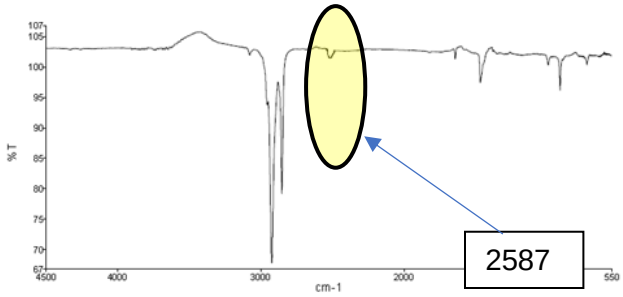

Figure 19. Infrared Spectrum of QR_{ods}. The IR of the sample shows the characteristic B-H band stretching which indicates presence of a carboranyl group.

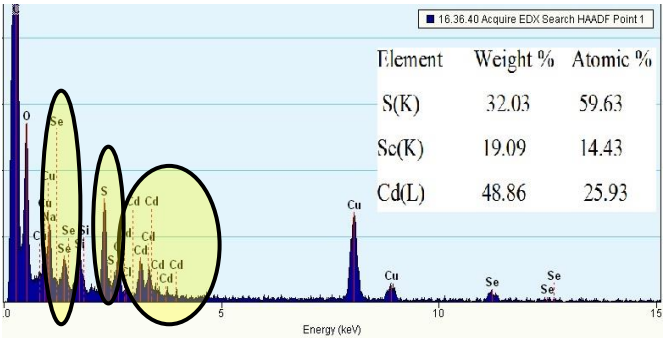

Figure 20. EDX of QR_{ods} with *ortho*-carboranethiol. The EDX of the sample shows the ratio of Cd, Se and S present in the sample.

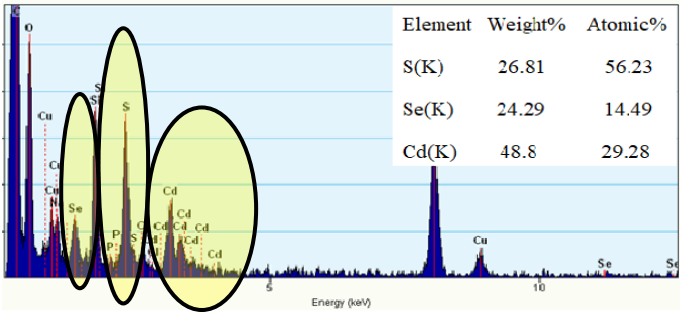

Figure 21. EDX of QR_{ods} with meta-carboranedithiol. The EDX of the sample shows the ratio of Cd, Se and S present in the sample.

The ratio of Cd:Se is again almost 2:1, which as mentioned in the previous section, is unconventional but it is this skewed ratio that helps in the generation of these novel structures. The ratio remains constant over a period of 5 months and was found to be 2.13:1 in favor of Cd when checked by ICP analysis.

Electron diffraction studies confirmed the presence of CdSe structures of hexagonal phase and the QR_{ods} had a more crystalline diffraction pattern as shown in **Fig. 22**. The mean size of the QR_{ods} was calculated using a Gaussian graph as explained in the previous section. The mean size of QR_{ods} capped with ortho-carboranethiol was 12.10 nm while the mean size of those capped with meta-carboranethiol was 9.49 nm.

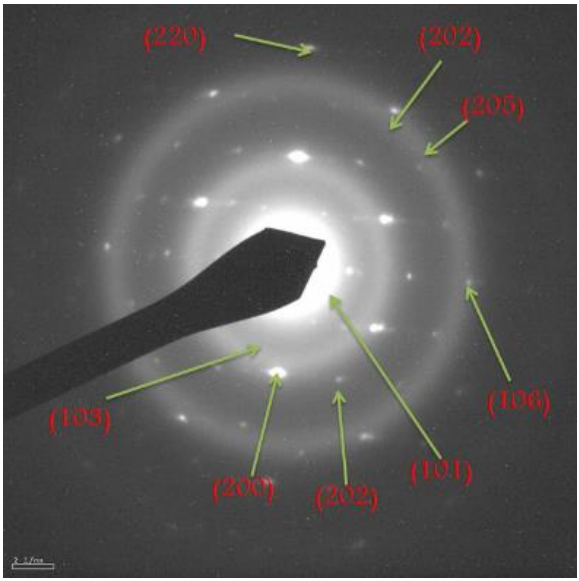

Figure 22. Electron diffraction of QR_{ods}. The electron diffraction of QR_{ods} is more monocrystalline as compared to the QDs.

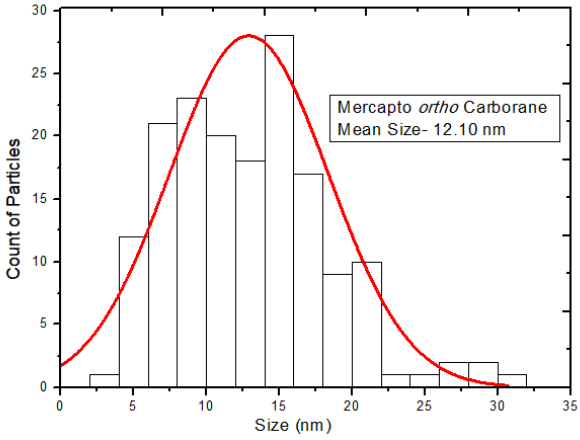

Figure 23. Gaussian size graph of QR_{ods} made with *ortho*-carboranethiol.

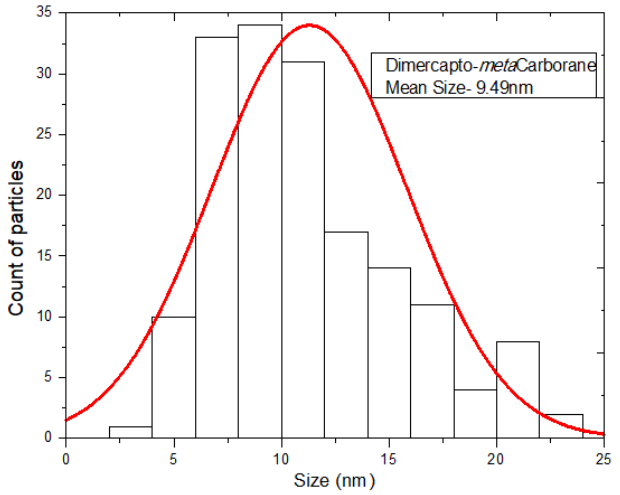

Figure 24. Gaussian size graph of QR_{ods} made with *meta*-carboranedithiol.

The QR_{ods} capped with *ortho*-carboranethiol emitted the range of colors from blue to yellow when excited by UV light, depending upon the time of pipetting out of the samples from the reaction mixture after selenium addition. The intensity of Photoluminescent (PL) emission is depicted below in **Fig. 25** of the QR_{ods} formed at different times of pipetting out from the solution. The PL studies were conducted using Fluorometer Perkin Elmer LS45 and intensity of emission was recorded in arbitrary units using a filter that only allowed 1% of the total light to pass through, as without the filter, the readings were too high to be measured by the fluorometer. These studies were done by exciting the samples with a light of wavelength 365 nm.

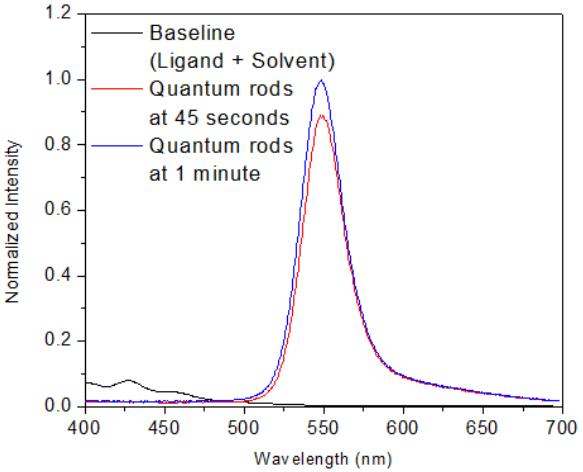

Figure 25. Intensity of PL emission of QR_{ods} capped with ortho-carboranethiol. Intensities were normalized for a succinct depiction as the fluorometer shows intensity values in arbitrary units. The times written denote the time elapsed after Se addition to the reaction mixture when samples were pipetted out.

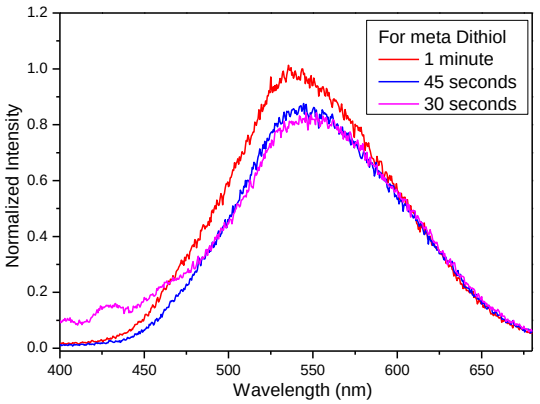

Figure 26. Intensity of PL emission of QR_{ods} capped with *meta*-carboranedithiol. Intensities were normalized for a succinct depiction as the fluorometer shows intensity values in arbitrary units. The times written denote the time elapsed after Se addition to the reaction mixture when samples were pipetted out.

As is clear from **Fig. 25** and **Fig. 26**, the sample pipetted out after 1 min of Se addition shows the maximum PL intensity. The samples pipetted out after 20s after Se addition showed no appreciable PL emission. The sample pipetted out after 45s and 1 min after Se addition showed appreciable PL intensity and it gradually faded to an amount that was not comparable to the intensity of these two samples, 5 min after Se addition. This implies that contrary to the QDs, the QR_{ods} take longer to fully form, but after full formation, become too large in size if the reaction is allowed to go on for too long and hence lose their high intensity of PL emission. The range of PL emission was around 550 nm. As mentioned in the previous section, blank tests were conducted with each of the individual reactants to ensure that any PL emission recorded by the fluorometer was solely due to the formation of QR_{ods}. Absorbance and Excitation spectra of the QR_{ods} are shown in the figures below.

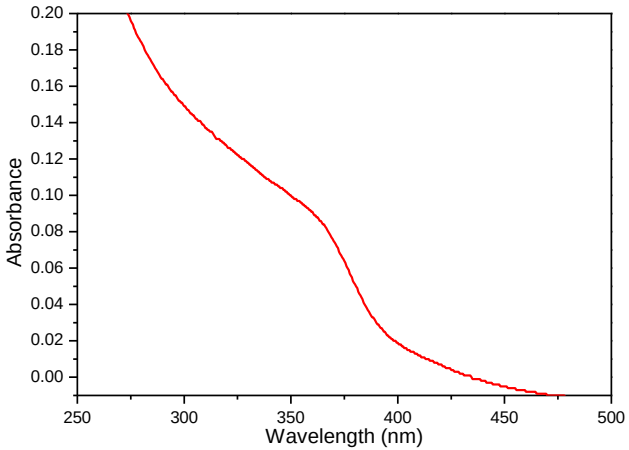

Figure 27(a). Absorption spectrum for QR_{ods} formed by *ortho*-carboranethiol.

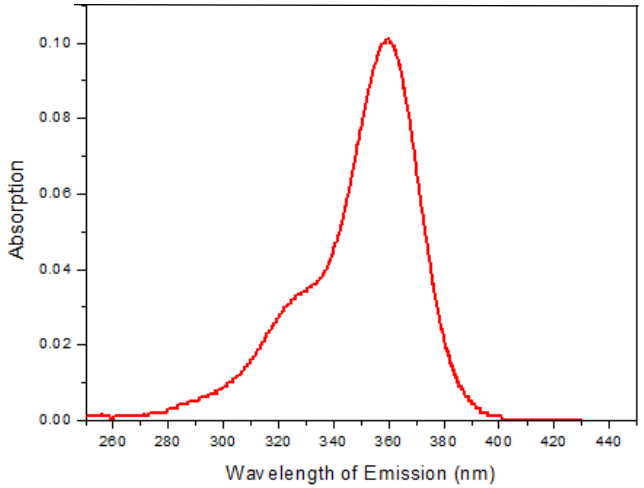

Figure 27 (b). Absorption spectrum for QR_{ods} formed by *meta*-carboranedithiol.

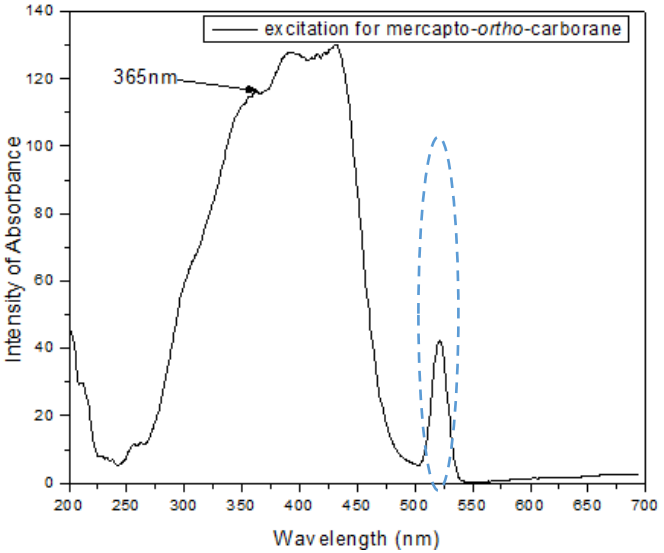

Figure 28 (a). Excitation spectrum of the QR_{ods} capped with *ortho*-carboranethiol. The spectrum shows maximum excitation at 365 nm. The peak highlighted in blue denotes grating diffraction.

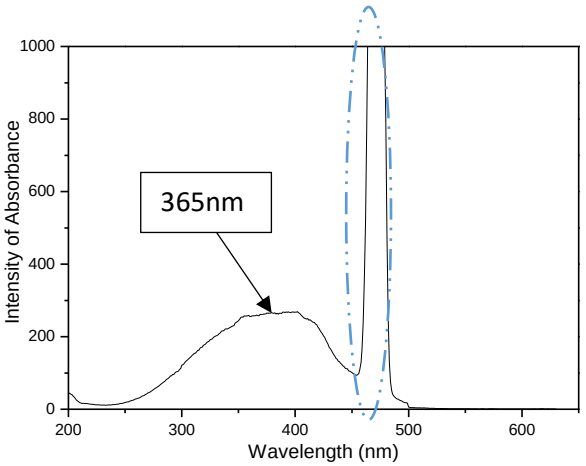

Figure 28 (b). Excitation spectrum of the QR_{ods} capped with *meta*-carboranedithiol. The spectrum shows maximum excitation at 365 nm. The peak highlighted in blue diffraction denotes grating diffraction.

As with the QDs capped using carboranyl thiol, we observed a unique dissonance between the Excitation and Absorption spectra, the reasons for which have already been alluded to in the previous section.

The method used to calculate the QY has been described in detail in the previous section and was calculated to be 69.95% for the QR_{ods} capped with *ortho*-carboranethiol and 50.4% for the QR_{ods} capped with *meta*-carboranedithiol.

3.4.3.3 Quantum Rings and their characterization

Quantum Rings were produced using 1-methyl-*ortho*-2-carboranethiol, *meta*-carboranephosphinic acid and *meta*-carboranediphosphinic acid as capping agents.

QRs take a longer time than QDs and QR_{ods} to be formed fully. When produced using 1-methyl-*ortho*-2-carboranethiol as capping agent, they show a linear growth, both in terms of morphology and PL intensity. They start appearing 45 seconds after Selenium addition to the reaction mixture and are fully formed 1 minute after Selenium addition. If the reaction is allowed to run for longer than 5 minutes after Selenium addition, the QRs already start aggregating. This process is shown in **Fig. 29** where samples were pipetted out at 5 different intervals of the reaction stage after Se addition and observed under TEM. As is clear from the figure, the formation of full fledged QRs is what leads to a marked increase in PL intensity.

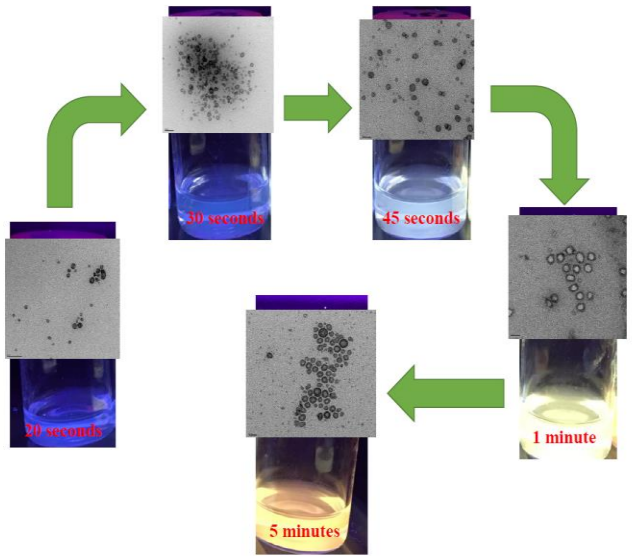

Figure 29. Schematic depicting the formation of QRs over time. The time written corresponds to the time elapsed after the addition of Se precursor to the reaction mixture. The fluorescence (or lack of) observed under UV light corresponds to the different stages of the reaction procedure.

The QRs with 1-methyl-*ortho*-2-carboranethiol show the full spectrum of color of PL emission from blue to yellow indicating a facile growth process with time. On the other hand, the QRs capped with *meta*-carbronephosphinic acid and *meta*-carboranediphosphinic acid indicate a less favorable and linear growth process. They took much longer to form than all the other QNCs, taking as long as 5 minutes to form fully fledged QRs when using *meta*-carboranediphosphinic acid and 1 minute when using *meta*-carboranephosphinic acid. It is at this point that they show maximum PL intensity which decreases as the QRs grow in size. **Fig. 30** shows a probable structure for QRs generated with phosphinic acid derivatives of carboranyl ligands, in which every single Selenium is bonded to four cadmium atoms; each cadmium is linked to three Se and to two P from the carborane units. The structure as proposed has a width of 2nm. But the largest rings made by *meta*-carboranephosphinic acid and *meta*-carboranediphosphinic acid have a size of 19.2 nm of the inner ring, thus indicating that covalent piling of these units is possible as are hydrophobic interactions between carborane units. The piling up of the layers along with the bulk and hydrophobicity of the carborane spheres, can cause a distortion to occur, to minimize the surface energy, which would facilitate the formation of the QRs at a high temperature, with the nanobubbles originated due to the sudden

temperature rise acting as a template for QRs formation.

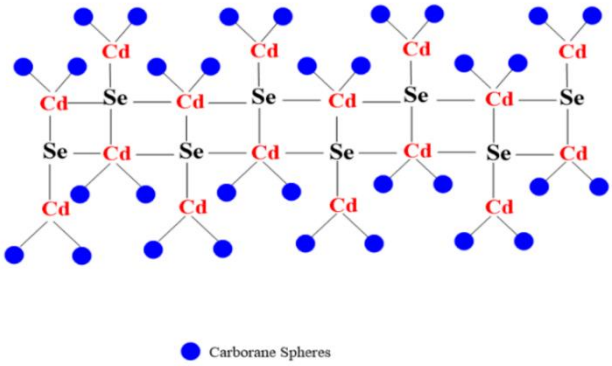

Figure 30. The structure proposed for the QRs synthesized with the carborane derivatives.

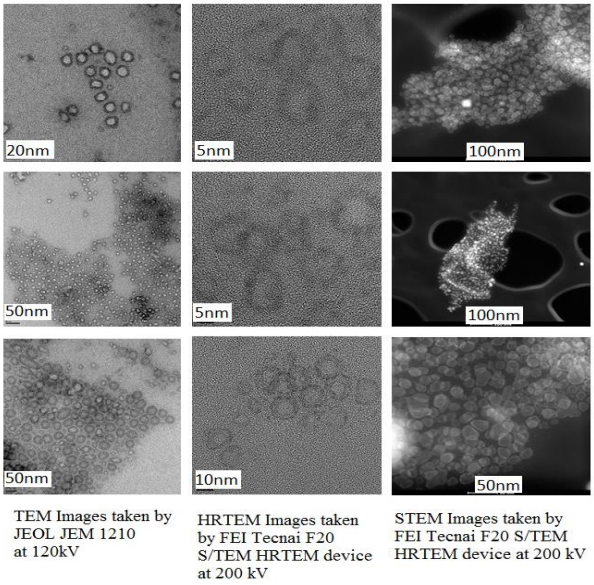

Figure 31. TEM, HRTEM and STEM images of QRs capped with 1-methyl-*ortho*-2-carboranethiol

.

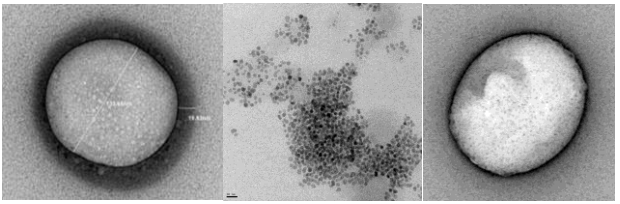

Figure 32. TEM images of QRs formed by using *meta*-carboranephoshinic acid (left and centre) and *meta*-carboranediphosphinc acid (right). The left and right images are magnified images of a single QR to give a better idea of their morphology.

Figure 33. QRs produced using meta- carboranephosphinic acid as capping agent. These images show QRs pipetted out at 45s, 1 min, 5 min and 15 min respectively (from left to right) after Se addition. These images were taken under UV illumination at a wavelength of 365 nm.

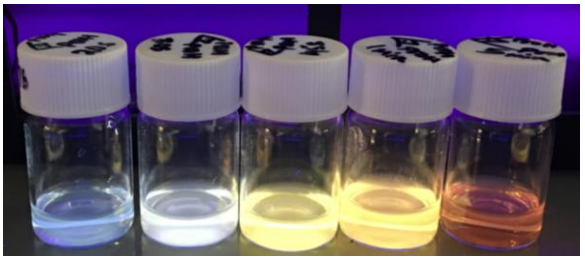

Figure 34. QRs produced using meta- carboranediphosphinic acid as capping agent. These images show QRs pipetted out at 1 min, 5 min, 10

min, 15 min and 30 min respectively (from left to right) after Se addition. These images were taken under UV illumination at a wavelength of 365 nm.

The presence of Boron, Cadmium, Selenium and Phosphorous were confirmed by the spectroscopic techniques listed below. The EELS spectra in **Fig. 35**, **Fig. 36** and **Fig. 37** confirms the presence of Boron in the QR_{ods} sample. The IR spectra in **Fig. 38** confirms the presence of the characteristic B-H bond present in carboranes. The ratio of Cd, Se, S and P are depicted in **Fig. 39**, **Fig. 40** and **Fig. 41** by EDX studies.

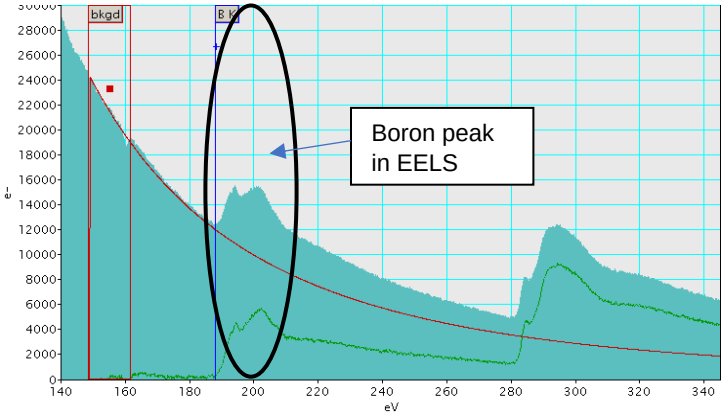

Figure 35. EELS of the QRs capped with 1-methyl-*ortho*-2-carboranethiol. The presence of Boron is confirmed.

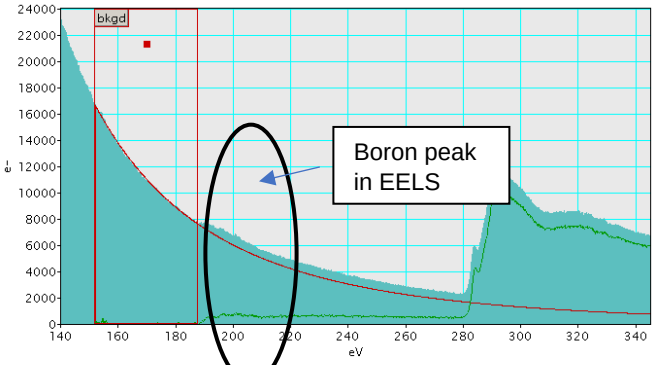

Figure 36. EELS of the QRs capped with *meta*-carboranephosphininc acid. The presence of Boron is confirmed.

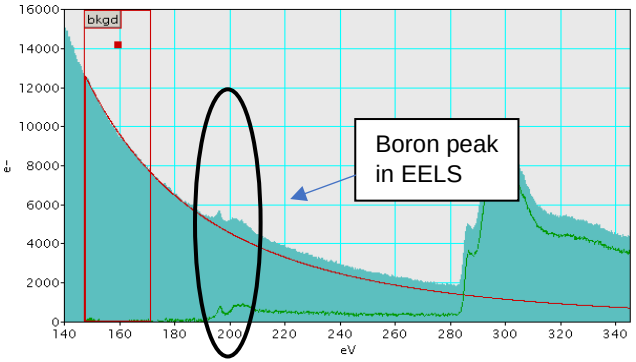

Figure 37. EELS of the QRs capped with *meta*-carboranediphosphinic acid. The presence of Boron is confirmed.

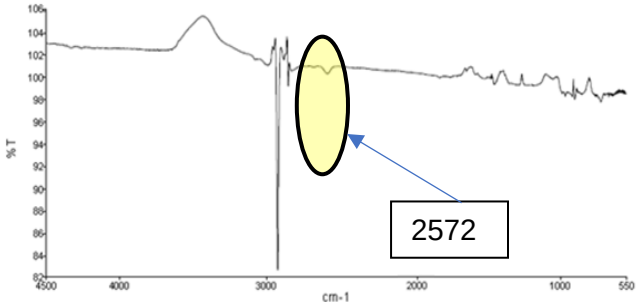

Figure 38. IR spectra of the QRs. The IR spectrum shows the characteristic B-H band stretching which indicates the presence of a carboranyl group.

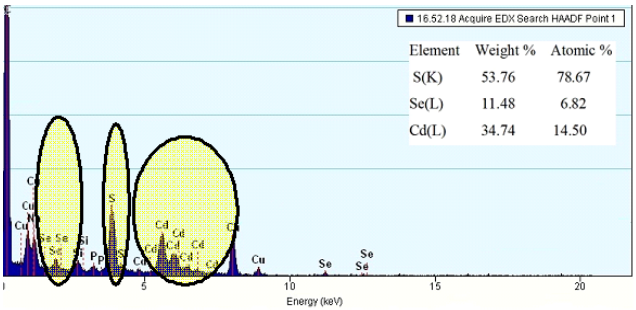

Figure 39. EDX of the QRs capped with 1-methyl-*ortho*-2-carboranethiol. EDX of the sample shows the ratio of Cd, Se and S present.

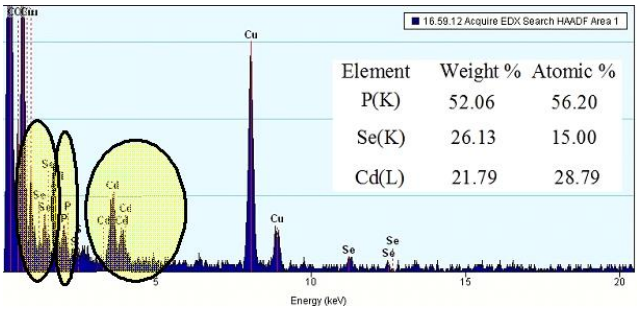

Figure 40. EDX of the QRs capped with *meta*-carboranephosphinic acid. EDX of the sample shows the ratio of Cd, Se and P present.

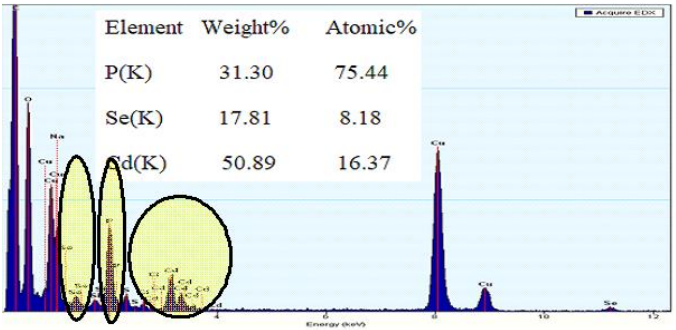

Figure 41. EDX of the QRs capped with *meta*-carboranediphosphinic acid. EDX of the sample shows the ratio of Cd, Se and P present.

For the QRs capped with 1-methyl-*ortho*-2-carborane, the EDX ratio confirms the Cd:Se ratio of 2:1, the significance of which in the formation of novel QNCs has already been explained in previous sections. For the QRs formed by capping with *meta*-carboranephosphinic acid, the ratio of Cd:Se:P is 2:1:4, which is in agreement with the model proposed in **Fig. 30.** Capping with *meta*-carboranediphosphinic acid, the amount of P is twice than in the previous case, since the 2 P groups are attached to the carboranyl ligand. ICP analysis confirmed that these ratio remain stable even 5 months after formation of these QRs.

Electron diffraction studies showed that the CdSe QRs had a hexagonal phase and were more polycrystalline, as shown in **Fig. 42**. The mean size of the QRs capped by 1-methyl-*ortho*-2-carbone is 4.12 nm and for QRs capped by phosphinic acid derivatives of the carboranyl ligands, the mean size was 5.32 nm, though the size variation in the latter QRs is much more as letting the reaction go on for longer time periods leads to formation of very large QRs.

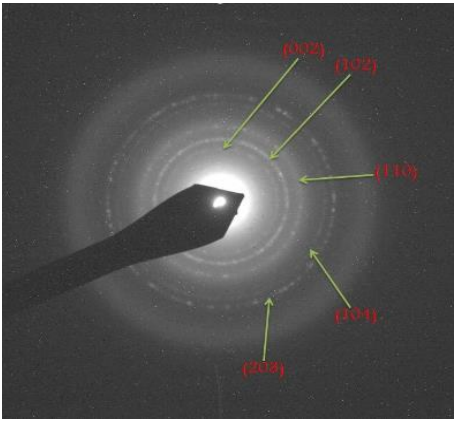

Figure 42. Electron diffraction pattern of the QRs.

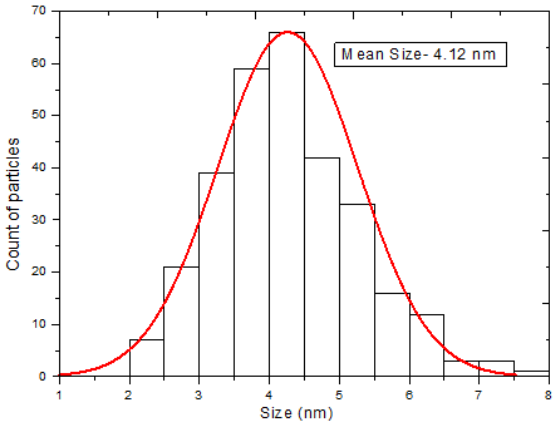

Figure 43. Gaussian size graph of QRs capped by 1-methyl-*ortho*-2-carborane.

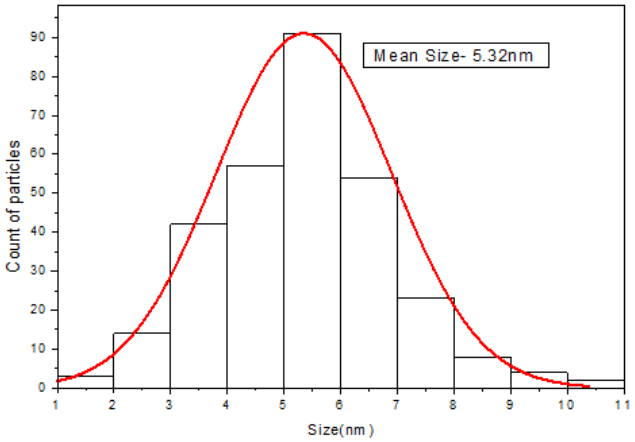

Figure 44. Gaussian size graph of QRs capped using phosphinic derivatives of carboranyl ligands.

The QRs capped with 1-methyl-*ortho*-2-carboranethiol, upon excitation with UV light of wavelength 365 nm, showed a fluorescent emission of range of colors from blue to yellow, depending upon the time of pipetting out from the reaction mixture after Se addition. The QRs capped with *meta*-carboranephosphinic acid and *meta*-carboranediphosphinic acid showed a similar spectrum of fluorescent emission in terms of color, upon excitation by UV wavelength of 365 nm. The intensity of PL emission is depicted in the figures below. The PL studies were conducted using Fluorometer Perkin Elmer LS45 and intensity of emission was recorded in arbitrary units using a filter that only allowed 1% of the total light to pass through, as without the filter, the readings were too high to be measured by the fluorometer.

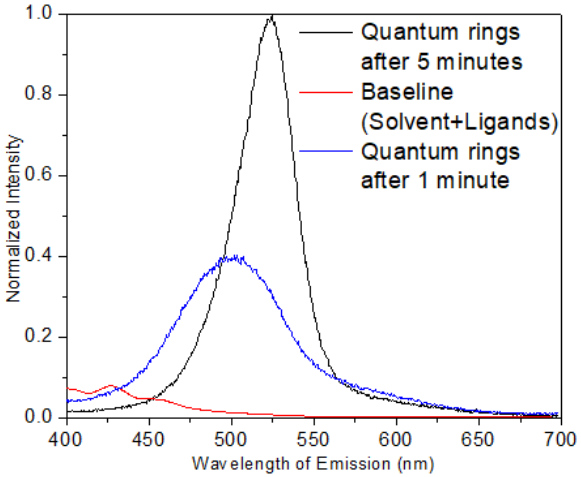

Figure 45. Intensity of PL emission of QRs capped with 1-methyl-*ortho*-2-carboranethiol. Intensities were normalized for a succinct depiction as the fluorometer shows intensity values in arbitrary units. The times written denote the time elapsed after Se addition to the reaction mixture when samples were pipetted out.

As is clear from **Fig. 45** and already alluded to earlier, the intensity of PL emission is directly dependant on the complete formation of QRs. Only when the QRs are fully formed, 1 min and 5 min after Se addition, do they show appreciable PL emission. The range of emission of these samples was between 500 and 550 nm.

For the QRs capped with *meta*-carboranephosphinic acid, the maximum PL emission intensity is shown by the QRs formed 1 min after Se addition (**Fig. 46**) and then it gradually decreases as the size of the QRs increases. Similarly, for QRs capped with *meta*-carboranediphosphinic acid, the maximum PL emission intensity is observed when the QRs are fully formed, i.e, 5

min after Se addition (**Fig. 47**) and then the intensity gradually decreases as size of the QRs increases upon progression of the reaction.

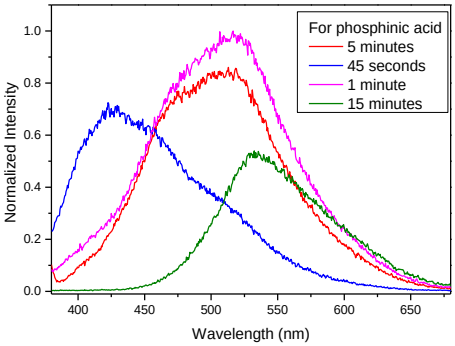

Figure 46. Intensity of PL emission of QRs capped with *meta*-carboranephosphinic acid. Intensities were normalized for a succinct depiction as the fluorometer shows intensity values in arbitrary units. The times written denote the time elapsed after Se addition to the reaction mixture when samples were pipetted out.

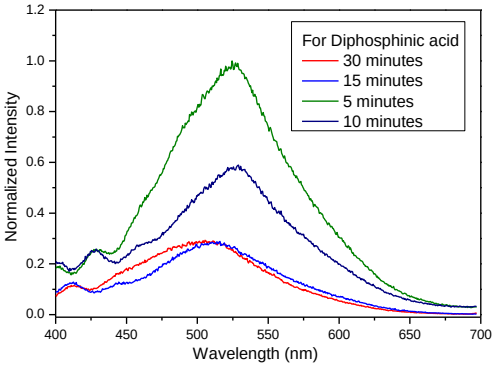

Figure 47. Intensity of PL emission of QRs capped with *meta*-carboranediphosphinic acid. Intensities were normalized for a succinct depiction as the fluorometer shows intensity values in arbitrary units. The times written denote the time elapsed after Se addition to the reaction mixture when samples were pipetted out.

Absorbance and Excitation spectra of the QRs are shown below. Absorption was observed in all cases around 365 nm.

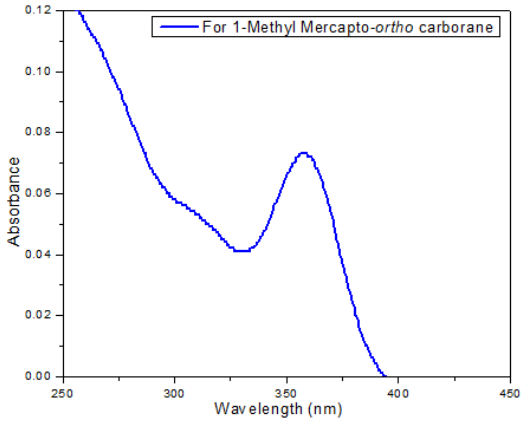

Figure 48(a). Absorption spectrum of QRs capped with 1-methyl-*ortho*-2-carboranethiol.

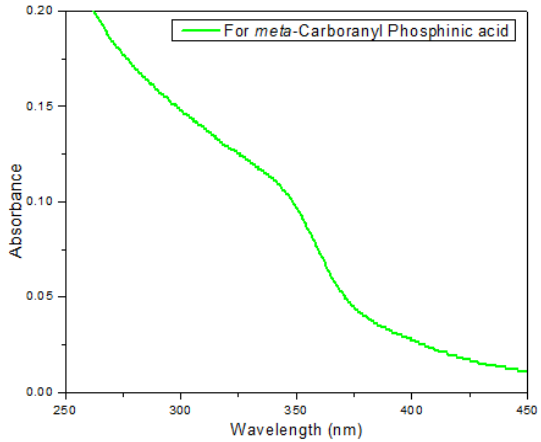

Figure 48 (b). Absorption spectrum of QRs capped with *meta*-carboranephosphinic acid.

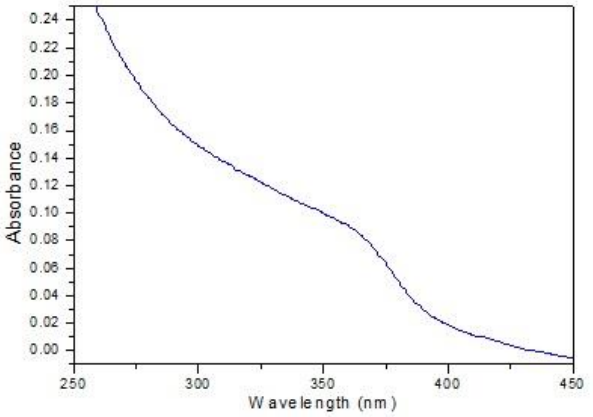

Figure 48 (c). Absorption Spectrum of QRs capped with *meta*-carboranediphosphinic acid.

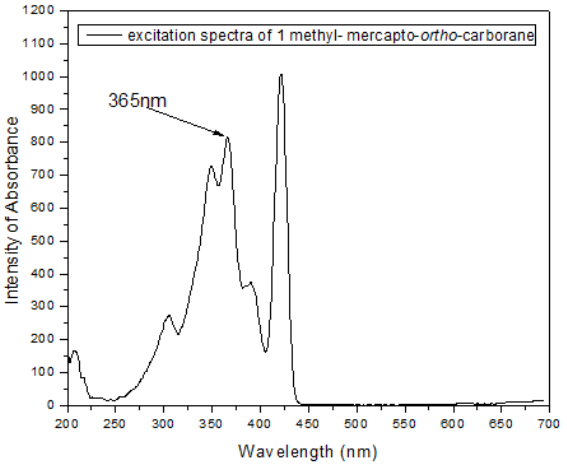

Figure 49 (a). Excitation spectrum of QRs capped with 1-methyl-*ortho*-2-carboranethiol.

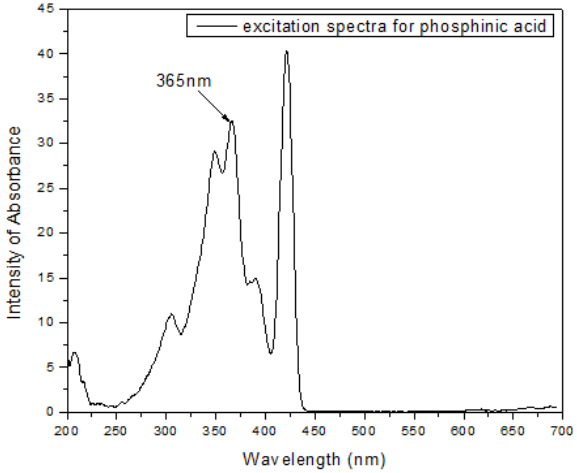

Figure 49 (b). Excitation spectrum of QRs capped with *meta*-carboranephosphinic acid.

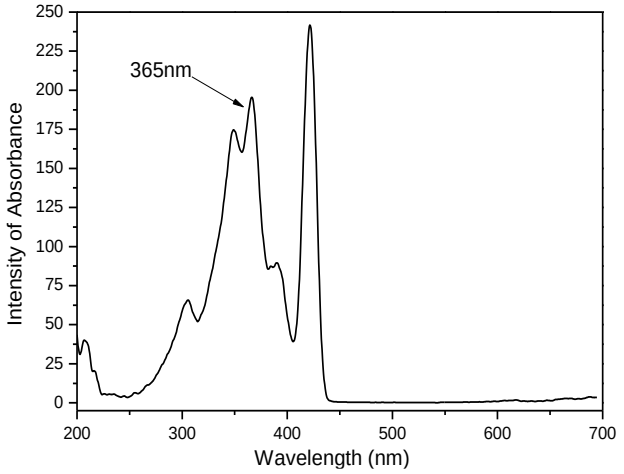

Figure 49 (c). Excitation spectrum of QRs capped with *meta*-carboranediphosphinic acid.

3.4.4.4 Quantum Tetrapods and their characterization

The most surprising formation using carboranyl ligands as capping agents in the synthetic method described earlier, was the appearance of Quantum Tetrapods (QTPs), a very rare morphology that has never been synthesized before using a one-step colloidal synthesis. [61-62] These QTPs were produced by using meta-carboranecarboxylic acid as capping agent.

These QTPs showed a unique property, unforeseen in any of the other QNCs produced using carboranyl ligands, of changing colors of PL emission as they aged. Upon pipetting put from the reaction mixture, these QTPs showed a green colored emission upon excitation with UV light of 365 nm, but after 3 months, they showed a yellow colored emission which changed to orange after 5 months.

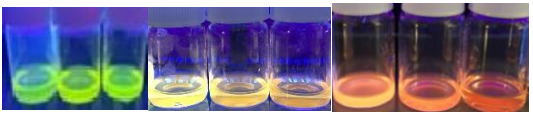

Figure 50. The change of color of PL emission as the samples age with time. The samples on the left are those pictured immediately after synthesis, the middle ones after 3 months of synthesis and the samples on the right, 5 months after synthesis.

Another unique property about these QTPs was that all the QTPs produced were of the same size and hence, showed almost the same PL emission irrespective of the length of reaction time after Se addition. QTPs were all formed within the first minute after Se addition and allowing the reaction to run longer did not lead to formation of these fascinating nanocrystals.

The change in color with the passage of time, even though they have been removed from the reaction conditions, would suggest that these QTPs keep growing with time or aggregating, but the TEM of QTPs done at different times after their synthesis suggest that their size stays constant. The EDX of the samples showed that the Cd:Se ratio also stayed constant irrespective of the passage of time. The change in color of PL emission seems to be independent of size or chemical composition. (**Fig. 51** and **Fig. 52**)

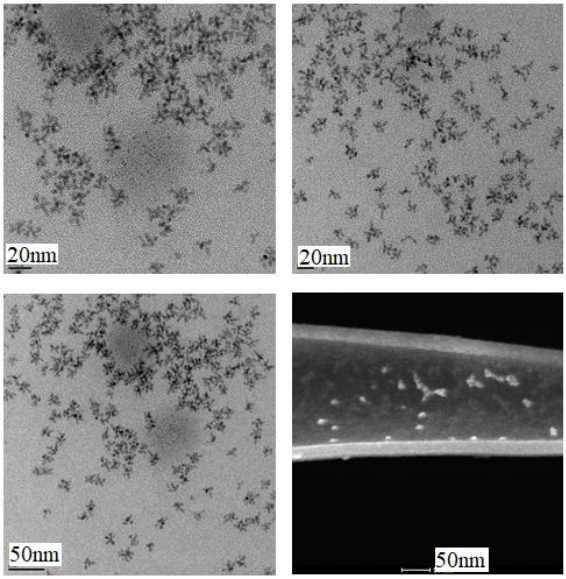

Figure 51. TEM (left top, bottom and right top), and STEM (right bottom) images of the QTPs are shown in the above figure, taken after synthesis, three months and five months after synthesis. The QTPs have maintained their size over the period of five months as seen by the TEM images here.

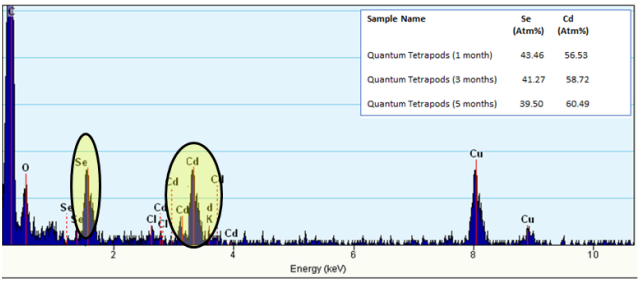

Figure 52. EDX of QTPs. The EDX of the sample shows the ratio of Cd and Se over different months and it remains almost comparable over the period of five months.

It should be noted that the Cd:Se ratio in the case of QTPs is 3:2, unlike the 2:1 ratio observed for other QNCs synthesised using carboranyl ligands.

One tentative explanation for the change in color with the passage of time is that different phases are generated as a result of the aging of the samples which leads to this color change. In support of this, it was observed that the QTPs have the hexagonal wurtzite structure 1 month after synthesis, while as the QTPs age with time they show a cubic zinc blende phase. (**Fig. 53**)

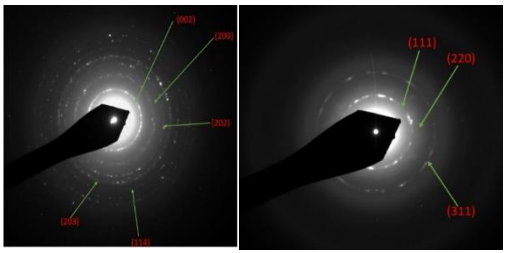

Figure 53. Electron diffraction of QTPs after 1 month (left) of synthesis confirms CdSe in hexagonal structure and after 5 months (right) confirms CdSe in cubic structure. The diffraction pattern is polycrystalline in nature.

The EELS of the sample confirmed the presence of Boron as shown in **Fig. 54**.

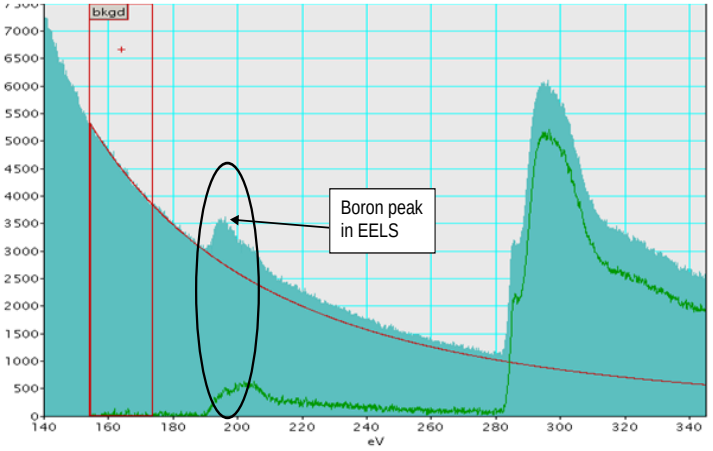

Figure 54. The presence of Boron in the QTPs was confirmed by EELS.

The PL studies were conducted using Fluorometer Perkin Elmer LS45 and intensity of emission was recorded in arbitrary units using a filter that only allowed 1% of the total light to pass through, as without the filter, the readings were too high to be measured by the fluorometer. Since the intensity of PL emission stayed same even after the passage of time, only the PL emission intensity of the samples immediately after synthesis is shown.

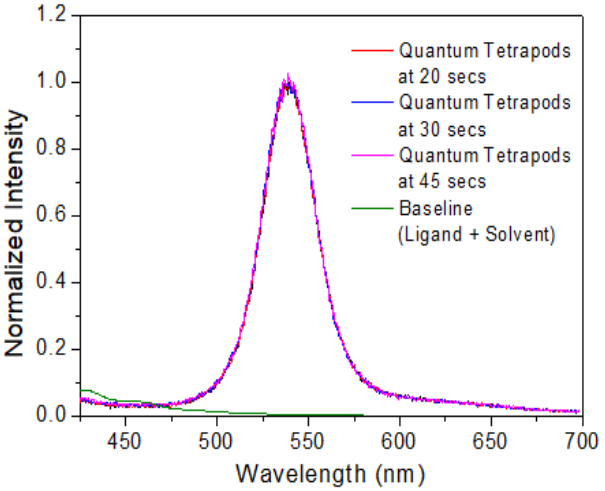

Figure 55. Intensity of PL emission of QTPs capped with meta-carboranecarboxylic acid. Intensities were normalized for a succinct depiction as the fluorometer shows intensity values in arbitrary units. The times written denote the time elapsed after Se addition to the reaction mixture when samples were pipetted out.

As is clear from **Fig. 55**, the PL intensity of emission of the samples pipetted out after 20s, 30s and 45s after Se addition are nearly the same. The samples pipetted out after these times showed no meaningful PL emission. The range of emission of these samples was between 500 and 550 nm.

The Absorption and Excitation spectra of the QTPs are shown below in **Fig. 56** and **Fig. 57**.

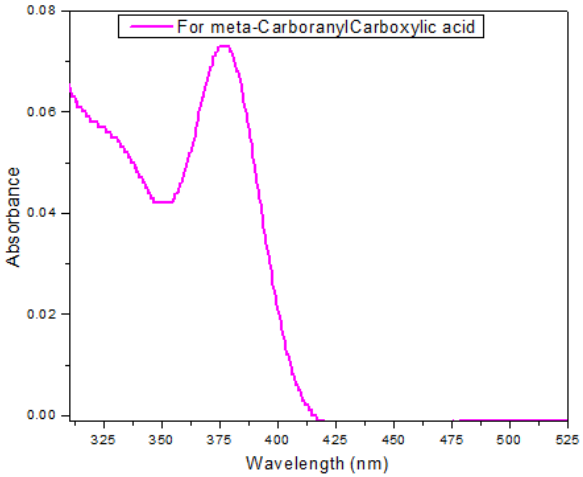

Figure 56. Absorption spectrum of QTPs. Absorbance was observed around 360 nm.

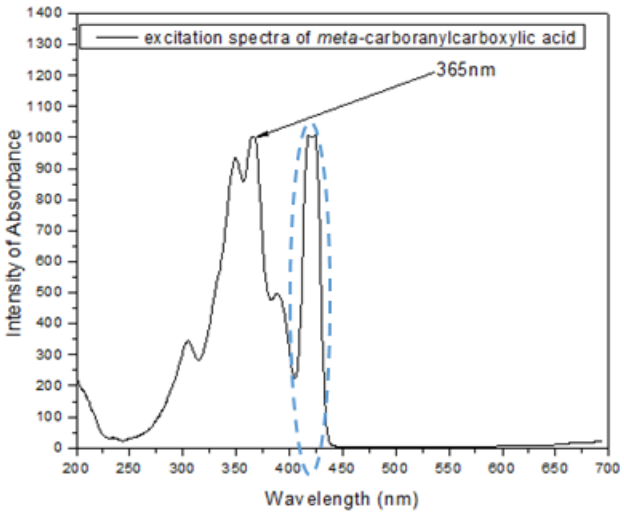

Figure 57. Excitation spectrum of QTPs. The excitation spectrum showed maximum excitation at 377nm. The diffraction grating is highlighted in blue.

As with the other QNCs produced by capping with carboranyl ligands, there is a dissonance between the Absorption and Excitation spectrum. The Quantum Yield was calculated using the method described previously and was found to be 58%.

3.5 Comparison with Organic ligand

To substantiate the relevance of the carboranyl ligands in the formation of QNCs it was considered appropriate to compare the carboranyl ligands with adamantanethiol by using the same conditions of synthesis as those leading to that of the novel QNCs. The result was the formation of QDs with a weak fluorescence and the TEM showed an agglomeration of dots, which was vastly different from the QDs formed using carboranyl ligands that give well dispersed and homogenous QDs. There was no appearance of either QR_{ods} or QRs or QTPs, hence illustrating the necessity of the carboranyl ligands in producing these novel structures. The results were the same with and without incorporating the temperature ramp, as illustrated by the **Fig. 58**.

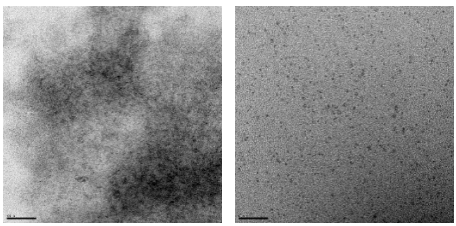

Figure 58. TEM images of QDs produced by 1-Adamantane thiol are shown here. The image on the left shows QDs produced without the temperature ramp. And the image on the right shows QDs are produced even when temperature ramp is done. No other QNCs were observed with temperature ramp using 1-Adamantane thiol.

3.4.4 Conclusions

In this work, it was reported the ease with which different QNCs can be generated in a one-step colloidal synthesis using carboranyl ligands as capping agents. Each carboranyl ligand led to a different morphology in the quantum regime, all of which should a wide spectrum of PL emission colors when excited by UV light and high Quantum Yields. These are summarized in the table below.

Name of ligand	Quantum Nanocrystal generated	Range of PL emission colors	Quantum Yield
meta-carboranethiol	Quantum Dots	Blue to Yellow	77%
ortho-carboranethiol	Quantum Rods	Blue to Yellow	70%
meta-carboranedithiol	Quantum Rods	Shades of Yellow	50%
1-methyl-*ortho*-2-carboranethiol	Quantum Rings	Blue to Yellow	57%
meta-carboranephosphinic acid	Quantum Rings	Blue to Yellow	44%
meta-carboranediphosphinic acid	Quantum Rings	Blue to Yellow	40%
meta-carboranecarboxylic acid	Quantum Tetrapods	Green and Yellow	48%

Table 1. Summary of QNCs generated, their PL emission and Quantum Yield.

The reported procedure does not require the synthesis of any intermediate structures; it is only based on the use of spherical carboranyl ligands that by means of a coordinating site binds to the cadmium to generate the

QNCs of CdSe composition. The key to producing these QNCs, i.e, the carboranyl ligands are based on icosahedral carboranes of formula $C_2B_{10}H_{12}$. The compact packing of spheres, their size near 0.6 nm, and the hydrophobicity are the key points that explain the formation of these novel QNCs. A temperature ramp for final 40-45^{o}C was also essential for the formation of the QNCs; without it only QDs are generated. Most of the carboranyl ligands studied in this work only produce QDs without the sudden temperature ramp, but these ligands produce other QNCs when the temperature ramp is incorporated. A possible explanation for this is that nanobubbles are generated due to the sudden temperature rise, which acts as a template for the growth of QNCs.

The method reported in this work is the first such method that allows for tuning morphologies in the Quantum regime, all the while using a simple one step colloidal synthesis. This led to the formation of the extremely rare Quantum Tetrapods and their curious property of changing color of PL emission as they age over time. This method can also be used to generate Quantum Rings and Quantum Rods in large quantities using a simple chemical synthesis, something that has not been achieved so far, thus allowing for the many fascinating properties of these novels QNCs to be studied in detail and to be used for real life applications.

3.4.5. References

1. A.P. Alivisatos., *Science*, **271** (1996) 933-937.
2. S. J. Lim et al., *Nat. Commun*., **6** (2015) 8210.
3. P. V. Kamat., *J. Phys. Chem. C*, **112** (2008) 18737-18753.
4. M. K. Choi, J. Yang, T. Hyeon, D. H. Kim, *npj Flex. Electron.*, **2** (2018) 10.
5. D.V. Talapin, C.B. Murray, *Science*, **310** (2005) 86-89.
6. V. I. Klimov et al., *Science* **290** (2000) 314-317.
7. T. Jamieson et al., *Biomaterials*, **28** (2007) 4717-4732.
8. P. Wu, X. P. Yan, *Chem. Soc. Rev.*,**42** (2013) 5489-5521.
9. S. Zhou, M. Shao, S. T. Lee., *ACS Nano* **6** (2012) 1059-1064.
10. A. P. Alivisatos., *Nat. Biotechnol*., **22** (2004) 47-52.
11. R. C. Somers, M. G. Bawendi, D. G. Nocera, *Chem. Soc. Rev*. **36** (2007) 579–591.
12. L. Cui, X. P. He, G. R. Chen, *RSC Adv.* **5** (2015) 26644–26653.
13. L. Liu et al., *J. Am. Chem. Soc.* **131** (2009) 16423–16429.
14. A. P. Alivisatos, W. Gu, C. Larabell, *Annu. Rev. Biomed. Eng*. **7** (2005) 55–76.
15. J. Weng, J. Ren, *Curr. Med. Chem.*, **13** (2006) 897–909.
16. X. Michalet et al., *Science*, **307** (2005) 538.
17. S. Jin, Y. Hu, Z. Gu, L. Hiu, H. C. Wu, *J. Nanomater*., **2011** (2011) 1.
18. N. A. Bakar et al., *Semiconductor Eletronics*, 2008 ICSE, 2008 IEEE Int. Conf., 2008.
19. X. Peng, et al., *Nature* **404** (2000) 59–61.
20. E. M. Chan, R. A. Mathies, A. P. Alivisatos, *Nano Lett.* **3** (2003) 199–201.
21. L. Li, J. Hu, W. Yang, A.P. Alivisatos, *Nano Lett.* **1** (2001) 349–351.
22. J. Hu et al., *Science* **292** (2001) 2060–2063.
23. A. Shabaev, A. L. Efros, *Nano Lett.* **4** (2004) 1821–1825.
24. H. Htoon, J. A. Hollingworth, A. V. Malko, R. Dickerson V. I. Klimov, *Appl. Phys. Lett.* **82** (2003) 4776–4778.
25. A. Lorke et al., *Phys. Rev. Lett.* **84** (2000) 2223-2226.
26. E. Rothenberg, M. Kazes, E. Shaviv, U. Banin, *Nano Lett.* **5** (2005) 1581–1586.

27. S. N. Raja et al., *Nano Lett.* **13** (2002) 3915–3922.
28. A. Wolcott, R. C. Fitzmorris, O. Muzaffery, J. Z. Zhang, *Chem. Mater.*, **22** (2010) 2814–2821.
29. A. E. Saunders, F. Shieh, B. A. Korgel, *J. Phys. Chem. B.* **109** (2005) 8538–8542.
30. K. Manthiram, B. J. Beberwyck, D. V. Talapin, A. P. Alivisatos, J. Vis. Exp. **82** (2013) 50731.
31. C. Tong, S. Yoon, L. Wang, *Nanoscale Res. Lett*., **7** (2012) 520.
32. V. E. Demidov et al., *Phys. Rep*., **673** (2017) 1–31.
33. A. Fuhrer et al., *Nature*., **413** (2001) 822–825.
34. W. C. Tan, J. C. Inkson, *Phys. Rev. B - Condens. Matter Mater. Phys*., **60** (1999) 5626–5635.
35. V. I. Klimov et al., *Nature*, **447** (2007) 441–446.
36. G. O. De Sousa, D. R. Da Costa, A. Chaves, G. A. Farias, F. M. Peeters, *Phys. Rev. B*, **95** (2017) 20514.
37. L. L. Li, D. Moldovan, P. Vasilopoulos, F. M. Peeters, *Phys. Rev. B*, **95** (2017) 205426.
38. D. R. Da Costa, A. Chaves, W. P. Ferreira, G. A. Farias, R. Ferreira, *J. Phys. Condens. Matter*, **29** (2017) 165501.
39. A, Lorke et al., *Microelectron. Eng.* **47** (1999), 95–99.
40. A, Lorke et al., *Phys. Rev. Lett.* **84** (2000) 2223–2226.
41. R. J. Warburton et al., *Nature* **405** (2000) 926–929.
42. M. Bayer et al., *Phys. Rev. Lett.* **90** (2003) 4.
43. C. Somaschini, S. Bietti, S. Sanguinetti N. Koguchi, A. Fedorov, Nanotechnology **21** (2010)125601.
44. C. Somaschini, S. Bietti, N. Koguchi, S. Sanguinetti, *Nanotechnology* **22** (2011) 185602.
45. I. Fedin, D. V Talapin, *J. Am. Chem. Soc.*, **138** (2016), 9771–9774.
46. K. D. Gilroy, A. Ruditskiy, H. C. Peng, D. Qin, Y. Xia, *Chem. Rev*., **116** (2016) 10414–10472.
47. A. M. Cioran et al., *J. Am. Chem. Soc.,* **134** (2012) 212–221.
48. A. Saha, E. Oleshkevich, C. Vinas, F. Teixidor, *Adv. Mater.*, **29** (2017) 1704238.
49. L. A. Paquette, R. J. Ternansky, D. W. Balogh, G. Kentgen, *J. Am. Chem. Soc.* **105** (1983) 4446–4450.
50. J. Poater. M. Solà, C. Viñas, F. Teixidor, *Angew. Chemie - Int. Ed.* **53** 2014, 12191–12195.

51. J. Poater, M. Solà, C. Viñas, F. Teixidor, *Chem. - A Eur. J.*, **22** (2016) 7437–7443.
52. R. N. Grimes, *Carboranes*, 3rd Ed.; Elsevier: Oxford, 2016.
53. C. Viñas, R. Benakki, F. Teixidor, J. Casabó, *Inorg. Chem.*, **34** (1995) 3844–3845.
54. E. Oleshkevich, F. Teixidor, D. Choquesillo-Lazarte, R. Sillanpää, C. Viñas, *Chem. - A Eur. J.*, **22** (2016) 3665–3670
55. M. Fontanet et al., *Chem- A Eur. J.*, **17** (2011) 13217-13229.
56. C. A. Ubani, S. M. Yusof, *J. Mod. Educ. Rev.*, **1** (2011) 63–73.
57. W. J. Baumgardner, Z. Quan, J. Fang, T. Hanrath, *Nanoscale*, **4** (2012) 3625.
58. M. Grabolle et al., *Anal. Chem.*, **81** (2009) 6285.
59. P. Taylor, *Nucleosides Nucleotides & Nucleic acids*, **26** (2007) 1611–1613.
60. Y. Endo et al., *Chem. Biol.*, **8** (2001) 341–355.
61. T. Mokari, E. Rothenburg, I. Popov, R. Costi, U. Banin, *Science.*, **304** (2004) 1787-1790.
62. L. Manna, D.J. Miliron, A. Meisel, E.C. Scher, A.P. Alivisatos, *Nat. Mat.*, **2** (2003) 382-385.

3.5. Carboranes in Conjunction with Gold and Magnetic Nanoparticles for potential use in Biomedical Applications

Spherical carboranyl derivatives capped gold nanoparticles showed unique phase transfer properties. Further, H[COSAN] was attached to gold coated magnetic nanoparticles designed for use in sensing layer of a Point of Care device for heart failure diagnosis.

Abhishek Saini
ICMAB-CSIC (UAB)

CONTENTS

3.5.1 Introduction

3.5.1.1 Carboranyl Thiol capped Gold nanoparticles

Gold nanoparticles (Au NPs) are amongst the most investigated nanoparticles, due to their use in a myriad of applications. [1-4] The fact that makes them so attractive is that their surface and core properties can be manipulated for different applications. Thiol stabilized gold nanoparticles have been known to show great stability and dispersibility in nonpolar solvents. [5-8] These nanoparticles have found use in application such as development of artificial nose-type gas sensors with potential applications in lung cancer diagnostics based on breath analysis. [9-11] They have also been used for biomedical applications such as drug and gene delivery. [12-14]

Vinas and co. had demonstrated that Au NPs capped with *ortho*-carboranethiol showed phase transfer properties, being able to travel from aqueous to organic phase by behaving as a Henglein-type electron pool. [15] This unique property was found to be due to the presence of *ortho*-carboranethiol clusters as capping agents, which, like other thiol ligands, effectively stabilize the gold core, but owing to their spherical shape necessarily leave gaps that allow direct access of reactants and solvent molecules to the gold surface. [15] These *ortho*-carboranethiol capped Au NPs showed cellular uptake properties, hence making them ideal for use in biomedical applications. The phase transfer property was demonstrated by using HCl as an oxidising agent, but the use of other cations was not

explored. This acted as the motivation for this particular work, where different cations were used to demonstrate this phase transfer property of *ortho*-carboranethiol capped Au NPs.

3.5.1.2 Gold coated magnetic nanoparticles

The second part of this chapter deals with the synthesis of gold coated magnetic nanoparticles decorated with amine and cobaltabis(dicarbollide) for use in a Point of Care (POC) device for early diagnosis of heart failure.

Magnetite (Fe_3O_4 NPs) are the most common magnetic materials which are extensively studied in nano-dimension. They are often referred to as SPIONs (Super Paramagnetic Iron Oxide Nanoparticles) as they show superparamagnetic properties due to their size. Commonly used MNPs are usually within the dimension of 5-20nm as magnetite usually have single domains within this size range. Magnetic nanoparticles have been studied extensively for use in nanomedicine and biosensing materials for many decades. [16] Despite their enormous potential, these materials face problems for actual real-life applications as active elements in sensing materials. This is due to their low electrical conductivity and limited optical properties which reduces their effectiveness as transducing elements in a sensor.[17] Their large surface area to volume ratio and low surface charge at neutral pH also causes dispersions of these particles to be unstable with the magnetic nanoparticles tending to aggregate when dispersed in solvents.[18]

Coating the magnetic nanoparticles with gold layer solves all of the aforementioned issues such as conductivity,[19] optical properties (localized surface plasmon resonance and surface enhanced Raman scattering), [20] biocompatibility,[21-22] bioaffinity through functionalization of amine/thiol terminal groups,[23] and chemical stability by protecting the magnetic core from aggregation, oxidation and corrosion.[24] Gold coated magnetic nanoparticles (MNP@Au) can be used for a wide variety of applications due to their versatility. The optical and magnetic properties of these particles can be tuned by changing their size, gold shell thickness, shape, charge, and surface modification.

This chapter is now divided into 2 sections, the first detailing the synthesis and characterization of the Au nps capped with *ortho*-carboranethiol and exploring their phase transfer properties. The second part of this chapter will deal with the synthesis and characterization of the MNP@Au decorated with amine and cobaltabis(dicarbollide), referred to as H[COSAN] in this chapter.

3.5.2 Experimental Procedures and Results

3.5.2.1 Phase transfer properties of *ortho*-carboranethiol capped Gold nanoparticles

3.5.2.1.1 Synthesis of *ortho*-carboranethiol capped Gold nanoparticles

The *ortho*-carboranethiol capped gold nanoparticles were synthesized using the procedure followed by Cioran et al. It is summarized briefly below:

50 mg of *ortho*-carboranethiol (0.283 mmol) and 111 mg of chlorauric acid ($HAuCl_4$) (0.283 mmol) were dissolved in 60 mL of methanol and 64 mg of sodium borohydride (1.6998 mmol) was dissolved in 30 mL of methanol. Both these solutions were mixed under vigorous stirring. The mixture was stirred at room temperature for 10 min before the solvent was removed by rotary evaporation. The dark-brown residue was thoroughly washed with diethyl ether to remove excess *ortho*-carboranethiol and then dissolved in isopropanol to remove the remaining sodium borohydride and other insoluble contaminants. Finally, the remaining product was dried under vacuum before use.

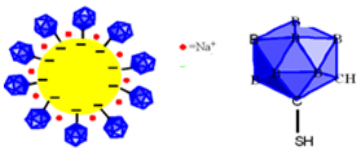

Figure 1. Gold nanoparticles capped with *ortho*-carboranethiol.

3.5.2.1.2Phase transfer of *ortho*-carboranethiol capped Gold nanoparticles

To perform the phase transfer, the first cation chosen was Fe^{3+}. It was theorized that upon coming in contact with the Au nps, the Fe^{3+} will get reduced to Fe^{2+} and act as an oxidizing agent for the Au nps, thus facilitating their transport from the aqueous phase to the organic phase.

To this end, a 1M aqueous solution of $Fe(III)Cl_3$ was prepared. Meanwhile, in a vial, 10 mg of *ortho*-carboranethiol capped Au NPs were dispersed in 3 ml water. To the same vial, 3 ml of Diethyl ether was added to form a two-phase system with the Au NPs dispersed in the aqueous phase at the bottom of the vial. Upon the dropwise addition of around 1 ml of the aqueous $FeCl_3$ solution interspersed with shaking to provide kinetic energy, it was observed that the Au nps transfer from the aqueous phase at the bottom of the vial to the ether phase at the top of the vial.

The aqueous part was then removed from the vial and a 0.1M aqueous solution of $NaBH_4$ was added dropwise, which led to the transfer of the Au NPs back into the aqueous phase. This reversible phase transfer process has been depicted below in **Fig. 2**.

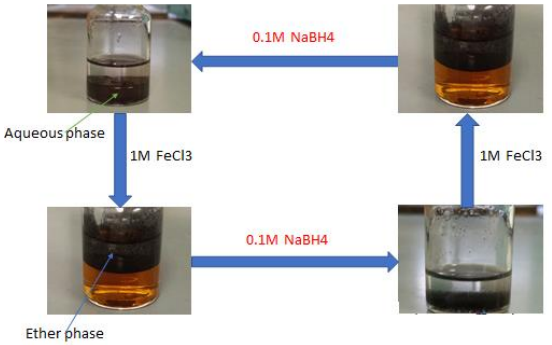

Figure 2. The transfer of the *ortho*-carboranethiol capped Au NPs facilitated by $FeCl_3$ and $NaBH_4$

This phase transfer of the Au NPs can be explained by the schematic below in **Fig. 3**

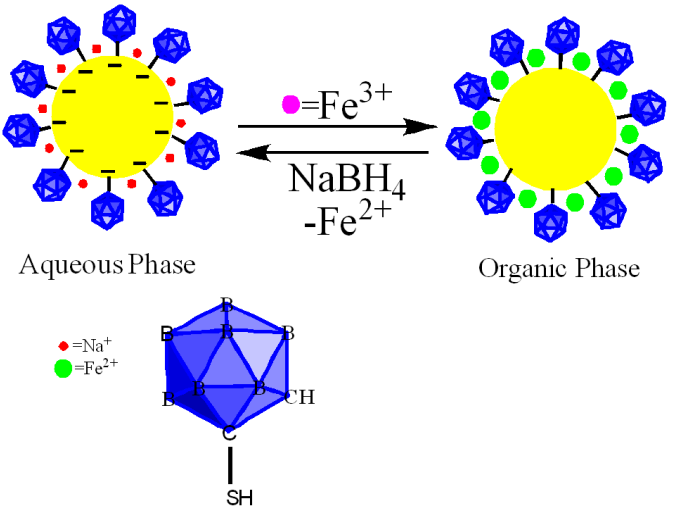

Figure 3. Scheme for the transfer of the *ortho*-carboranethiol capped Au NPs facilitated by $FeCl_3$ and $NaBH_4$

The *ortho*-carboranethiol capped Au NPs are ion pools that can store electrons in the core of Au and positive ions in the voids formed by the carborane clusters. These NPs when oxidized using dilute HCl, lose the electrons from the gold core along with the evolution of the hydrogen gas. Also, the sodium ions desorb and the particle becomes less hydrophilic and precipitates in the aqueous phase but is soluble in organic solvents like ether and is extracted in the ether phase. The uniqueness of these NPs lies in the fact that these can be made water soluble again by adding sodium borohydride, which due to the voids produced can reach the core and charge it by direct access and the sodium ions are trapped in the voids which compensate the negative charge of the core. This charged particle is water soluble which when discharged is soluble in an organic phase, thus proving that it is a redox procedure and not an acid/base reaction. This effect in the Au NPs is brought over because of the spherical capping of the carborane ligands. This has also been proved by using molecular stoppers. In that case, after the Au NPs were in organic phase, a molecular stopper was introduced. After that when sodium borohydride was added to revert the solubility of these NPs into aqueous phase, it was not possible to do so. This is because the molecular stopper had blocked the voids and hence the metal core could not be charged by direct access of the reducing agent and hence it could not be made water soluble. Using this concept, we tried to utilize these NPs to store other ions in the voids generated by the carborane ligands. In the case shown in **Fig. 3**, the initial Au NPs are water soluble which contains the Na^+ ions in the voids. Then, we add Fe^{3+} ions to oxidize the core and NPs, which

in turn reduces the Fe^{3+} to Fe^{2+} and these get trapped into the voids. This NP is now soluble in the ether phase. The salt used for this procedure was $FeCl_3$. While when sodium borohydride is added again in order to revert its solubility, then the same thing happens as explained before, that the metal core is negative charged by the reducing agent due to direct access, and the Na^+ ions are trapped into the voids and the Fe^{2+} ions are expelled from the voids. This makes the Au NPs water soluble again. This phenomenon helps us to obtain Au NPs which can act as charge transporters or charge carriers. Also, the presence of ions makes the Au NPs generate potential across membranes which can facilitate the transport of these particles across the membranes in biological systems. Different ions can be trapped into the voids of these NPs and transported across the membranes. The size of the voids is smaller and are around 0.25nm as estimated, so the ions to be transported need to be smaller ions. Already Na^+ and K^+ ions being transported across the membranes have been reported by our group, though Mg^{2+} ions could not be transported due to their larger charge.[27] Nevertheless, this opened up a new avenue for investigation using these unique Au NPs. Noticeably since the divalent ion of Mg could not be trapped inside the voids while the monovalent ions could be, does raise the question as to how can Fe^{2+} be trapped inside the voids. To study this further and see whether indeed iron ions were trapped inside the void or formed a layer of ions surrounding the monolayer capped Au NPs. Firstly, we tried to characterize the Au NPs with Fe^{2+} in ether phase using Infra-red spectroscopy (IR). In the IR we could see the peak of the B-H stretching clearly at around $2517cm^{-1}$.

This confirmed the presence of the *ortho*-carboranethiol cluster acting as the capping ligand for these NPs and there was no change in the structural feature of the NPs. The IR spectrum is given below.

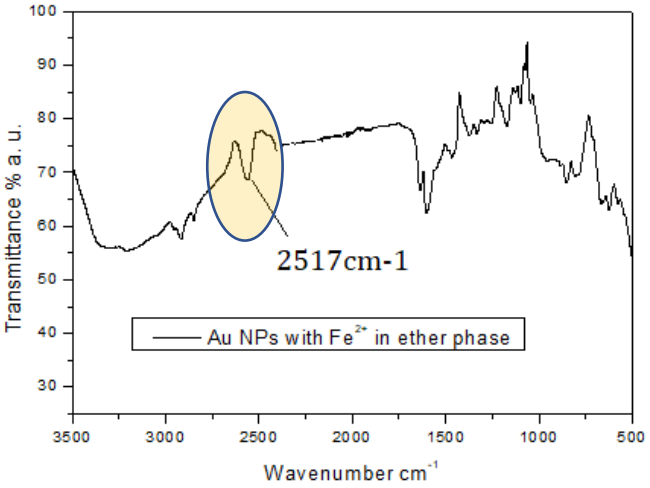

Figure 4: IR Spectrum of Au NPs with Fe^{2+} in ether phase. It shows the B-H band at 2517cm^{-1}.

In order to study this further we did the Elemental mapping to observe the coverage of the iron ions and the Au NPs as well as the ratio of the Fe to Au in the sample. In the elemental mapping, it was observed that the iron ions covered most of the surface of the carborane capped Au NPs. The map clearly shows that the Fe^{2+} ions are present in excess above the Au NPs as seen in **Fig. 5.**

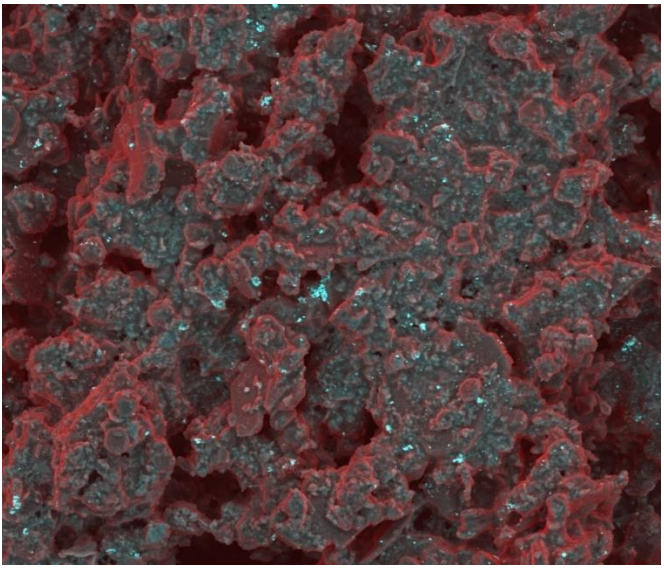

Figure 5: Elemental mapping of Au NPs with Fe^{2+}. Fe is shown in red and Au is shown in blue.

Since there is so much of iron ions covering the surface it can be hypothesized that the iron ions are not trapped inside the voids but are on the surface close to the carborane ligands. When the Fe^{3+} is added, they oxide the core probably by direct access to the metal core and get reduced to Fe^{2+} and expel the Na^{+} from the voids. This necessarily does not mean that the Fe^{2+} get trapped within those voids as had envisaged before and remain there. But instead they might just be floating around the channels created by the close packing of the spherical carborane ligands. Hence, they are closer to the surface of the coated NPs and consequently more prominently visible in the mapping and on top of the NPs.

Furthermore, we also did Energy Dispersive X-ray (EDX) to quantify the amount of Au and Fe in the sample (**Fig. 6**).

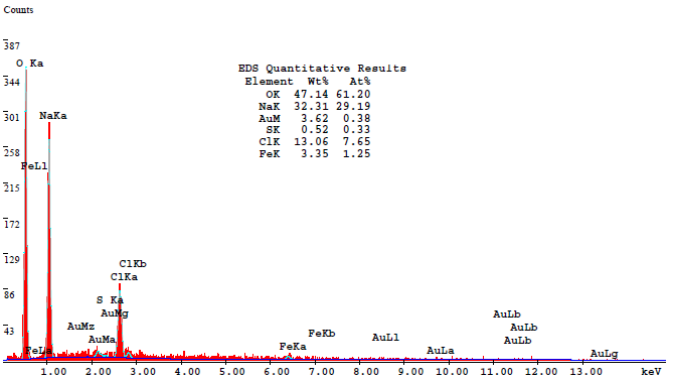

Figure 6: EDX Spectrum of the Au NPs with Fe^{2+} in ether phase.

Here we can clearly see that the amount of Fe is larger than Au in the sample. It is deduced that the ratio of Au:Fe is almost 1:3.5. This clearly supports the hypothesis that perhaps the Fe ions are not trapped within the voids due to their smaller size but they are present near the surface of the channels formed by the ligands and hence they are in excess when compared to the Au core of the sample. The ratio of Au: S was 1.15:1, the S was a little less than the Au, which is to be expected since the S is only bonded to the outer layer of the Au, and not the complete Au core. The presence of Cl is also important and will be elaborated upon later. Using the EDX data we did some calculations on the surface coverage of the S on the Au core. Using the geometrical square packing of sphere on a sphere we did these calculations. The core of Au is the sphere upon

which the spherical carboranyl ligands are closely packed in a square packing was assumed.

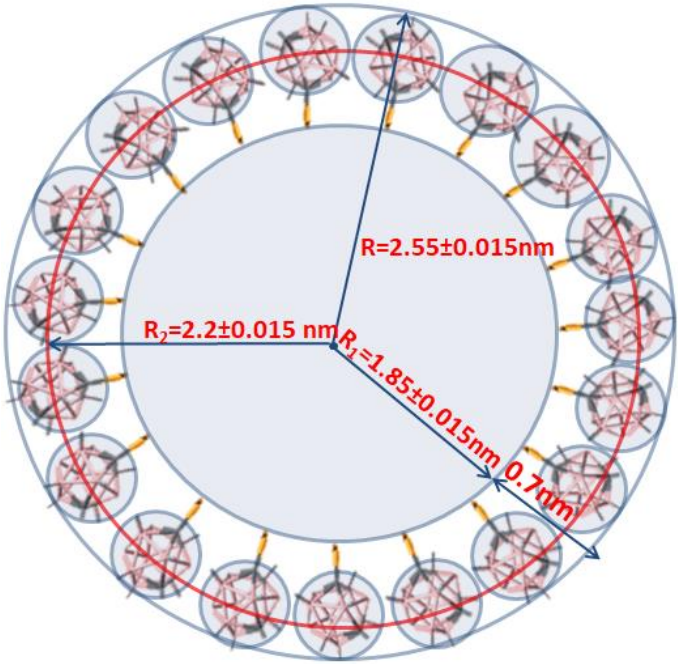

Figure 7. Dimensions of Au NPs capped with *ortho*-carboranethiol.

Geometry calculations: At first, we did an estimation of how many carboranyl thiols can cover the surface of the Au core, considering the Au core and the carborane cluster as ideal spheres, and that the carborane clusters have a square packing onto the surface of Au core.
Dimensions of *ortho*-carboranylthiol was measured from its crystal structure, and determined as 0.5 nm ($Ø_{carbSH}$) as the diameter for carborane cluster "sphere" and 0.7 nm (L) in length including the sulphur group. The diameter of the core of Au NPs was found subtracting the two lengths of

ortho-carboranethiol ligand, 2L, from mean diameter of Au NPs found by TEM (5.1± 0.03 nm as seen in **Fig. 9**) ,
$Ø_{TEM}$ = 5.1 ± 0.03 nm, which resulted to 3.7 ± 0.03 nm. It was considered as $Ø_1$.
So R_1= $Ø_1$/2, R_1= 1.85 ± 0.015 nm;
Now, $Ø_2$ = [Diameter of the whole Au NPs capped with *ortho*-carboranethiol] – [Diameter of the carboranyl sphere]
So, $Ø_2 = Ø_{TEM} - 2(L\text{-}1/2Ø_{carbSH})$ = 4.4 ± 0.03 nm, So, R_2= $Ø_2$/2=2.2 ± 0.015 nm.
Now in order to calculate the surface area we need to use the formula for surface area of sphere which is $4\pi r^2$.
$A_2 = 4\pi R_2^2$ = 61.641 ÷ 59.983 nm² (60.81 ± 1.658 nm²)
A_2 is the surface area of the core. For square packing we need to calculate the area of carboranyl thiol.
$A_{carbSH} = Ø_{carbSH}^2$= 0.5 x 0.5= 0.25 nm²
n_{max} (maximum number of CarbSH that can cover the surface of the Au Core with a diameter of 3.7 ± 0.03nm) = A_2/A_{carbSH}= 246.564 ÷ 239.932 (243.24 ± 6.632)
Now, in order to determine the surface coverage values from EDX results we do the following calculations:
Surface calculations: We already know the At % ratio of Au:S is 1.15:1 from the EDX results. Now from the geometrical calculations we know the exact diameter (d) of the Au core is 3.7 ± 0.03nm. So, the mass of the core is calculated from here (m_{Au})
$m_{Au} = (1/6)\pi d^3 \varrho_{Au}$ (where d is the diameter of the Au core and ϱ is the true density of Au NPs)
m_{Au}= (1/6) x 3.141 x (3.7 ± 0.03)³ x 19.32 g/cm³= (51.24 ± 1.24)E-20g
$Mole_{Au} = m_{Au}/M_{Au} = N_{Au}/N_A$, where M_{Au} is the molecular weight of Au which is 196 g/mol, N_{Au} is the number of Au units that contains one NP core with the diameter of 3.7 ± 0.03nm and N_A is the Avogadro number.

So now, $N_{Au}=m_{Au} \times N_A/M_{Au}= 157.4 \pm 38$

Now taking into account the ratio obtained in the EDX spectrum for Au:S as 1.15:1, each nanoparticle bears $n_{carbSH} = N_{Au}/1.15= 136$ (ignoring the error factor)

Therefore, from here the saturation of the surface of the Au core with CarbSH in terms of % can be calculated with respect to the maximum number of CarbSH that we estimated from the geometrical calculations.

$S_{carbSH}= n_{carbSH}/n_{max} \times 100\%= 64.7\%$ (ignoring the error factor).

So by these calculation we can deduce an approximate surface coverage % of the carboranyl thiols on the Au core of 3.7 ± 0.03nm diameter. The coverage is approximately 65%.

Though the above characterizations prove the presence of iron in the sample, it was important to see whether there was reduction in the iron from Fe^{3+} to Fe^{2+}. To quantify the reduction in the iron ions we did the X-ray photoelectron spectroscopy (XPS). In this we isolated the NPs in ether phase again and studied the dried, powdered sample. The XPS analysis was performed in a Phoibos 150 analyzer (SPECS GmbH, Berlin, Germany) under ultrahigh vacuum conditions (base pressure 4×10^{-10} mbar) with a monochromatic aluminium K alpha X-ray source (1486.74 eV). The energy resolution as measured by the fwhm of the Ag 3d5/2 peak for a sputtered silver foil was 0.8 eV. In this we could clearly see the peak of Fe^{2+} at 710.5eV. It confirmed that there was a reduction of the Fe^{3+} ions to Fe^{2+} ions and that the core which initially had negative charges was oxidised and hence it was no longer soluble in water and could be transferred to the ether phase (organic phase).

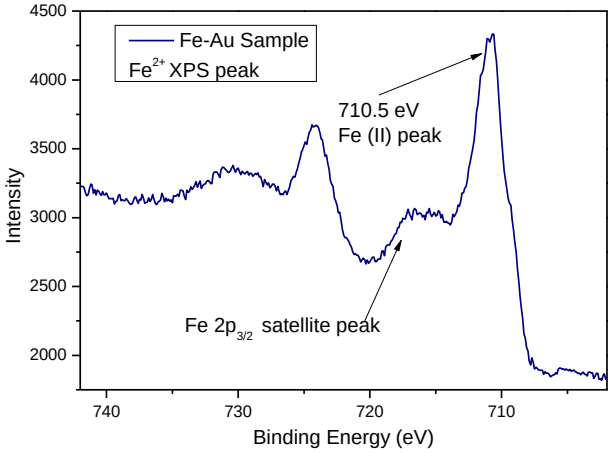

Figure 7: XPS of Au NPs in ether phase having Fe^{2+} in them.

Also, to quantify the size, the TEM analysis was done of these NPs. The size of the NPs in ether phase having been oxidised had increased when compared to the size of the NPs in the water phase. This is probably due to the presence of an additional layer of Fe^{2+} ions near the surface of the NPs. This further confirms that the size had indeed increased after the addition of the Fe^{3+} ions to the water phase NPs to transfer them to ether phase. The images of Transmission electron micrographs are given below in **Fig. 9** and **Fig. 11**. A total of over 200 nanoparticles were manually measure using the ImageJ software and the histogram was plotted. Then, using the Gaussian function, the mean size was calculated. The mean size of the particles initially synthesized (dispersed in water) was 5.1nm with very minor error of 0.03nm. This showed that the NPs were quite monodispersed and had a very uniform distribution of size even being synthesized in a colloidal method. The histogram is shown in **Fig. 10**.

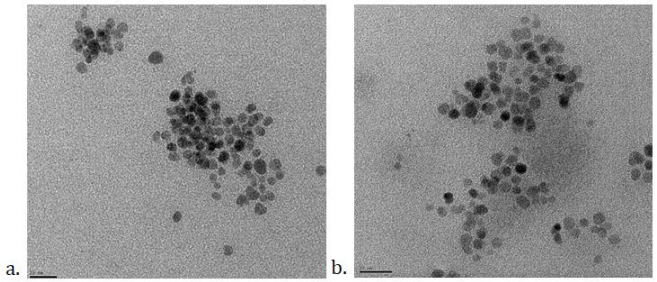

Figure 9: TEM images of Au NPs capped with *o*-mercaptocarborane (in aqueous phase). It shows quite monodispersed particles.

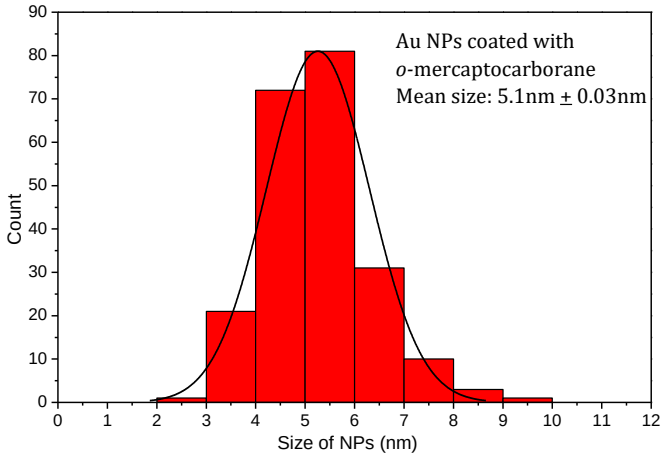

Figure 10: Gaussian Size graph of the Au NPs capped with *o*-mercaptocarborane. Mean size: 5.1nm ± 0.03nm.

The mean size of the NPs in ether phase with the Fe^{2+} was measured the same way from the TEM images and the size had considerably increased and was 9.5nm with an error of 0.046nm. It was again very monodispersed, even though the size had increased. The gaussian size histogram is shown in **Fig. 12**.

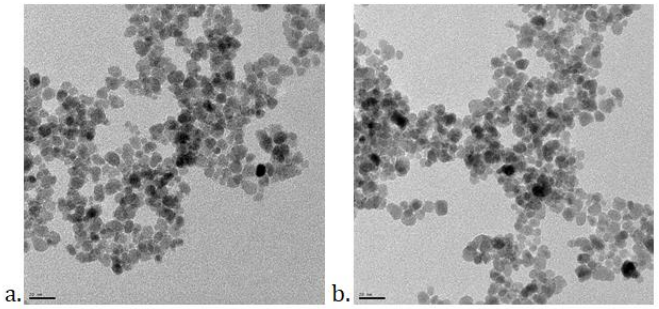

Figure 11: TEM images of Au NPs capped with *o*-mercaptocarborane with Fe^{2+} in ether phase. It shows quite monodispersed particles.

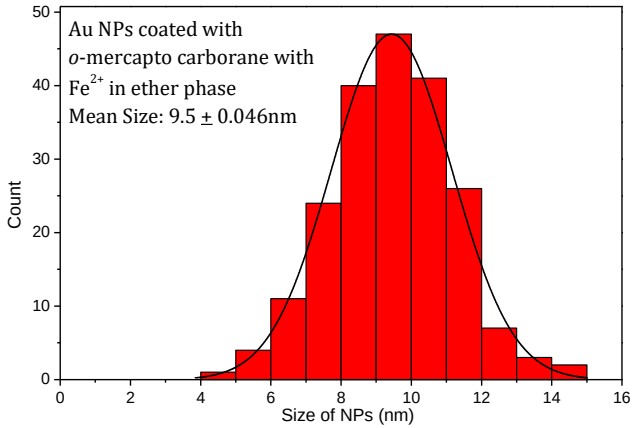

Figure 12: Gaussian Size graph of the Au NPs capped with *o*-mercaptocarborane with Fe^{2+} in ether phase. Mean size: 9.5nm ± 0.046nm.

For the size calculations, the image of the TEM were measured in the same scale of 20nm in both cases. Also, in order to confirm that the core was of Au NPs, the selected area diffraction pattern was done on the sample in the TEM grid. The diffraction rings were very clearly visualized and the miller indices were assigned to the rings and they matched the miller indices of Au metal.

This electron diffraction pattern was done for the sample obtained from the ether phase. It is shown in **Fig. 13**.

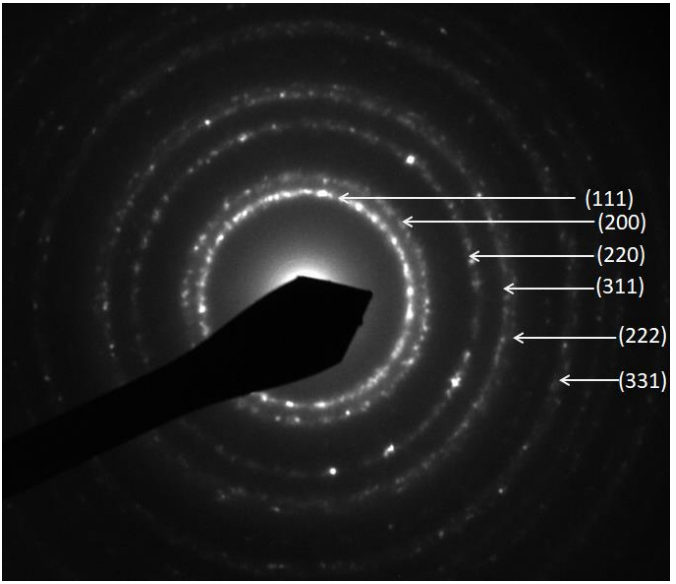

Figure 13: Selected area electron diffraction (SAED) was done to determine the composition of the core of the NPs in ether phase and they confirmed that the core was composed of Au metal.

Moreover, the initial Au NPs synthesized which were around 4-5nm inn diameter, did not show any plasmon peak in the UV-vis absorbance but the NPs with Fe^{2+} showed a tiny absorbance peak in between 514nm to 550 nm, which is characteristic of Au NPs. Usually as mentioned in the paper by Vinas and co., the Au NPs having smaller dimensions of around 3-4nm do not show any plasmon peak in the UV-vis absorbance spectrum. Since the size increased to almost 10nm when the Au NPs were transferred to the ether phase by the addition of Fe^{3+} ions to oxidize them, we did a UV-vis absorbance

measurement for these NPs, and we could see a small peak, which further corroborates the size increase as obtained by the TEM images. The UV-vis absorbance spectrum is shown in **Fig. 14**. In smaller NPs of Au the intensity of the peak gets damped due to the reduced mean free path of the electrons. [15] As the size of the nanoparticle increases the intensity of the peak grows. This comparison is shown in **Fig. 15**.

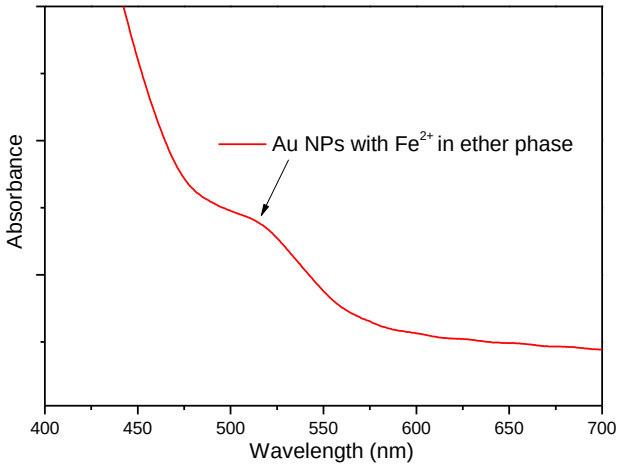

Figure 14: UV-vis spectrum of Au NPs with Fe ions in ether phase. Due to the increase in size of the NPs, there is an appearance of the plasmon peak of the NPs.

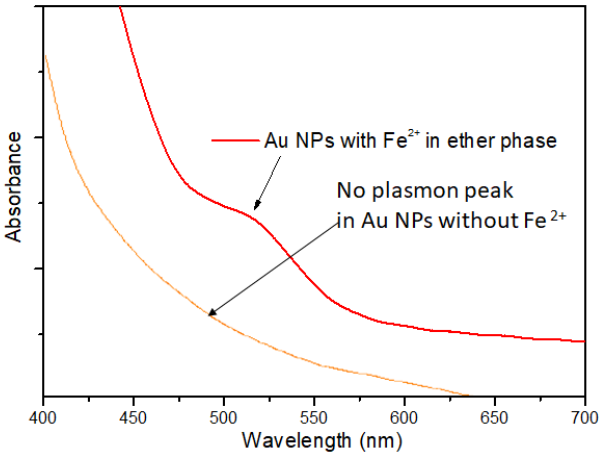

Figure 15: Comparison of the UV-vis Spectra of Au NPs with Fe ions in ether phase with Au NPs in water phase without the Fe ions.

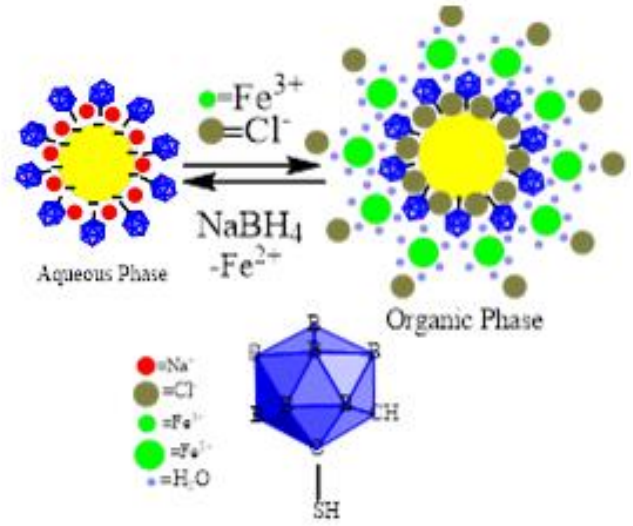

Figure 16: New model for divalent/trivalent/trivalent ions.

So, after obtaining the aforementioned results, we were compelled to modify the model we had initially hypothesized. It was clear that the Fe ions were surrounding the carborane capped Au NPs rather than filling the void positions created by the spherical shapes carboranes. The role of the Cl^- anion (present due to using $FeCl_3$ as an iron source) in this proposed model should not be underestimated. It is the presence of the Cl^- anion and its ionic interaction with the Fe^{2+} that anchors the Fe^{2+} in place and provides stability to this complex. This architecture and the importance of the Cl^- has already been hypothesized in CdSe QDs with a core canopy architecture. [arpita] **Fig. 16** (right) shows the image of the new model proposed for larger ions. The peripheral presence of the Fe and Cl ions is shown in the **Fig. 16** which is different to the positioning of the Fe ions within the voids as shown in **Fig. 3**. The presence of Fe^{2+} and Cl^- ions and being separated by a miniscule distance, makes these Au NPs as molecular capacitors. The presence of these charged anions and cations gives rise to the concept of the double layer capacitance. In this case, there are two layers of charge with opposing polarity, and are separated by a small layer of solvent molecules which acts as the dielectric material used in the normal capacitors, thus transforming these Au NPs as molecular capacitors capable of storing electric charge.

To further quantify the samples, we did Electron Energy Loss Spectroscopy (EELS) and analysed the sample using

Scanning Transmission Electron Microscopy (STEM). This was done to locate the B and the Fe in the samples. In STEM, it combines the advantage of TEM (good resolution) and SEM (3D structural image), along with the advantage of using high-angle annular dark field imaging technique (HAADF). The HAADF images can take bright field and dark field images, thus the contrast is better and it is easy to locate different components in the sample. In the STEM image shown in **Fig. 17**, we can clearly see that the Au NPs are small and are covered on top with carborane thiol moieties and Fe is present closer to the carborane clusters rather than the surface of the Au NPs.

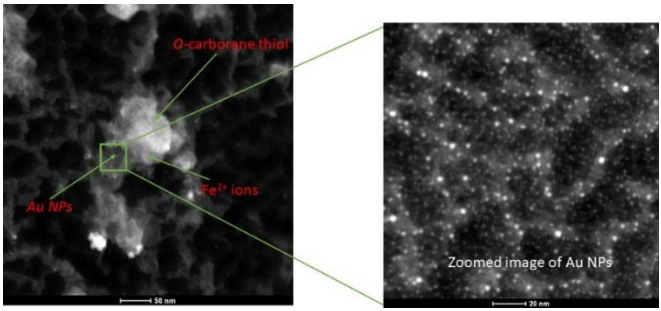

Figure 17: STEM image of Au NPs with Fe^{2+} ions in ether phase. It shows the placement of the Carborane cluster, Fe ions and the Au NPs. The right side showed the zoomed image of the Au NPs.

We further analysed the region marked in the **Fig. 17** as carborane and Fe with EELS to check the presence of Boron and EDX to find Fe. We could clearly observe the peak of Boron in EELS. While the EDX spectrum clearly showed that the peak of Fe was visible thus indicating the positioning of them within the sample. EELS was done for B while EDX was used for Fe because B is a light element and it is difficult to detect light elements using the EDX as

they produce weaker signals. This is because when the samples are ionized, the weaker element emit longer wavelengths of X-ray which can easily get absorbed within the sample and cannot be detected. While the heavier elements emit shorter wavelength X-rays which can be easily detected by the detector. The EELS and the EDX is shown from the area and we can clearly see B and Fe in them but not Au as this is covered by them.

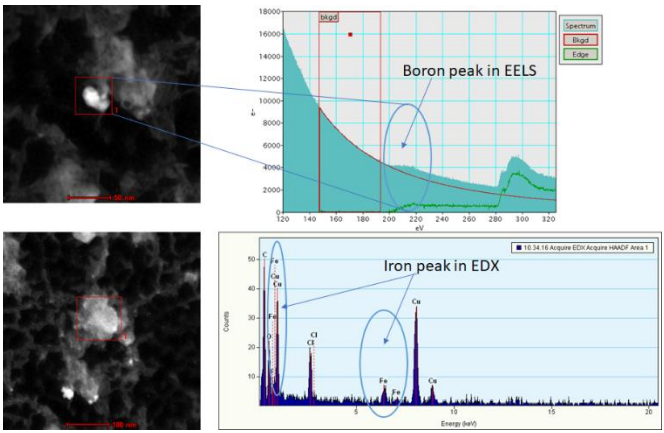

Figure 18: STEM images with EELS spectrum for B and EDX spectrum for Fe.

After this, we analysed the portion where we found the Au NPs in the STEM image and did an EDX on the area there, and we could clearly observe the presence of Au there on the sample. Different energies of Au were detected by the EDX analysis. The spectrum and the region are shown in **Fig. 19**. The Au NPs in these were of the same size as mentioned above, which is around 9-10nm.

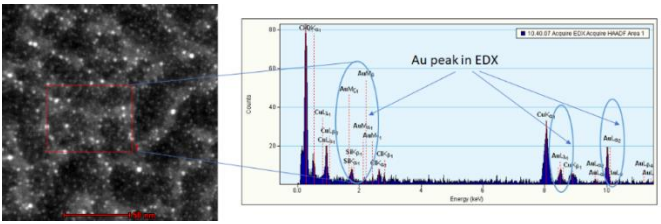

Figure 19: STEM image of Au NPs along with EDX Spectrum.

Perhaps the most important property of the architecture detailed here is the reversibility of the phase transfer process. Upon addition of Fe3+ to ortho-carborane capped gold nanoparticles in water, they shifted to ether phase and then back again to aqueous phase after reduction by Sodium borohydride. This cycle could be repeated multiple times and studies conducted of the samples in ether and aqueous phase, each time after the phase transfer were consistent with the studies done the first time after the phase transfer occurred. The size of the particles in aqueous phase from TEM were found to be around 5 nm and around 10 nm in the ether phase, irrespective of how many times the phase transfer was done. Similarly, UV-vis showed the plasmon peak due to presence of Fe^{2+} in ether phase, but not in aqueous phase. The proposed model shows an inherent capacity of the complex to expand upon entering the organic phase, thus allowing the larger Cl^- ions to enter the voids generated due to the spherical carboranes. Upon re-entering the aqueous phase, the Cl^- ions are expelled out from the voids.

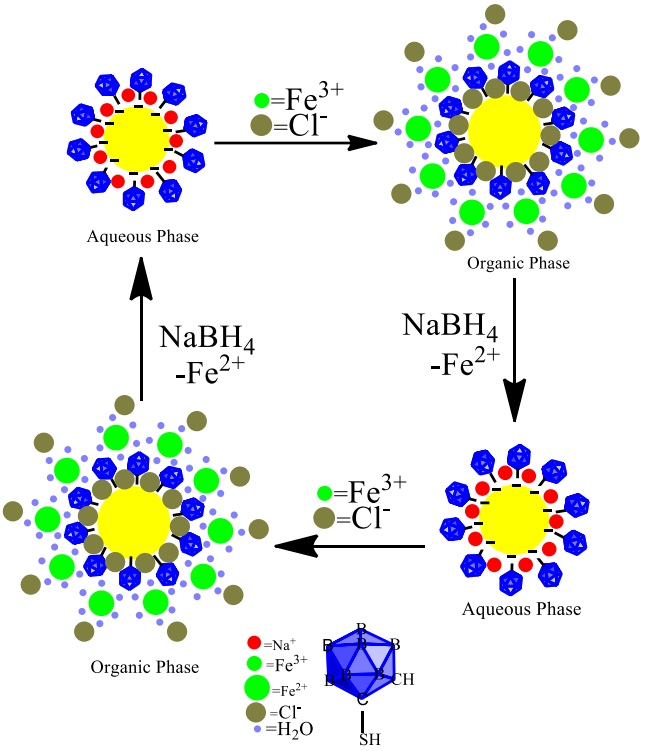

Figure 20: The schematic for the change in size of the Au NPs when there is a change in the medium.

After being quite successful with the Fe ions, we wanted to do the same tests with other divalent ions, trivalent ions or tetravalent ions. Among the other divalent ions which showed success were Ni and Mn while Ce which is a tetravalent ion showed good results too. Ce was used because it is a strong oxidising agent and it will readily oxidize the core. To quantify the results for the other ions we did XPS spectra of them showing their reduced states and also elemental mapping for them to see the position of their presence within the sample.

In the XPS spectrum of Ni, we could very well see the peak of Ni^0 at 852.6 eV. There was a small satellite present from the Ni^{2+} state in the XPS spectrum. This indicated perhaps that all of the Ni^{2+} was not transformed to Ni^0 state. The pure Ni metal has a very sharp single peak in XPS spectrum at 852.6eV, in our case the peak was present at 852.6eV but wasn't the only peak, it also had a satellite of Ni $2p_{3/2}$. The spectrum is shown in **Fig. 21**. In the case of Mn, we could see the Mn^0 peak at 638.8 eV, and it also had a satellite peak from the Mn^{2+}. Here the satellite peak was much smaller in size compared to the Mn^0 peak. In Ni the satellite peak is a little bit more prominent than in the Mn one. Both the samples showed reversible solubility in water and ether phase when reduced and oxidized respectively. For the Mn and Ni samples, the salts used for the test were chloride salts. The XPS spectrum for the Mn sample is shown in **Fig. 22**.

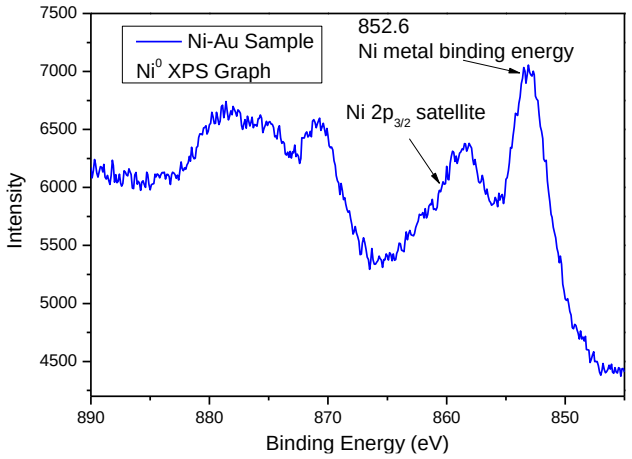

Figure 21: XPS Spectrum of Au NPs with Ni^0.

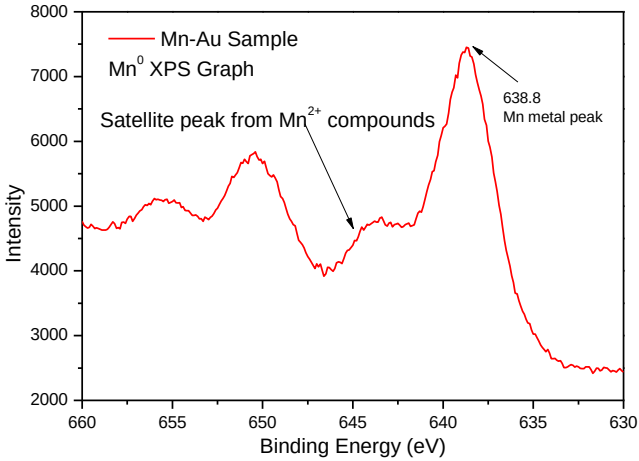

Figure 22: XPS Spectrum of Au NPs with Mn^0.

In the case of Ce, we could not see a clear spectrum in the XPS for Ce^{3+}. We started from Ce^{4+} and after oxidizing the core of Au, it should have reduced itself to Ce^{3+}. Though, the sample showed solubility in both ether and water phases, the spectrum obtained in XPS did not show a clear peak for Ce^{3+} state. Rather, the spectrum showed an intermediate state between Ce^{4+} and Ce^{3+}. The spectrum is shown in **Fig. 23**.

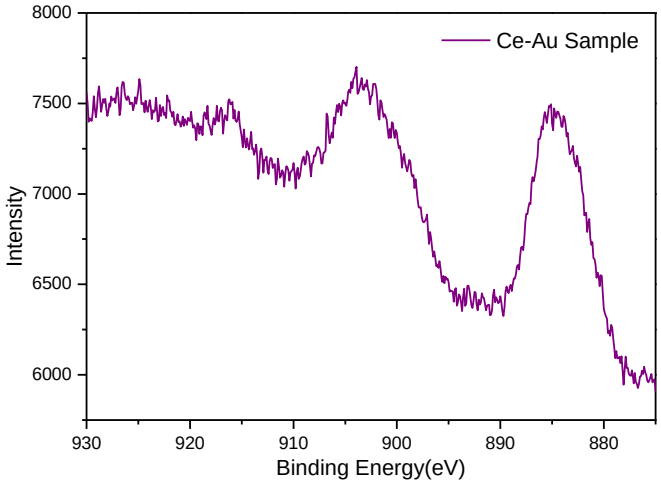

Figure 23: XPS spectrum of the Au NPs with Ce.

It must be pointed out that while the EDX spectra of Ni and Mn show the peaks of Ni^0 and Mn^0 respectively, thus fitting in with the model for phase transfer explained in **Fig. 16**, the EDX spectra also shows satellite peaks of Ni^{2+} and Mn^{2+} respectively. This would suggest that the complete oxidation of Ni and Mn does not take place, and rather an intermediate is formed. Indeed, Ni and Mn cannot exist in their 0 Oxidation state in this architecture, they would need to exist in some complexed form. It is possible that they exist as nano clusters but this is conjectural.

The elemental mapping and the EDX spectra of all the gold nanoparticles in ether phase, transferred using Ni, Mn and Ce showed the same results like we obtained with Fe ions sample. In all of them the Ni, Mn, Ce, covered the Au NPs and the ratio in the EDX was also reminiscent of

the Fe-Au sample. The At% ratio of Au:Ni in the Ni-Au sample is around 1:3, if we take into account both the energies of the Ni and Au and average them out. For Mn-Au sample, the At. % ratio of Au:Mn is 1:5, while for the Ce-Au sample, the At. % ratio of Au:Ce is 1:3 (taking both energies of the metals). So, all of them showed excess of the reduced ions compared to the Au core of the NPs. This is probably as we suggested before, due to their presence on near the surface of the sample along with the carborane spheres. The results are shown below.

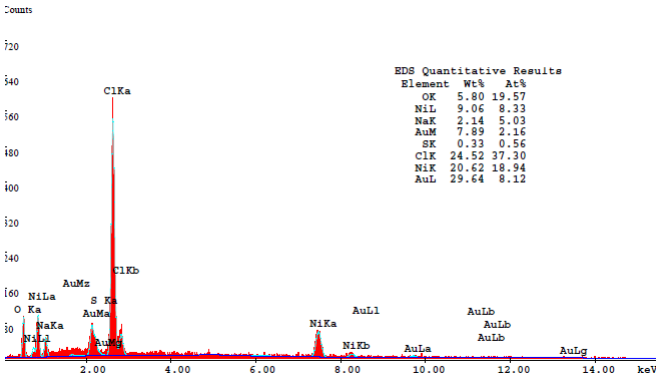

Figure 24: EDX Spectrum of Ni-Au NPs sample.

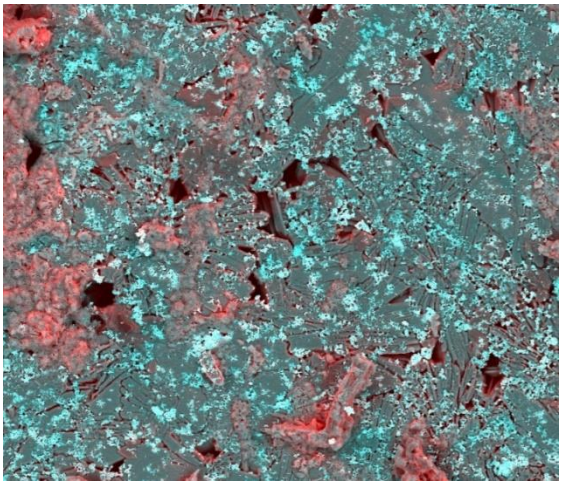

Figure 25: Elemental mapping of Ni-Au NPs sample. Here Ni is in blue and Au is in Red.

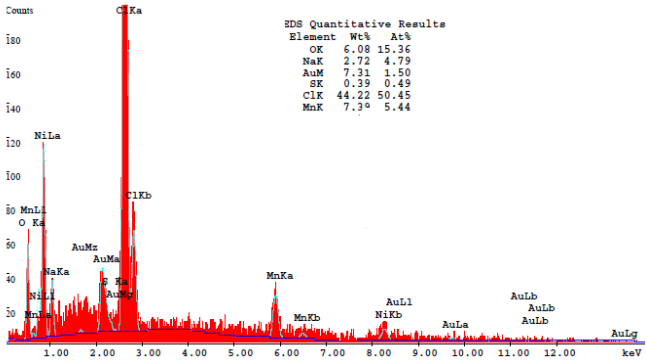

Figure 26: EDX Spectrum of Mn-Au NPs sample.

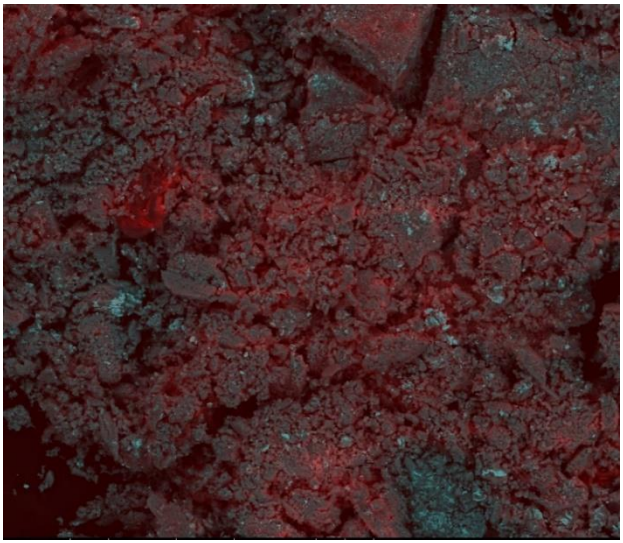

Figure 27: Elemental mapping of Mn-Au NPs sample. Here Au is in blue and Mn is in Red.

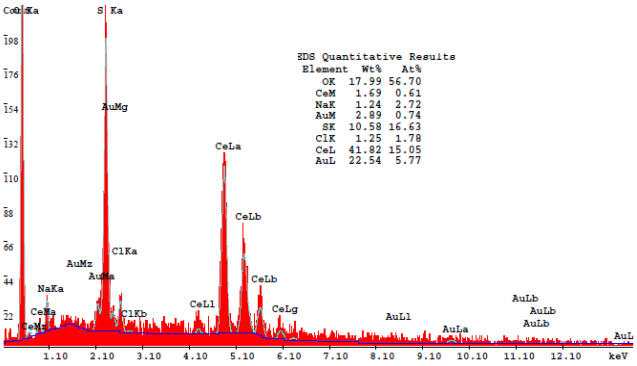

Figure 28: EDX Spectrum of Ce-Au NPs sample.

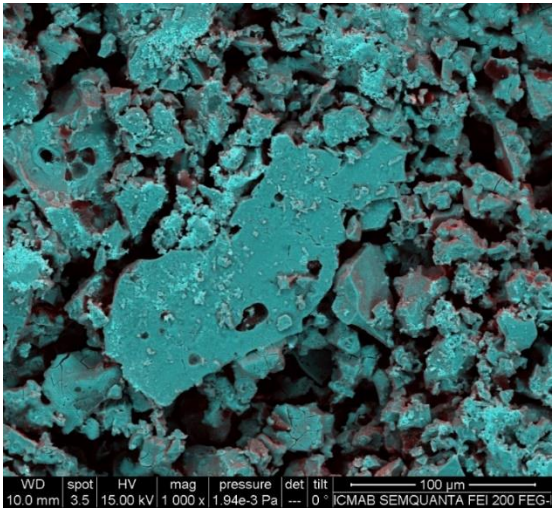

Figure 29: Elemental mapping of Mn-Au NPs sample. Here Ce is in blue and Au is in Red.

The presence of gold core remaining intact was also checked with XPS and for all the samples the peak for Au metal was observed at 84.0 eV. The figure is shown below in **Fig. 30**.

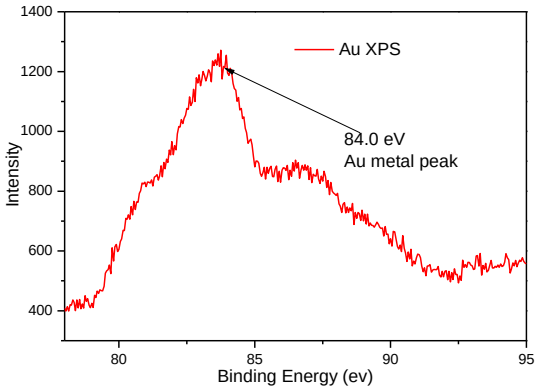

Figure 30: XPS peak for Au metal. It confirmed that the core of Au was intact throughout the experiments.

The success with phase transfer using the aforementioned cations, also prompted us to try other cations, such as Zn^{2+}, Cu^{2+}, Ce^{3+}, Eu^{3+}, but a reversible phase transfer was not successful with these cations. The gold nanoparticles transferred from the aqueous phase to the interface of the ether phase using Zn^{2+} and Ce^{3+}, but they did not transfer back to the aqueous phase upon addition of sodium borohydride. No phase transfer of Au NPs was observed upon using Cu^{2+} and Eu^{3+}.

After obtaining these results we wanted to try different thiol ligands to see if it was indeed for the carborane ligands or straight chain ligands could help us obtain the same results or not. This was not checked before when the Au NPs were initially synthesized by Vinas and co. We tried two different common thiol ligands used in water medium. They were Mercaptoacetic acid (MAA) and 3-Mercaptopropionic acid (3-MPA). When we synthesized the Au NPs using them, we could not observe any phase transfer properties in those NPs. Thus, it confirmed the fact that the close packing of the spherical carborane ligands on the spherical Au core yielded this new property in these NPs.

3.5.2.2 Gold coated Magnetic Nanoparticles decorated with Amine and Cobaltabis(dicarbollide)

This work was done as part of the European Union Horizon 2020 KardiaTool project. The aim of the project is the development of a Point of Care (POC) device for early

diagnosis of heart failure. Fe_3O_4@Au nanoparticles decorated with amine and cobaltabis(dicarbollide) were synthesized to be incorporated into the sensing layer of this device. These nanoparticles will be further functionalized with antibodies and these antibodies will act as traps for the specific antigens that indicate heart failure. This specific composition of the nanoparticles was designed as each layer of the complex plays an integral part in the POC device. The nanoparticles must be magnetic so that they can be extracted by a magnetic field. This in turn will also extract the aforementioned antigens attached to the nanoparticles. These MNPs were coated with a layer of Gold to allow for further functionalization with amine and subsequently, H[COSAN], which easily attaches itself with an amine. H[COSAN] was used due to its nature as a redox specie which has a tuneable HOMO-LUMO, thus making it attractive for using it in sensing applications.

3.5.2.2.1 Synthesis Procedure

For obtaining the gold coated magnetic nanoparticles, a precursor Iron-oleate complex was prepared using the method reported by Park et al. [28] 40 mmol of $FeCl_3.6H_2O$ (10.8 g) was mixed with 120 mmol of Sodium Oleate (36.5 g) in a mixture of 80 mL Ethanol, 140 mL Hexane and 60 mL distilled water. This solution was maintained at 70^oC for 4 hours, following which the upper organic layer containing the iron-oleate complex was washed with distilled water. After this washing, the hexane was

removed by rotary evaporation, leaving us with the waxy iron-oleate complex.

The gold coated magnetic nanoparticles (Fe_3O_4-Au, MNP@Au) were synthesized following a method reported by Xu et al. [29] 4 mmol of the iron oleate complex (2.5 g) was mixed in mixture of 30 mL oleylamine and 10 mL Oleic Acid. This solution was maintained at 100°C for 1 hour, followed by 200°C for 2 hours and finally at 300°C for 2 hours. Nitrogen was bubbled throughout the heating process to remove any traces of hydrate vapor. After the heating for the aforementioned duration, the reaction was stopped and ethanol was added to precipitate the magnetic nanoparticles. They were isolated by magnetic separation and washed with hexane and ethanol to remove any traces of oleylamine. The nanoparticles were dried under vacuum at 80°C before proceeding.

40 mg of these magnetic nanoparticles were dispersed in 10 mL Chloroform and 2 mmol oleylamine (656 μL). 2.5 mmol of $HAuCl_4$ (8.49 mg) was dissolved in 10 mL Chloroform and 1 mmol oleylamine (328 μL). The solution containing the HAuCl4 was added dropwise into the solution containing the magnetic nanoparticles, under constant stirring. This mixture was stirred for 20 hours at room temperature, following which the nanoparticles were precipitated by the addition of Ethanol. The nanoparticles were isolated by magnetic separation and washed with Ethanol and Hexane. These nanoparticles were dried under vacuum at 80°C.

At this point the gold coated magnetic nanoparticles were prepared, but they were not water soluble. To make them

water soluble, the gold coated magnetic nanoparticles were added to an aqueous solution containing 0.1 M Cetyl Trimethyl Ammonium Chloride (CTAC) and 0.1 mmol Sodium Citrate, which acts as the reducing agent. This mixture was sonicated for 10 mins, following which the nanoparticles were completely soluble in water.

The next step after this was to functionalize the Fe_3O_4-Au NPs (MNP@Au) with amino groups to facilitate the procedure of immobilizing antibodies on them or to use them to form a complex with H[COSAN]. Here we discuss the procedure to obtain the complex with H[COSAN] after functionalizing with amino groups.

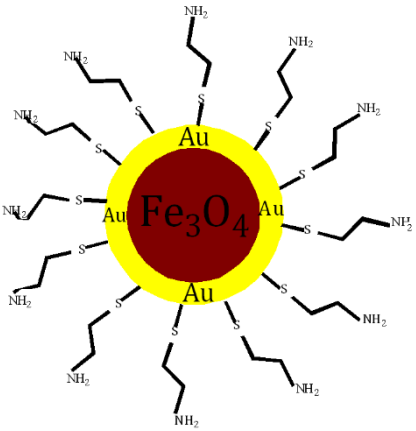

Figure 31. MNP@Au NPs decorated with amine groups.

The functionalization was done using 2-Aminoethanethiol. 20 mg of MNP@Au were dissolved in 10 mL water/ethanol mixture (1:1 by volume). [30] Then, 40 mg of 2-Aminoethanethiol was added to the reaction mixture and the reaction was then shaken mechanically using a mechanical shaker for 3 hours in the dark. The

entire procedure from measuring of 2-Aminoethanethiol to its addition has to be done in dark as it is light sensitive. The reaction was done in room temperature. Magnetic beads cannot be used in the reaction as the MNPs would be attracted towards the bead and will not react with the reagents, so this reaction was performed using a mechanical shaker. After 3 hours of the reaction in the dark, the particles were magnetically decantated and then washed with ethanol and dried to obtain the solid MNP@Au-NH_2 particles. 2-Aminoethanethiol was used because of the affinity sulphur groups have towards the Au, so in this case the thiol groups would attach themselves to the Au surface while the amino groups will be free at the periphery for further reactions. The schematic is shown below in **Fig. 32.**

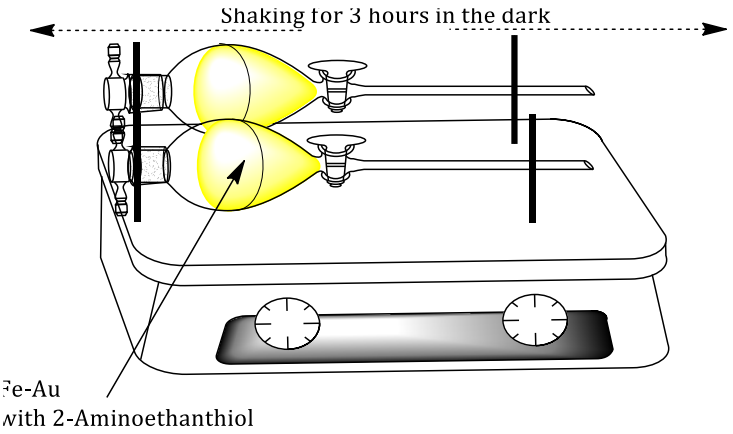

Figure 32: Schematic for functionalizing the MNP@Au with NH_2 groups.

After the synthesis of the MNP@Au-NH_2, H[COSAN] was attached to it by an ionic interaction. For this the MNP@Au-NH_2 was added to a solution of H[COSAN]

and sonicated for 30 minutes and then washed magnetically with water 3 times and dried to obtain the solid powder. This complex was then characterised using various techniques.

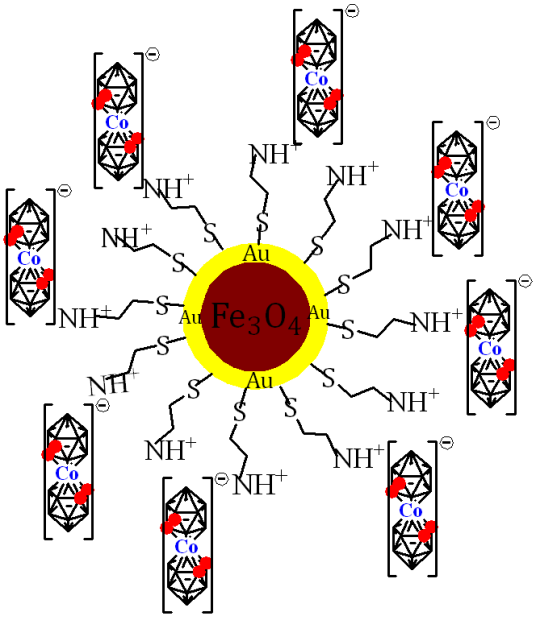

Figure 33. MNP@Au decorated with NH_2 and H[COSAN].

3.5.2.2.2 Characterization of MNP@Au-NH_2-H[COSAN]

The first technique used to characterize was UV-vis spectroscopy. First, a 5mM solution of H[COSAN] was dissolved in 10mL of water and then its UV-vis absorbance was recorded. The H[COSAN] showed a characteristic peak at 445nm. Then increasing amounts of

MNP@Au-NH_2 was added to the solution of H[COSAN], and with increasing amount of the MNP@Au-NH_2, the intensity of the peak of H[COSAN] decreased, thus confirming the attachment of H[COSAN] to MNP@Au-NH_2. This is shown in **Fig. 34.**

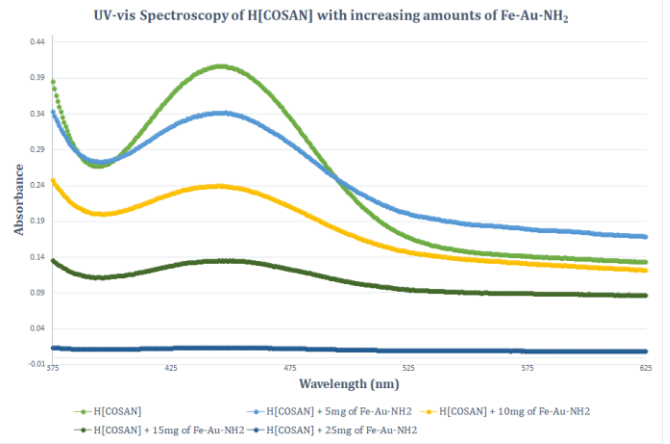

Figure 34. UV-vis of MNP@Au-NH_2 with H[COSAN] with increasing amounts of MNPs. It confirmed interaction between the H[COSAN] and the MNPs.

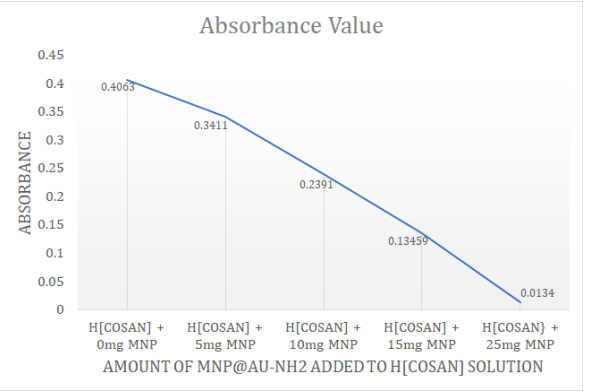

Figure 35. The decrease in absorbance of H[COSAN] as it becomes attached to increasing amounts of MNPs.

An IR spectrum of the MNP@Au-NH_2 was recorded and it clearly showed the N-H band stretching at 3103 cm^{-1} and 1536 cm^{-1} as well as the Fe-O band at 546 cm^{-1}. This confirmed that the NH_2 had been attached to the MNP@Au. (**Fig. 36**). The attachment of the H[COSAN] to these NPs was confirmed by UV-Vis, Zeta Potential and EELS.

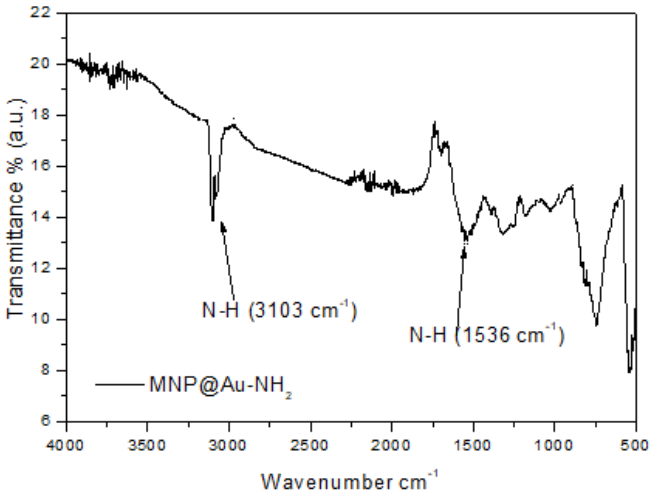

Figure 36. IR spectrum of MNP@Au-NH_2.

Fig. 37 shows the zeta potential (ζ-potential) value of MNP@Au-NH_2 as 15.8 mV, implying that the amine groups are on the surface of the NPs, thus rendering a positive value to the NPs. A ζ-potential between 10 / 30 mV, suggests that over time the MNPs will tend to aggregate. When the MNPs form the complex MNP@Au-NH_2-H[COSAN] the ζ-potential becomes negative -12.6 mV (see Fig. 35) which confirms the presence of the H[COSAN] on the surface of the nanoparticles because

[COSAN] is an anion. The ζ-potential is between -10 / -30 mV again indicating that the complex has a tendency to aggregate. This clear shift in the polarity of the MNPs before and after the interaction with the cobaltabis(dicarbollide) confirms the presence of H[COSAN] on the surface of the MNPs.

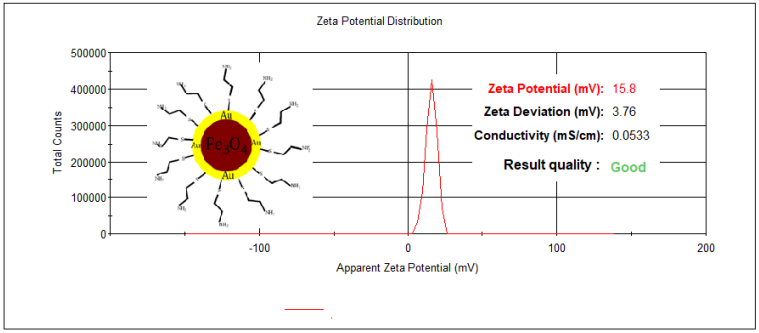

Figure 37. Zeta-potential of MNP@Au-NH_2. The zeta potential is positive here.

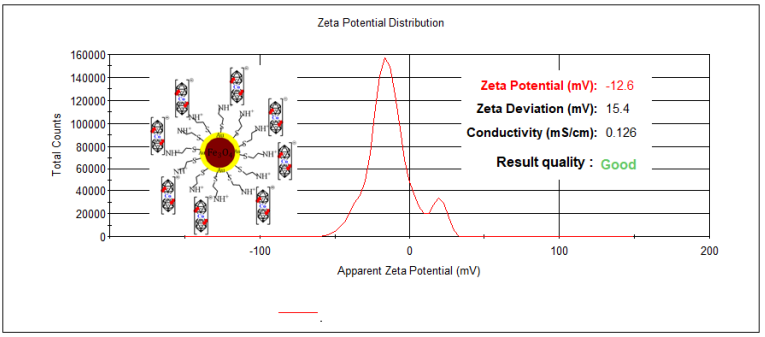

Figure 38. Zeta-potential of MNP@Au- NH_2-H[COSAN]. The zeta potential is negative here, implying attachment of H[COSAN] with the amine group.

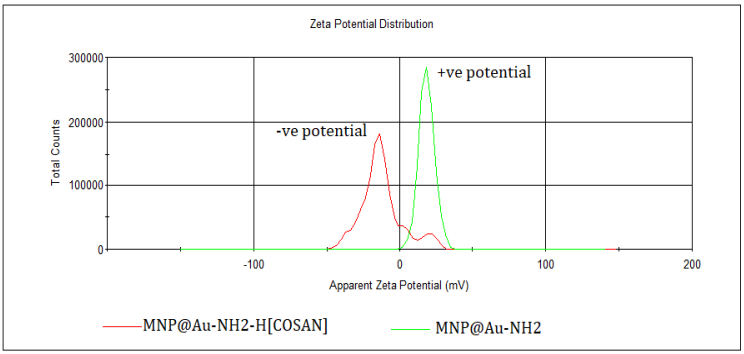

Figure 39. Comparison of zeta potential before and after attachment of H[COSAN].

The presence of the H[COSAN] on the surface of the NPs was further reinforced by EELS, which clearly indicated the presence of Boron in the sample. (**Fig. 40**)

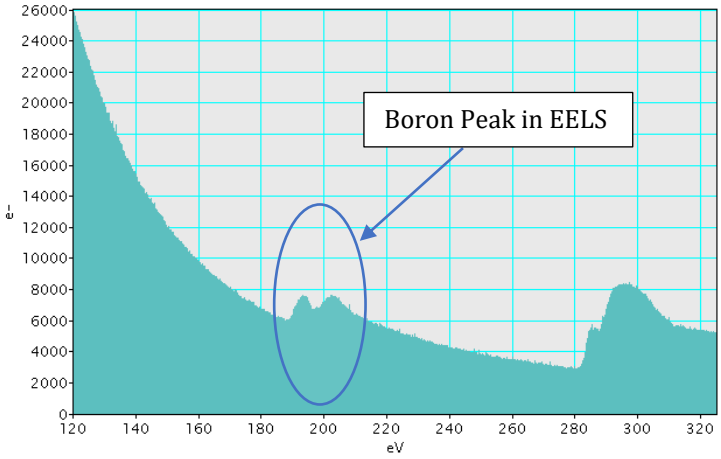

Figure 40. EELS spectrum of the MNP@Au-NH_2-H[COSAN], clearly indicating the presence of Boron.

The attachment of H[COSAN] to the MNPs is important as the cobaltabis(dicarbollide) is a redox specie possessing tuneable HOMO-LUMO. The tuneable HOMO-LUMO enables the complex to tune the energy levels in order to improve the conductivity, thus allowing complexes containing the H{COSAN] to be used in Ion Selective Sensors as already explained in the previous chapters of this thesis. The energy levels between each cobaltabis(dicarbollide) attached to the MNP@Au can be tuned too, and if they are aligned within close range, then it allows for the electrons to tunnel from one H[COSAN] to the other, attached to the MNPs surface thus improving the conductivity of the complex. This would enhance the sensing layer of the sensors in which they will be used. The H[COSAN] has another advantage of being able to self -assemble. This self-assembly property enables them to form layers on the surface of the MNPs easily. All these properties made them ideal for incorporation in the magnetic complex, seeing as how the ultimate goal was to incorporate this complex into a sensing layer.

The size of the MNP@Au after attachment of the H[COSAN] was measured using TEM. (**Fig. 41**) The mean size was calculated by measuring the particles manually using ImageJ software and plotting the

Gaussian graph and was found to be 26. 11 nm± 0.15 nm. (**Fig. 42**)

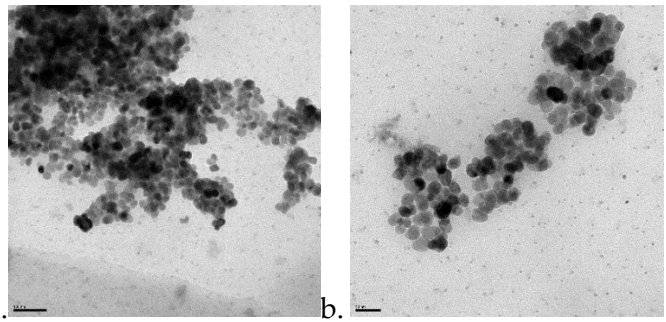

Figure 41. TEM images of the MNP@Au-NH_2-H[COSAN] complex. The studies were conducted using JEOL TEM 1210 at 120 kV.

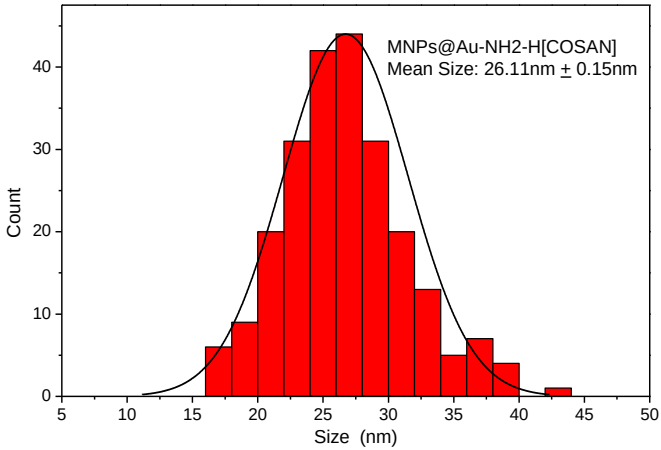

Figure 42. Gaussian size graph of MNP@Au-NH_2-H[COSAN].

EDX studies were done to study the composition of the complex and to find out the ratio of Fe, Au and Co(from the H[COSAN]) in the sample. These studies were conducted using STEM, by studying

areas of the sample with clusters of the MNP@Au-NH_2-H[COSAN] complex. (**Fig. 43**)

The EDX of the sample showed a ratio of Fe:Au:Co to be around 3:1:1 in terms of Atomic wt. %. (**Fig. 44**) This ratio is to be expected, since the core consists of Fe_3O_4 NPs and consequently they are present in high amount in the complex.

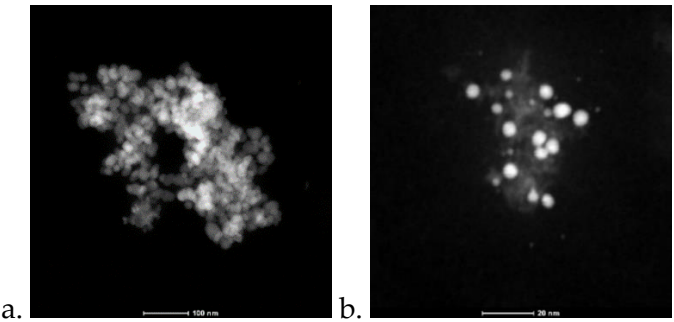

Figure 43. STEM images of MNP@Au-NH_2-H[COSAN] complex. The studies were conducted using FEI Technai F20 S TEM/HRTEM device at 200 kV.

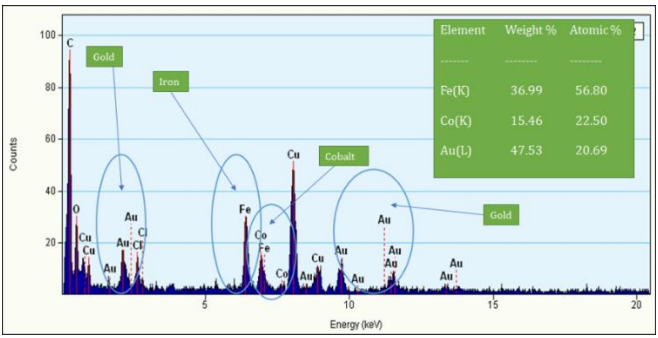

Figure 44. EDX spectrum of the MNP@Au-NH_2-H[COSAN] complex.

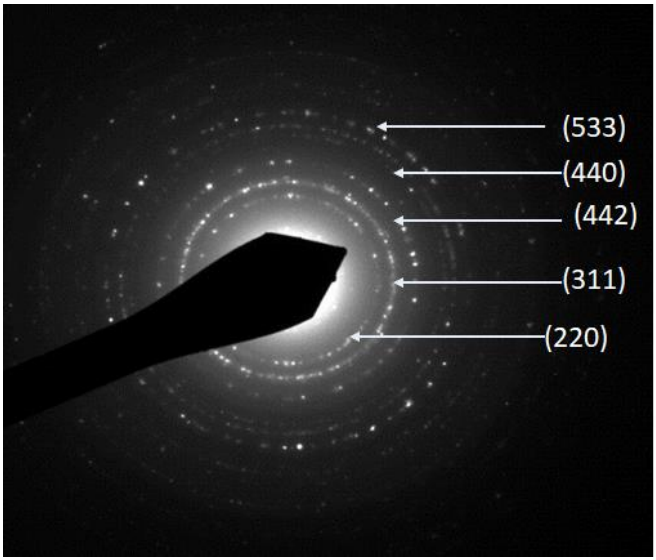

Figure 45. Electron diffraction pattern for the MNP@Au-NH_2-H[COSAN]

The selected area electron diffraction (SAED) was done on the MNPs@Au-NH_2-H[COSAN] and it showed a crystalline pattern. The pattern represented the magnetite cubic spinel structure. The crystallinity of the diffraction pattern can be attributed to the presence of the gold coating of the magnetic core and the presence of the H[COSAN]. It was not possible to see the diffraction rings for the Au NPs as the coating of the Au in the magnetic core was not very thick.

Magnetic characterization of MNPs@Au-NH_2-H[COSAN] was carried out in a Superconductive Quantum Interference Device (SQUID)

magnetometer (Quantum Design MPMS5XL). Magnetization *vs* magnetic field measurements were performed at 300 K in a field 6 T. The samples were prepared using a polycarbonate capsule filled with 1 mg of MNP@Au-NH_2-H[COSAN] and compacted cotton.

The magnetic property of iron oxide (Fe_3O_4) nanoparticles is dependent on the distribution of Fe ions in octahedral and tetrahedral sites of the spinel structure. [31] The magnetic spins of the ions in the octahedral sites are ferromagnetically coupled to each other and antiferromagnetically coupled with tetrahedral sites. Because the number of Fe^{3+} ions in the octahedral sites and the tetrahedral sites are the same, their magnetic spins cancel each other. Consequently, the magnetic spins of only Fe^{2+} ions in the octahedral sites contribute to the net magnetic moment in a spinel structure.

Fig. 46 show a typical magnetization curve at 300 K for superparamagnetic nanoparticles in which neither remnant magnetization (magnetization at zero field, M_R) nor coercivity (hysteresis loop,H_c) were observed. The saturation magnetization value of MNP@Au-NH_2-H[COSAN] at 300 K was 0.20 emu/g.

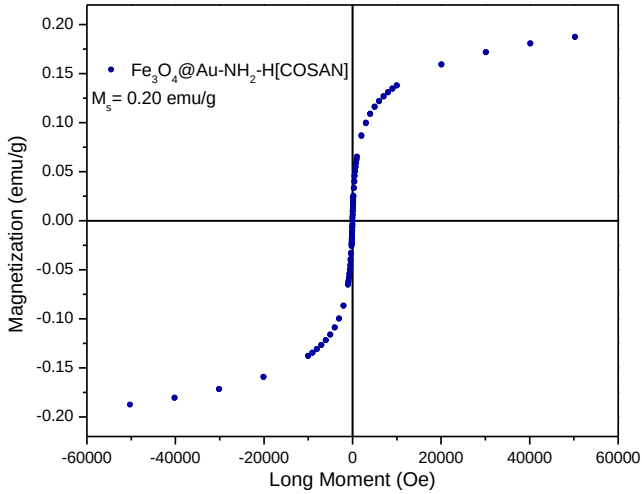

Figure 46. Magnetic Hysteresis of MNP@Au-NH2-H[COSAN] (Ms: 0.20 emu/g).

3.5.3 Conclusions

In this chapter, the phase transfer properties of *ortho*-carborane capped gold nanoparticles, which had been demonstrated in this group by Vinas and co, have been further explored. In addition to the already achieved phase transfer of the NPs between aqueous and organic media by using HCl, it was demonstrated that the phase transfer also occurred upon using, divalent, trivalent and tetravalent cations. Fe^{3+}, Ni^{2+}, Mn^{2+}, Ce^{4+} were amongst the cations that tested successfully in this phase transfer

system. This further demonstrated the use of carboranyl spheres acting as vehicles for transfer of ions from aqueous to organic phase, making them ideal for ion transport in biomedical applications. It was observed that the carboranyl spheres are present on the surface of the ions to be transported, creating a kind of charged ionic pool which upon the application of a little kinetic energy, releases energy allowing the ions to transfer from one phase to another. The samples were analysed using IR, EDX, EELS and Elemental Mapping to substantiate the presence of Boron (and hence carboranyl spheres), Gold and the cation of interest. XPS was done to demonstrate the change in oxidation state of the cations upon phase transfer.

The 2nd part of this chapter detailed the synthesis and characterization of a Fe_3O_4@Au-NH_2-H[COSAN] complex. This work was done as part of the European Union Horizon 2020 KardiaTool project. These nanoparticles were designed for use in a sensing layer to be incorporated in a Point of Care device for early diagnosis of heart failure. These nanoparticles will be further functionalized with antibodies and these antibodies will act as traps for the specific antigens that indicate heart failure. A magnetic field can easily extract the required antigens, hence necessitating the synthesis of these MNPs. These MNPs were coated with a layer of Gold

to allow for further functionalization with amine and subsequently H[COSAN]. The use of H[COSAN] is due to its nature as a redox specie which has a tuneable HOMO-LUMO which enhances the possibility of using it in sensing applications. These MNPs@Au-NH_2-H[COSAN] were characterized using TEM, STEM, EELS, EDX and their magnetic strength was determined using Magnetic Hysteresis.

3.5.4References

1. C. Burda, X.B. Chen, R. Narayanan, M. A. El-Sayed, *Chem Rev*., **105** (2005) 1025–1102.
2. M.C. Daniel, D. Astruc, *Chem Rev.,* **104** (2004) 293–346.
3. J. Homola, *Chem Rev.,* **108** (2008) 462–493.
4. P. N. Njoki et al., *J Phys Chem C,* **111** (2007) 14664–14669.
5. M. Brust, M. Walker, D. Bethell, D. J. Schiffrin, *J. Chem. Soc. Chem. Commun*. **7** (1994) 801–802.
6. M. Brust, J. Fink, D. Bethell, D. J. Schiffrin, C. J. Kiely, *Chem. Soc. Chem. Commun*., **16** (1995) 1655–1656.
7. E. Boisselier, D. Astruc, *Chem. Soc. Rev*. **38** (2009) 1759– 1782.
8. R. Sardar, A. M. Funston, P. Mulvaney, R. W. Murray, *Langmuir,* **25** (2009) 13840– 13851.
9. G. Peng et al., *Nat. Nanotechnol.,* **4** (2009) 669– 673.
10. E. Chow, T.R. Gengenbach, L. Wieczorek, B. Raguse, *Sens. Actuators. B*., **143** (2010) 704– 711.
11. E. Covincton et al., *Lab Chip,* **22** (2010) 3058– 3060.
12. C. Kim, S. S. Agasti, Z. J. Zhu, L. Isaacs, V. M. Rotello, *Nat. Chem*., **2** (2010) 962– 966.
13. Z. Krpetic et al., *Nano Lett.,* **10** (2010) 4549– 4554.
14. J. Gil-Tomas, *J. Mater. Chem.,* **21** (2011) 4189– 4196.
15. A.M. Cioran et al., *J. Am. Chem. Soc.* **134** (2012) 212-221.
16. S.M. Silva et al., *Chem. Commun*., **52** (2016) 7528-7540.
17. A. K. Gupta, M. Gupta, *Biomaterials*, **26** (2005) 3995–4021.
18. K. C. de Souza et al., *Mater. Sci. Eng., C*, **40** (2014) 275–280.
19. J. J. Gooding, S. Ciampi, *Chem. Soc. Rev*., **40** (2011) 2704–2718.
20. S. H. Koenig, K. E. Kellar, *Magn. Reson. Med*., **34** (1995) 227–233.
21. D. Yang et al., *Angew. Chem., Int. Ed*., **54** (2015) 12091–12096.
22. Y. R. Cui et al., *Talanta*, **85** (2011) 1246–1252.

23. H. Y. Park et al., *Langmuir*, **23** (2007) 9050–9056.
24. J. L. Lyon, D. A. Fleming, M. B. Stone, P. Schiffer, M. E. Williams, *Nano Lett.,* **4** (2004) 719–723.
25. I. Y. Goon et al., *Chem. Mater.,* **21** (2009) 673–681.
26. A. Saha, E. Oleshkevich, C. Vinas, F. Teixidor, *Adv. Mater.,* **29** (2017) 1704238.
27. M. P. Grzelczak et al., *ACS Nano,* **11** (2017) 212492-12499.
28. J. Park et al., Nat. Mat., **3** (2004) 891-895.
29. Z. Xu, Y. Hou, S. Sun, *J. Am. Chem. Soc.,* **129** (2007) 8698-8699.
30. G. Chen, M. Takezawa, N. Kawazoe, T. Tateishi, *The Open Biotechnology Journal*, **2** (2008) 152-156.
31. R. C. O'Handley, Modern Magnetic Materials: Principles and Applications; Wiley: New York, **1999**.

4. Conclusions

Abhishek Saini
ICMAB-CSIC (UAB)

4. Conclusions

The results in this thesis have been divided into two major parts. The first part consists of 3 chapters and deals with the use of $[Co(C_2B_9H_{11})_2]^-$ anion in use of ion pair complexes of the type $[cation\text{-}NH]^{n+}n[3,3'\text{-}Co(1,2\text{-}C_2B_9H_{11})_2]^-$ to be incorporated in the polymeric sensing layer of micro-Ion Selective Electrodes (ISEs) for the potentiometric detection of nitrogenous compounds. In this thesis, the use of this type of ISEs for the detection of the notorious algaecide Irgarol, the harmful compound belonging to Sulphonamides class of drugs- Sulfapyridine and the illicit drug Amphetamine in water.

- A micro-ISE made of a polymeric membrane comprising of $[C_{11}H_{20}N_5S][Co(C_2B_9H_{11})_2]$ as the ion pair complex was developed. The use of the metallacarborane anion $[Co(C_2B_9H_{11})_2]^-$ was due to its ability to produce weak hydrogen and dihydrogen bonds along with its electroactivity and redox reversibility make it an extremely appealing anion to be used in sensing materials. The Ion pair complex is incorporated into a PVC membrane along with different plasticizers. In this work, the ISE prepared for Irgarol detection having composition as 63% Bis(2-ethylhexyl) Sebacate (plasticizer),30% PVC (polymer matrix) and 7% $[C_{11}H_{20}N_5S][Co(C_2B_9H_{11})_2]$ ion-

pair complex worked best, showing extremely high sensitivity and selectivity towards Irgarol in water. The ISE reported here showed extremely promising results and the lowest detection limit achieved was 2 x 10^{-6} mol/dm^3 and it showed a stable response between pH 6 and 12 making it ideal for use in water. It also showed great selectivity in presence of interfering ions belonging to the same class of compounds as Irgarol. The ISE reported here gave a very quick response time of less than 10 seconds and could be used repeatedly for a period of 45 days without any degradation in its response parameters.

- Using the same strategy of incorporating the $[Co(C_2B_9H_{11})_2]^-$ anion as part of an ion pair complex, a micro-ISE was developed for the detection of Sulfapyridine. The ISE developed here using the same composition as above, produced the best results using Bis(2-ethylhexyl) Sebacate as plasticizer, showed a lowest detection limit of 1 x 10^{-6} mol/dm^3 and a working pH range of between 6 and 9. It was also 2 orders of magnitude more selective towards Sulfapyridine even in the presence of structurally similar other Sulphonamides.
- The detection of the illicit drug Amphetamine in wastewater was tackled using an $[C_9H_{13}NH]^+[Co(C_2B_9H_{11})_2]^-$ ion pair complex

based micro-ISE. The micro-ISE developed using a composition 31 wt.% of PVC, 65 wt. % of DBP (Plasticizer) and 4 wt. % of the ion-pair complex showed a perfect Nernstian response with a lowest detection limit of 1×10^{-5} mol/dm^3 and a working pH range of 1.5 to 8.5. The micro-ISE was found to highly selective towards Amphetamine in even in the presence of structurally similar compounds, which coupled with its stable lifetime and quick response time, make it an attractive device for Amphetamine detection compared to other existing devices reported for the same purpose in literature.

The second part of the Results section of this thesis deals with the use of carboranyl derivatives as capping agents for nanostructures, to produce innovative nanostructures with unique properties.

- A one step colloidal synthesis of different Quantum Nanocrystals (QNCs) using carboranyl ligands as capping agents was described. Using a different carboranyl ligand led to a different morphology in the quantum regime, all of which should a wide spectrum of PL emission colors when excited by UV light and high Quantum Yields. The reported procedure does not require the synthesis of

any intermediate structures; it is only based on the use of spherical carboranyl ligands that by means of a coordinating site binds to the cadmium to generate the QNCs of CdSe composition. The key to producing these QNCs, i.e, the carboranyl ligands are based on icosahedral carboranes of formula $C_2B_{10}H_{12}$. The method reported here is the first such method that allows for tuning morphologies in the Quantum regime, all the while using a simple one step colloidal synthesis. This led to the production of Quantum Dots, Quantum Rods, Quantum Rings and Quantum Tetrapods, finally approaching a method for the large-scale production of these novel nanostructures.

- *ortho*-carboranethiol capped gold nanoparticles were synthesized which showed the unique property of being able to transfer between and aqueous and organic phases. It was demonstrated that the phase transfer occurred upon using, divalent, trivalent and tetravalent cations. Fe^{3+}, Ni^{2+}, Mn^{2+}, Ce^{4+} were amongst the cations that tested successfully in this phase transfer system. This further demonstrated the use of carboranyl spheres acting as vehicles for transfer of ions from aqueous to organic phase, making them ideal for ion transport in biomedical applications. It

was observed that the carboranyl spheres are present on the surface of the ions to be transported, creating a kind of charged ionic pool which upon the application of a little kinetic energy, releases energy allowing the ions to transfer from one phase to another. This section also describes the synthesis of a Fe_3O_4@Au-NH_2-H[COSAN] nanoparticles. These nanoparticles were designed for use in a sensing layer to be incorporated in a Point of Care device for early diagnosis of heart failure. These nanoparticles will be further functionalized with antibodies and these antibodies will act as traps for the specific antigens that indicate heart failure. A magnetic field can easily extract the required antigens, hence necessitating the presence of a Fe_3O_4 magnetic core. These magnetic nanoparticles were coated with a layer of Gold to allow for further functionalization with amine and subsequently H[COSAN]. The use of H[COSAN] is due to its nature as a redox specie which has a tuneable HOMO-LUMO which enhances the possibility of using it in sensing applications.

ANNEX I:

Articles approved by the Committee of Department of Chemistry of Universitat de Autonoma de Barcelona (UAB) on 3rd June, 2019 to present the thesis as a compendium of articles are listed below:

- Section 3.1 (Results and Discussion): A novel potentiometric microsensor for real-time detection of Irgarol using the ion-pair complex [Irgarol-H]$^{+}$[Co($C_2B_9H_{11}$)$_2$]$^{-}$, A. Saini, J. Gallardo-Gonzalez, A. Baraket, I. Fuentes, C. Vinas, N. Zine, J. Bausells, F. Teixidor, A. Errachid., *Sensors and Actuators B*, **268** (2018) 164–169.
  DOI: doi.org/10.1016/j.snb.2018.04.070
- Section 3.2 (Results and Discussion): A simple membrane with the electroactive [Sulfapyridine-H]$^{+}$[Co($C_2B_9H_{11}$)$_2$]$^{-}$ for the easy potentiometric detection of sulphonamides, A. Saini, I. Fuentes, C. Vinas, N. Zine, J. Bausells, A. Errachid, F. Teixidor., *Journal of Organometallic Chemistry*, **893** (2019) 32-38.
  DOI: doi.org/10.1016/j.jorganchem.2019.04.030
- Section 3.3 (Results and Discussion): A highly selective potentiometric amphetamine microsensor based on all-solid-state membrane using a new ion-pair complex,[3,3′-Co(1,2-closo-$C_2B_9H_{11}$)$_2$]$^{-}$[$C_9H_{13}NH$]$^{+}$, J. Gallardo-Gonzalez, A. Saini, A. Baraket, S. Boudjaoui, A. Alcacer, A. Streklas, F. Teixidor, N. Zine, J. Bausells, A. Errachid., *Sensors and Actuators B*, **266** (2018) 823–829.
  DOI: doi.org/10.1016/j.snb.2018.04.001